Studies on Joining and Deposition using Planar Movement Setup for GMAW

A Thesis

Submitted in partial fulfilment of the requirements for the award of degree of

Doctor of Philosophy

in

Mechanical Engineering

Submitted by

Vinod Kumar

Regd. No. 951608003

Under the guidance of

Dr. Tarun Kumar Bera

Professor and Head
Department of Mechanical Engineering
Thapar Institute of Engineering & Technology
(Deemed to be University), Patiala

Department of Mechanical Engineering
Thapar Institute of Engineering & Technology
(Deemed to be University)
Patiala-147004, India
January, 2022

Dedicated to my Father

DECLARATION

I certify that

a. The work contained in this Thesis is original and has been done by me under the guidance of my supervisor.
b. The work has not been submitted to any other institute for any degree or diploma.
c. I have followed the guidelines provided by the institute in preparing the Thesis.
d. I have confirmed to the norms and guidelines given in the ethical code of conduct of the institute.
e. Whenever I have used materials (data, theoretical analysis, figures and text) from other sources, I have given due credit to them by citing them in the text of the Thesis and giving their details in the references. Further, I have taken permission from the copyright owners of the sources, whenever necessary.

Vinod Kumar

(Vinod Kumar)

CERTIFICATE

This is to certify that the Thesis entitled **'Studies on Joining and Deposition using Planar Movement Setup for GMAW'**, submitted by **Mr. Vinod Kumar** to Thapar Institute of Engineering & Technology (Deemed to be University), Patiala, India, is a record of bona fide research work carried under my supervision and is worthy of consideration for the award of the degree of Doctor of Philosophy of the Institute.

Dr. Tarun Kumar Bera

Professor and Head
Mechanical Engineering Department
Thapar Institute of Engineering & Technology (Deemed to be University),
Patiala, India, 147004
Email: tkbera@thapar.edu

Date: 07.06.2022

ACKNOWLEDGEMENT

First of all, I wish to thank the Lord, whose blessings have given me the strength which enabled me to successfully accomplish this Thesis. With great gratitude, I would like to express my deepest regards for my supervisor Dr. Tarun Kumar Bera, Professor and Head, Department of Mechanical Engineering, Thapar Institute of Engineering & Technology, Patiala for his invaluable guidance, moral support and encouragement during the entire period of this research which cannot adequately be expressed in words in this acknowledgement. His deep insight into the problems and the ability to provide constructive suggestions have been of immense value in improving the quality of my research work.

Heartfelt thanks are due to Prof. Prakash Gopalan (Director, Thapar Institute of Engineering & Technology, Patiala) and Prof. Rafat Siddiqui (Dean, Research and Sponsored Projects, Thapar Institute of Engineering & Technology, Patiala), Prof. Ajay Batish (Deputy Director, Dean of Partnerships & Accreditation and Professor in Mechanical Engineering Department, Thapar Institute of Engineering & Technology, Patiala), Dr. Kulvir Singh (Professor & Head, School of Physics and Material Science), Dr. Tarun Nanda (PhD coordinator, MED) and Dr. Anu Mittal (PhD coordinator, MED) for their encouragement and moral support throughout this period.

I would like to wholeheartedly thank all the members of my Doctoral committee including Dr. Raj Kumar Gupta, Professor, Department of Chemical Engineering, Dr. Dheeraj Gupta, Associate Professor, Department of Mechanical Engineering and Dr. Deepa Mudgal, Assistant Professor, Department of Mechanical Engineering for their continuous encouragement, critical and insightful comments for providing indispensable advice.

I am very thankful to Dr. Ajay Batish, Professor and Head of Central Workshop, Thapar Institute of Engineering & Technology, Patiala, for providing the necessary facilities in the workshop to fabricate the experimental setup. I am also thankful to Sh. Lalit Rana, Foreman, Central Workshop, for his co-operation, moral support and encouragement throughout this period.

I convey my sincere thanks to Dr. Anirban Bhattacharya, Assistant Professor, Indian Institute of Technology Patna, Bihar, India, for his valuable advice and suggestions at different times.

I express my sincere thanks to Dr. Vivek Jain, Associate Professor, Department of Mechanical Engineering, Thapar Institute of Engineering & Technology, Patiala for permitting the use of coordinate measuring machine, hardness tester and measuring microscope in Advanced Measurement Lab.

I would like to wholeheartedly thank Dr. Dhiraj K. Mahajan, Assistant Professor, and Sh. Rupinder Singh Mundra, IIT, Ropar for permitting the use of Universal Testing Machine and Impact Testing Machine.

I also extend my sincere thanks to Dr. V. K. Bansal, Deputy Director, Govt. I.T.I. Patiala for his whole hearted help.

I would also like to thank Sh. Narinder Kumar and Sh. Sarabjit Singh, Lab. Superintendent, Department of Mechanical Engineering and Sh. Munish Kumar, Department of Chemical Engineering, Thapar Institute of Engineering & Technology, Patiala for their help and open discussions.

I wish to thank my seniors, colleagues and dear friends Dr. Rajmeet Singh, Dr. Rashmi Arora, Mr. Prakhar Jain, Mr. Himanshu, Dr. Ashu Garg, Dr. Mohit Raj Saxena, Dr. Manjit Singh Matharu, Dr. Vipin Kumar Sharma, S. Dhian Singh, S. Rajinder Singh, S. Baldev Singh, S. Harsimran Singh and many others for their constant moral support and friendship.

I thank all the souls who helped me in this herculean task. Finally, I bow my head to the **ALMIGHTY** for all the blessings he has showered on me.

Vinod Kumar

(Vinod Kumar)

ABSTRACT

Now-a-days, owing to the rapid advances in technology and immense human intervention, most of the industrial components are not fabricated by conventional manufacturing processes. Industrial automation plays a significant role in order to achieve high accuracy, reliability, precision and quality of industrial processes, but at higher expenses. Automation involved in controlling and operating the various equipment such as CNC machines, robotic welding arms, heat-treating ovens, boilers, stabilization of ships, aircraft, and vehicles mitigates human interventions. In recent years, 3D metal printing technique is tremendously used for building products by vertical layer depositions in various engineering applications. Various welding techniques such as gas metal arc welding (GMAW), laser arc welding, electron beam welding, gas tungsten arc welding (GTAW) and plasma arc welding (PAW) are used for additive manufacturing (AM), but GMAW based AM has gained tremendous popularity in the industry. GMAW based AM builds metallic parts by depositing layer over layer to achieve relatively higher deposition rates and denser structures. As fully automation is involved in GMAW based AM, constant contact tubes to work distance provides consistent bead geometry, low spatters, uniform heat input and deep penetration depth as compared to conventional manual welding.

To address this challenge, a bi-directional automatic movement setup is indigenously designed and developed to obtain weld with uniform bead width along a desired path and having capability to perform vertical layer depositions for different open and closed profiles utilizing gas metal arc welding. A computer-aided design (CAD) model and a prototype of bi-directional movement setup for planar welding are first made for conceptualization and then, the setup is fabricated. It mainly consists of stepper motors, carriage, transmission system and guide ways. The welding torch is kept perpendicular to the substrate during deposition of all profiles. A trigger is provided under the torch holding device to manually switch on/off the welding torch whenever required. A dedicated electronic control unit is developed to independently control both stepper motors along two different axes for the desired positions of the welding torch during metal deposition. The control system is Arduino UNO based. The control system is responsible for starting of arc, controlling the speed of stepper motors, welding speed and precision of given trajectory during deposition. System modelling of the fabricated setup is carried out using a bond graph technique to predict different system behaviours as well as to predict the weld bead geometric path.

The effectiveness of the automatic planar movement setup is validated to check the uniformity in bead width and path/profile of the deposited weld bead, to perform vertical layer deposition for different open profiles (e.g., spiral and S-shape) and closed profiles (e.g., circular, elliptical) and to build three-dimensional specimens through different paths strategies followed for deposition i.e., spiral-in (circular and square), raster (square, diagonal and circular) at different welding speeds. The dissimilar joining between three different grades of steels (austenitic (AISI 304, AISI 316) and duplex 2205 stainless steels) are welded in the presence of three activated

fluxes (SiO_2, TiO_2 and CrO_3) following Taguchi fractional factorial design of experiment (DOE) technique. The influences of welding parameters namely welding current, voltage, workpiece material, filler material and gas flow rate along with activated fluxes are investigated on the depth of penetration of dissimilar steels. Finally, the prepared welded specimens are tested under mechanical and metallurgical testing. Mechanical testing such as tensile strength, toughness, microhardness, flexural strength of the deposited specimens following ASTM (American Society for Testing and Materials) and IS (Indian Standards) are performed to investigate the influence of various process parameters. The microstructural characterization of the base metal, heat-affected zone and welded zone of the deposited parts is carried out using scanning electron microscopy (SEM).

The experimental results reveal that the developed machine is suitable for effectively tracking the reference path and executing welding of any shape in two-dimension. The constant contact tube to work distance provided by the automated fabricated setup is required to achieve the significant consistency in weld bead width for all deposited profiles. The weld bead width increases due to lowest speed in case of spiral shaped weld profile and consequently, maximum heat is generated for this profile followed by S-shape, circular and elliptical profiles. The bead deposition is consistent i.e., deposited width and the layer heights all over the path of the deposition for different geometric shapes are almost uniform. Thus, the developed machine is also suitable for executing 3D metal deposition of any simple or complex shape. The fabricated setup is capable of building overhanging components with a maximum of 20˚ inclination. Maximum micro hardness value is observed in HAZ followed by weld metal and base metal in all the profiles. Comparatively better results are obtained from tensile, bending and microhardness testing and these results support that the deposited parts have dense structure. Amongst the five deposition strategies, raster linear (circular) exhibits highest tensile strength value followed by raster diagonal (square), raster (square), spiral-in (square) and spiral-in (circular). Among the activated fluxes, SiO_2 significantly improves the bending strength and toughness as compared to tensile strength and microhardness.

Keywords: Automatic GMAW, planar welding, closed and opened profiles, vertical layer deposition, dissimilar stainless-steel joining, activated flux, uniform bead geometry, tensile test, bending test, micro-hardness, SEM, bond graph modelling.

LIST OF ABBREVIATIONS

3DP	3-Dimensional Printing
AC	Alternative Current
A-GTAW	Activated Gas Tungsten Arc Welding
AISI	American Iron and Steel Institute
AM	Additive Manufacturing
ANN	Artificial Neural Network
ANOVA	Analysis of Variance
APCS	Adaptive Process Control Scheme
ASTM	American Society for Testing and Materials
BG	Bond Graph
CAD	Computer Aided Designing
CMB	Controlled Metal Buildup
CMM	Coordinate Measuring Machine
CMT	Cold Metal Transfer
CNC	Computer Numerical Control
CTWD	Contact Tube to Workpiece Distance
DC	Direct Current
DFF	Direct Freeform Fabrication
DOE	Design of Experiment
DOF	Degrees of Freedom
DMLS	Direct Metal Laser Sintering
EBF	Electron Beam Freeform Fabrication

EBM	Electron Beam Melting
EDX	Energy Dispersive X-ray
GMAW	Gas Metal Arc Welding
GTAW	Gas Tungsten arc welding
HAZ	Heat Affected Zone
HLM	Hybrid Layered Manufacturing
IMC	Inter-Metallic Compound
IS	Indian Standards
KE	Knee Exoskeleton
MAT	Medial Axis Transformation
MIG	Metal Inert Gas
OA	Orthogonal Array
P-GMAW	Pulsed Gas Metal Arc Welding
RM	Rapid Manufacturing
RP	Rapid Prototyping
SDM	Shape Deposition Manufacturing
SEM	Scanning Electron Microscope
SFF	Solid Freeform Fabrication
SLM	Selective Laser Melting
SLS	Selective Laser Sintering
SMD	Shape Metal Deposition
SMPS	Switch Mode Power Supply
TEP	Tennessee Eastman Process

T-GMAW	Tandem Gas Metal Arc Welding
TIG	Tungsten Inert Gas
VHN	Vickers Hardness Number
WAAM	Wire and Arc Additive Manufacturing
WEDM	Wire Electric Discharge Machining

NOMENCLATURE

C	Compliance element
CO_2	Carbon dioxide gas
CrO_3	Chromium trioxide
Df	Flow detector
G	Gear ratio
GY	Gyrator
H_i	Heat input rate
i	Current (A)
I	Inertial element
I_w	Welding current
J_f	Moment of inertia of flywheel (kg-m^2)
J_L	Moment of inertia of lead screw (kg-m^2)
k_b	Back emf constant (V-s/rad)
k_f	Stiffness of guide (N/m)
k_m	Motor constant (N-m/A)
k_t	Torsional stiffness of shaft (N-m/rad)
L	Lead of lead screw (mm)
L_a	Armature inductance (H)
MSe	Modulated source of effort
M_s	Mass of guide and welding gun (kg)
R	Resistive element
R_a	Armature resistance (Ω)
R_{b_1}	Damping in bearing1 (N-s/m)
R_{b_2}	Damping in bearing2 (N-s/m)
R_g	Damping in guide (N-s/m)
R_v	Viscous damping (N-s/m)
R_t	Torsional stiffness (N-m/rad)
Se	Source of effort
Sf	Source of flow

SiO_2	Silicon dioxide
S_w	Weld speed (m/s)
TF	Transformer
TiO_2	Titanium dioxide
v	Voltage (V)
V_w	Welding voltage (V)

Greek Characters

σ	Standard deviation
τ	Torque (N-m)
ω	Angular velocity (rad/s)
μ	Transformer modulus
$\dot{\theta}$	Rotational speed (rad/s)

PUBLICATIONS FROM PRESENT WORK

[1] V. Kumar, Bera T. K. and Bhattacharya A., "Development and performance analysis of semi-automatic movement setup for planar welding" Materials and Manufacturing Processes. 2019, 34(11), 1251–1261. DOI:10.1080/10426914.2019.1643470.

Publisher: Taylor & Francis, **Category**: SCI, **Impact Factor**: 4.616.

[2] V. Kumar and Bera T. K., "Performance of automated machine for different profiles in two-dimensional welding" Materials and Manufacturing Processes. 2020, 36(41), 435–447. DOI: 10.1080/10426914.2020.1843665.

Publisher: Taylor & Francis, **Category**: SCI, **Impact Factor**: 4.616.

[3] V. Kumar and Bera T. K., "GMAW-based metal deposition using semi-automatic movement setup" Arabian Journal for Science and Engineering. 2022, 1–14. DOI: 10.1007/s13369-021-06486-7.

Publisher: Springer, **Category**: SCI, **Impact Factor**: 2.334.

[4] V. Kumar and Bera T. K., "Effect of activated fluxes during welding of dissimilar stainless steels using semi-automatic setup" Materials and Manufacturing Processes. 2022, 1–10. DOI: 10.1080/10426914.2022.2065001.

Publisher: Taylor & Francis, **Category**: SCI, **Impact Factor**: 4.616.

[5] V. Kumar and Bera T. K., "Investigation of metal deposited objects for different build strategies using semi-automatic welding setup" Materials and Manufacturing Processes, (To be communicated).

Publisher: Taylor & Francis, **Category**: SCI, **Impact Factor**: 4.616.

LIST OF FIGURES

Fig. No.	Figure Captions	Page No.
1.1	Classification of welding processes	2
1.2	Gas metal arc welding operation	3
1.3	Gas metal arc welding setup	4
3.1	Planar movement setup for GMAW: (a) CAD model and (b) a wooden prototype	38
3.2	Automated welding machine: (a) fabricated setup at initial stage, (b) fabricated setup after modifications and (c) complete fabricated setup with welding arrangement	40
3.3	Block diagram of the setup	41
3.4	Connectivity between controller, drivers and motors	43
3.5	Word bond graph of the setup	44
3.6	Bond graph model of the setup for *x*-directional movement	46
3.7	Bond graph model of the setup in two directions	47
3.8	System responses of the planar welding setup in single direction	50
3.9	Different profiles for welding	51
3.10	System responses of planar welding setup (a, c, e, g) Input voltage and armature current for circular, elliptical, S-shaped and spiral profile, respectively (b, d, f, h) Torque and angular velocity of motor for circular, elliptical, S-shaped and spiral profile, respectively	53
4.1	Instruments used for testing: (a) spectroscopy machine, (b) coordinate measuring machine, (c) profile measuring microscope and (d) SEM machine	57
4.2	Representative weld bead geometry after GMAW using the presently developed setup at: (a) fast speed, L shape, (b) slow speed, L shape, (c) fast speed, 45°, (d) slow speed, 45°, (e) simultaneously fast along *x*-direction and slow along *y*-direction, and (f) simultaneously fast along *y*-direction and slow along *x*-direction	58
4.3	Single direction individual movement control with uniform speed in each axis (fast speed 3.5 mm/s, L-shape bead)	60
4.4	Single direction individual movement control with uniform speed in each axis (slow speed 2.5 mm/s, L-shape bead)	61
4.5	Simultaneous movement control in both axes with uniform high speed (3.5 mm/s) in both axes	63

Fig. No.	Figure Captions	Page No.
4.6	Simultaneous movement control in both axes with uniform speed (2.5 mm/s) in both axes	64
4.7	Single direction movement control with slow speed in *x*-axis and fast speed in *y*-axis, L-shape bead	65
4.8	Simultaneous movement control in both axes with unequal speed in both axes (fast speed in *x*-axis and slow speed in *y*-axis)	67
4.9	Simultaneous movement control in both axes with unequal speed in both axes (slow speed in *x*-axis and fast speed in *y*-axis)	68
4.10	Weld path geometric accuracy comparison between deposited path and predicted weld paths. (Note for legends of Fig (d) - FS: Simultaneous fast speed and slow speed along *x* and *y*-direction respectively, result from experiment, SF: Simultaneous slow speed and fast speed along *x* and *y*-direction respectively, result from experiment, BG: Simulated values from bond graph model for both the cases)	69
4.11	Different profiles for welding	71
4.12	Geometries of weld beads for: (a) circle, (b) ellipse, (c) S-shape and (d) spiral	72
4.13	Welding of circular profile (a) Weld of circular profile, (b) Weld bead appearance, (c) Measured weld profile, (d) Bead width variation, (e) SEM image of interfaces, (f) SEM image of weld fusion zone, (g) SEM image of HAZ and (h) SEM image of base metal	74
4.14	Welding of elliptical profile: (a) Weld of elliptical profile, (b) Weld bead appearance, (c) Measured weld profile, (d) Bead width variation, (e) SEM image of interfaces, (f) SEM image of weld fusion zone, (g) SEM image of HAZ and (h) SEM image of base metal	76
4.15	Welding of S-shape profile (a) Weld of S-shaped profile, (b) Weld bead appearance, (c) Measured weld profile, (d) Bead width variation, (e) SEM image of interfaces, (f) SEM image of weld fusion zone, (g) SEM image of HAZ and (h) SEM image of base metal	77
4.16	Welding of spiral profile (a) Weld of spiral profile, (b) Weld bead appearance, (c) Measured weld profile, (d) Bead width variation, (e) SEM image of interfaces, (f) SEM image of weld fusion zone, (g) SEM image of HAZ and (h) SEM image of base metal	79
4.17	Micro-hardness of different profiles	79
4.18	Comparison of weld bead in experiment and simulation	81
4.19	Different profiles for material deposition	83

Fig. No.	Figure Captions	Page No.
4.20	Material deposition of cylindrical profile: (a) material deposition of cylindrical profile, (b) wireframe of 3D measured material deposition, (c) layer height variation, (d) bead width variation, (e) SEM image of metal deposition zone at top layer, (f) SEM image of metal deposition zone at intersection of two layers, (g) SEM image of metal deposition zone at second last layer, (h) EDX spectrum showing peaks of elemental composition in deposited specimen, (i) SEM image of HAZ, (j) cross section of metal deposited specimen and (k) SEM image of base metal	86
4.21	Metal deposition of elliptical profile: (a) material deposition of cylindrical profile, (b) wireframe of 3D measured material deposition, (c) layer height variation, (d) bead width variation, (e) SEM image of metal deposition zone at top layer, (f) SEM image of metal deposition zone at intersection of two layers, (g) SEM image of metal deposition zone at second last layer, (h) SEM image of HAZ, (i) cross section of metal deposited specimen and (j) SEM image of base metal	88
4.22	Metal deposition of concave profile: (a) material deposition of cylindrical profile, (b) wireframe of 3D measured material deposition, (c) layer height variation, (d) bead width variation, (e) SEM image of metal deposition zone at top layer, (f) SEM image of metal deposition zone at intersection of two layers, (g) SEM image of metal deposition zone at second last layer, (h) SEM image of HAZ, (i) cross section of metal deposited specimen and (j) SEM image of base metal	90
4.23	Metal deposition of semi-cylindrical profile: (a) material deposition of cylindrical profile, (b) wireframe of 3D measured material deposition, (c) layer height variation, (d) bead width variation, (e) SEM image of metal deposition zone at top layer, (f) SEM image of metal deposition zone at intersection of two layers, (g) SEM image of metal deposition zone at second last layer, (h) SEM image of HAZ, (i) cross section of metal deposited specimen and (j) SEM image of base metal	92
4.24	Metal deposition of double semi-cylindrical profile: (a) semi-cylindrical profile, (b) wireframe of 3D measured material deposition, (c) layer height variation, (d) bead width variation, (e) SEM image of metal deposition zone at top layer, (f) SEM image of metal deposition zone at intersection of two layers, (g) SEM image of metal deposition zone at second last layer, (h) SEM image of HAZ, (i) cross section of specimen and (j) SEM image of base metal	93

Fig. No.	Figure Captions	Page No.
4.25	Metal deposition of V-profile. (a) material deposition of cylindrical profile, (b) wireframe of 3D measured material deposition, (c) layer height variation and (d) bead width variation	94
4.26	(a) Micro-hardness of different profiles (circle, ellipse, semi-circle, double semi-circle, concave and V-profile) and (b) best-fit third-order polynomial curves for micro-hardness	95
4.27	(a) Top layer and its vicinity, (b) SEM image of metal deposition zone at top layer, (c) SEM image of metal deposition zone at intersection of two layers, (d) SEM image of metal deposition zone at second last layer, (e) EDX spectrum showing peaks of elemental composition in deposited specimen, (f) SEM image of HAZ, (g) cross section of metal deposited specimen and (h) SEM image of base metal for metal deposition of V-profile	98
4.28	Different metal deposition patterns	99
4.29	Fabrication of components using negative and positive slops for: (a) circular object and (b) square object	99
4.30	(a) Marked specimen for cutting, (b) location of specimens for cutting and (c) test specimens geometry	101
4.31	Location of tensile and flexural specimens for different strategies	101
4.32	Different strategies used for deposition along with actual specimens and their wire frames raster (square) (a-b), raster diagonal (square) (c-d), spiral-in (square) (e-f), spiral-in (circular) (g-h) and raster linear (circular) (i-j)	103
4.33	(a) Fractured tensile specimens and (b) fractured bending specimens	105
4.34	Comparison of tensile stress and maximum bending load during different patterns	106
4.35	Microhardness results: (a) location of indentations on deposited specimen, (b) microhardness values of different patterns and (c) comparison of time taken for different build strategies	107
4.36	SEM images of metal deposition zone at upper layer**,** interface of two layers and lower layer raster (square) (a-c), raster diagonal (square) (d-f), spiral-in (square) (g-i), spiral-in (circular) (j-l) and raster linear (circular) (m-o)	110
5.1	Automatic bi-directional movement setup: (a) fabricated GMAW setup, (b) specimen after applying activated flux and (c) welded specimen	114
5.2	(a) Marking arrangement of different test welded specimens and (b) geometry of all test specimens	116
5.3	Fractured specimens during: (a) tensile, (b) impact and (c) bend test	116

Fig. No.	Figure Captions	Page No.
5.4	(a) The effect of process variables on joint, (b) influence of each factor on the tensile strength of the joint of austenitic AISI 304/ 316 with duplex 2205	120
5.5	(a) The effect of process variables on joint, (b) influence of each factor on the bending strength of the joint of austenitic AISI 304/ 316 with duplex 2205	121
5.6	(a) The effect of process variables on joint, (b) influence of each factor on the toughness of the joint of austenitic AISI 304/ 316 with duplex 2205	121
5.7	(a) The effect of process variables on joint, (b) influence of each factor on the microhardness of the joint of austenitic AISI 304/ 316 with duplex 2205	121
5.8	Effects of activated fluxes on the weld bead geometry during 18 experiments	123
5.9	Metallurgical studies by SEM at boundaries between base material and fusion region after dissimilar joining	126

LIST OF TABLES

Table. No.	Table Captions	Page No.
3.1	Parameter values used for modelling in uni-directional motion	49
3.2	Parameters required for modelling in bi-directional motion	50
4.1	Work material used in the present study	56
4.2	Absolute errors for various straight path profiles with same or different speeds	70
4.3	Spectroscopy results of workpiece utilized in the present work	71
4.4	Speed of welding during deposition of different profiles and corresponding heat input	80
4.5	Maximum variation produced during deposition of different profiles	80
4.6	Material composition	83
4.7	Material composition in the present study	100
5.1	Weight percentage of base metal	115
5.2	Factors and their varied levels for each process variable chosen for joining the dissimilar metals	117
5.3	Trial conditions of L_{18} (3^5-2^1) experimental design (OA) and consequent experimental results, Mixed level Taguchi static designs	118
5.4	ANOVA summary of results after joining between dissimilar steels	118
5.5	Comparison of Techno-Economic aspect	127

TABLE OF CONTENTS

Dedication i

Declaration iii

Certificate v

Acknowledgement vii

Abstract ix

List of Abbreviations xi

Nomenclature xv

Publications from Present Work xvii

List of Figures xix

List of Tables xxv

Chapter 1: Introduction 1–14

1.1 Joining and Metal Deposition 1

1.2 Classification of Welding Processes 2

1.3 Different Metal Deposition Methods 4

1.4 Process Parameters for GMAW 6

1.5 Bond Graph Technique for System Modelling 8

1.6 Background and Motivation 9

1.7 Significance of the Research 10

1.8 Contribution of the Thesis 11

1.9 Organization of the Thesis 12

Chapter 2: Literature Review 15–36

2.1 WAAM based Rapid Prototyping 16

2.2 Other Rapid Prototyping Techniques 18

2.3 Different Difficulties in AM 20

2.4 Advanced Techniques in AM 22

2.5 Thermal Behaviour in AM 24

2.6 Influence of Process Parameters on Metallic Properties 25

2.7 Dissimilar Metals Joining 28

2.8 Effects of Activated Fluxes in Welding 30

2.9 Bond Graph Modelling 32

2.10 Observations from Literature 34

2.11 Objectives of the Present Work 35

Chapter 3: Fabrication and Modelling of GMAW Setup 37–54

3.1 Computer-Aided Design (CAD) Model and a Prototype 38

3.2 Fabrication of GMAW Setup 38

3.2.1 Block Diagram of the Setup 41

3.2.2 Connectivity between Controller, Driver and Motor 41

3.3 Bond Graph Modelling of Bi-Directional Movement Setup of GMAW 42

3.3.1 Bond Graph Modelling in Single Direction 44

3.3.2 Bond Graph Modelling in Two Directions 46

3.4 System Response 47

3.4.1 Bond Graph Response in Uni-Direction Motion 47

3.4.2 Bond Graph Response in Bi-Directional Motion 50

Chapter 4: Layer Deposition with Different Build Strategies 55–112

4.1 Performance Analysis of Semi-Automatic Movement Setup 55

4.1.1 Chemical Composition of Workpiece and Sample Preparation 56

4.1.2 Validation of System accuracy with Equal Speeds in Both Directions 57

4.1.3 Validation of System accuracy with Unequal Speed in *X* and *Y* Direction 64

4.1.4 Comparison of Weld Bead between Experimental and Simulation Results 68

4.2 Single Layer Bead Deposition of Open and Closed Profiles 70

4.2.1 Chemical Composition of Workpiece and Sample Preparation 71

4.2.2 Weld Bead Geometries of Different Profiles 72

4.2.3 Bead Deposition with Different Profiles 73

4.2.4 Comparison of Weld Bead in Experiments and Simulation 80

4.3 Multi-Layer Bead Deposition of Open and Closed Profiles 81

4.3.1 Chemical Composition of Workpiece and Sample Preparation 82

4.3.2 Different Open and Closed Profiles 83

4.3.3 Bead Deposition with Different Profiles 84

4.4 Multi Layer Bead Deposition with Different Build Strategies 98

4.4.1 Chemical Composition of Workpiece and Sample Preparation 99

4.4.2 Testing of Deposited Specimens 101

4.4.2.1 Analysis of Tensile and Bending Strength 104

4.4.2.2 Analysis of Microhardness 106

4.4.2.3 Microstructural Analysis 107

Chapter 5: Joining of Dissimilar Stainless Steels using Activated Fluxes 113–128

5.1 Effect of Activated Fluxes during Welding of Dissimilar Stainless Steels 113

5.2 Chemical Composition of Workpiece and Sample Preparation 115

5.3 Selection of Orthogonal Array and Factors Assignment 116

5.4 Analysis of Variance 117

5.5 Welding and Testing of Dissimilar Stainless Steels 118

5.6 Techno-Economic Aspect 127

Chapter 6: Conclusions 129–132

6.1 Conclusions 129

6.2 Scope for Future Work 131

References 133–143

Curriculum Vitae 145

Chapter 1
Introduction

Welding is a part and parcel of our daily life. From kitchen utensils to aeroplane, welding is essential for their manufacture. Scope of welding extends from the simplest manual metal arc welding done in atmospheric pressure to underwater (Hyperbaric) welding carried out on ships, oil platforms, dams and other marine structures. Hyperbaric welding is of immense economic value as no other procedure in the similar conditions will work. Welding is an efficient and highly economical manufacturing process. It has replaced many of the earlier used processes which were inefficient and non-universal in nature.

Welding is the joining process for metals and non-metals through fusion such that bonding takes at faying surfaces. Fusion may be caused by heat or pressure or both; the filler metal may or may not be used. The different heat sources for fusion may be electric arc, high energy beams, exothermic and chemical reaction. The end result of welding is continuity of homogeneous material composition and characteristics of the two parts which are being joined together.

1.1 Joining and Metal Deposition

There are various methods of joining metals other than welding but joining with welding is a permanent method. A variety of techniques (refer Fig. 1.1) are available which can be performed welding similar or dissimilar metals by manual, semi-automatic and automatic process. There are several issues associated with the manual welding process such as non-uniform metal deposition, uneven bead geometry, poor weld quality and non-uniform heat input due to variation in electrode to workpiece distance. Automation in welding can eliminate these issues and provide good quality weld with consistency in heat input consequently deeper penetration. Automotive, aerospace and rapid tooling industries demand high geometrical accuracy and surface finish meeting the specific requirements. Bead geometry plays a vital role to define the weld quality and joint strength and these are influenced by welding process parameters. Furthermore, automatic path planning in execution is an essential aspect of welding in automation. There are various techniques available such as vision-sensing system, passive vision sensing

technology and infrared pyrometry sensing technique which can be implemented to automatically identify the weld bead path and control the bead geometry online. To realize multi beads, multi-layer deposition offset distance during overlapping of beads defines the deposition quality in terms of dense structure. Several techniques i.e., selective laser sintering (SLS), controlled metal buildup (CMB), shape deposition manufacturing (SDM) and selective laser melting (SLM) are available to deposit complex shaped components layer upon layer to produce prototypes and functional parts with good surface finish and high dimensional accuracy.

1.2 Classification of Welding Processes

There are various types of welding techniques used for making a weld joint. Welding processes can be classified into two main groups i.e., fusion welding and pressure welding according to the method of generation of heat and application of pressure. These two broad groups involve a number of welding processes having special characteristics and areas of applications. Figure 1.1 depicts all significant welding and associated processes which are generally used in the industries.

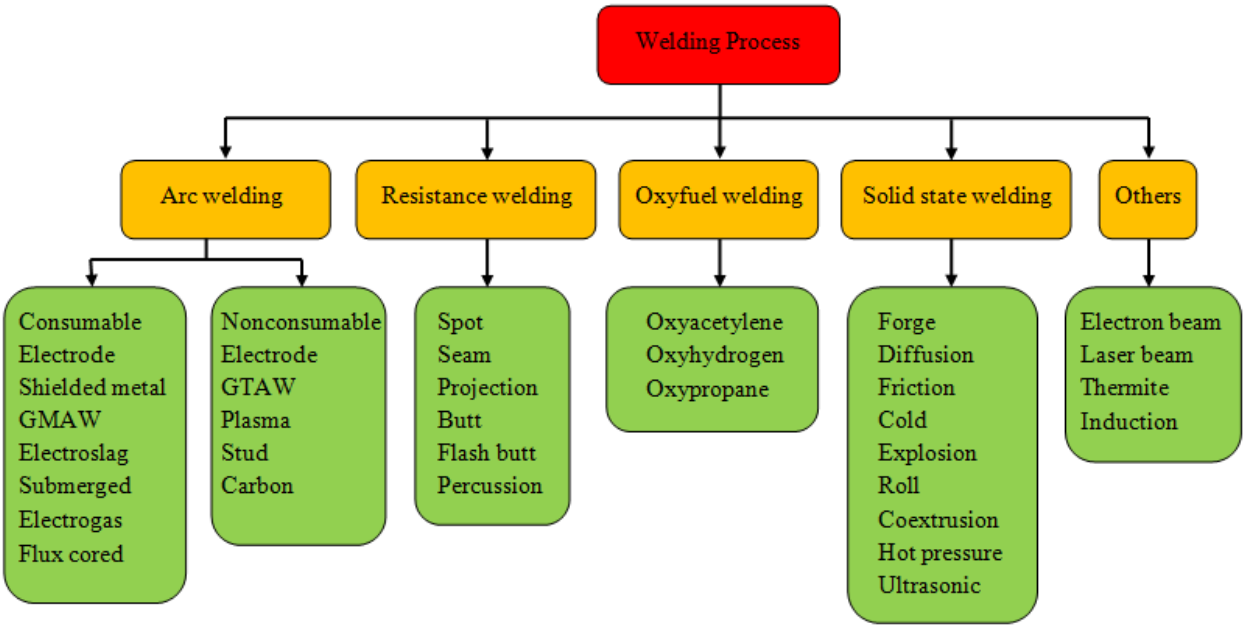

Figure 1.1 Classification of welding processes

Gas metal arc welding (GMAW) is a welding process in which heat for fusion is generated by an electric arc formed between continuously fed consumable electrodes, shielded with inert gas and a workpiece. Arc and welding zone are shielded from atmospheric contamination by the shroud of inert gas or active gas or mixture of both as shown in the Fig.1.2.

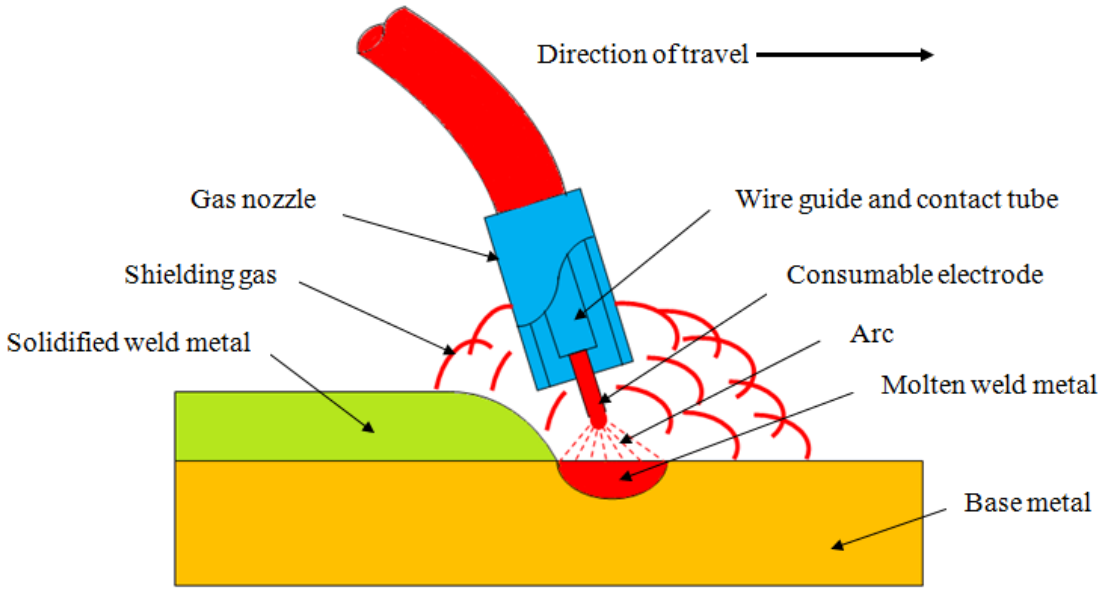

Figure 1.2 Gas metal arc welding operation

The process is also referred to as MIG or CO_2 welding. New developments in the process include application to a broader range of materials, operation at low current densities and pulsed direct current and the application of reactive gases, specifically CO_2, or gas mixtures. Owing to the new developments in the process and with the use of both inert and reactive gases, it is formally accepted the term GMAW for the process. The term MIG welding is more frequently used than GMAW. MIG welding is utilized in both semi-automatic and automatic modes. Gas metal arc welding setup consists of a constant voltage power supply, welding gun, a shielding gas cylinder and a wire feed control unit which pulls the wire electrode from a spool and pushes it through a welding gun as depicted in Fig. 1.3. It is employed particularly in high production welding projects owing to the continuous supply of wire electrodes. Most commercially available metals such as carbon steel, stainless steel, copper and aluminium can be suitably welded with

MIG in all positions by selecting the appropriate shielding gas, wire electrode and welding conditions.

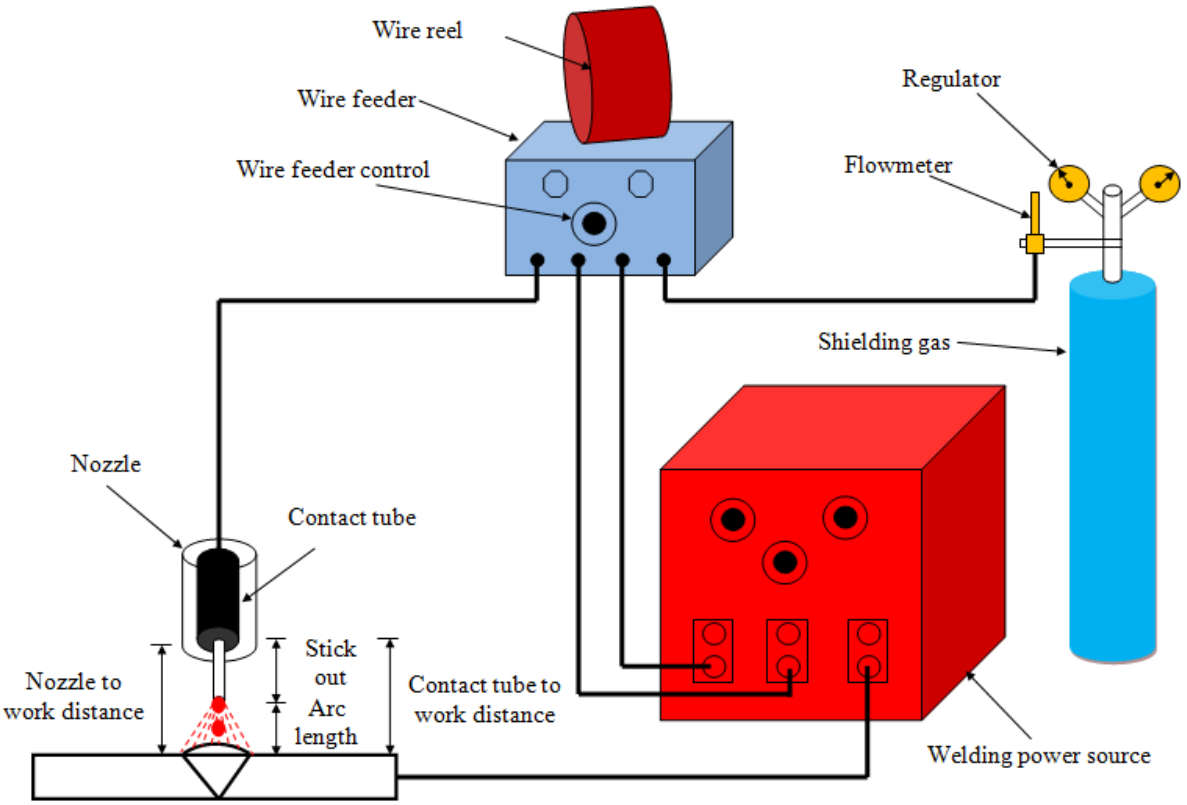

Figure 1.3 Gas metal arc welding setup

1.3 Different Metal Deposition Methods

Complex shaped functional components can be built using additive manufacturing (AM) with high geometrical accuracy and surface finish to meet the specific requirements of automotive, aerospace and rapid tooling industries. As manufacturing of thin-walled objects is the toughest task to deal with such issues, various mathematical models are available to implement during AM. Furthermore, AM can also be used to deposit complex thin-walled components having the ability to be ready to use by providing extra features of aligning the overhanging layer over layer. Material shortage at edges of the second layer and subsequent layers during deposition by overlapping layers should be

considered with attention as it would define the deposition quality. Surface finish after deposition during AM is the most desirable aspect. AM offers high deposition rate, higher material and power efficiency which makes this process demanding. In AM the multi bead multi-layer components are fabricated by overlapping the consecutive beads [Ding *et al*., 2015; Xiong *et al*., 2017; Xu *et al*., 2018; Panchagnula & Simhambhatla, 2018].

Wire and arc additive manufacturing (WAAM) is used to deposit 2D and 3D intricate profiles in metal deposition using various welding techniques. In WAAM, parts are constructed layer by layer using different metals for deposition. To eliminate the human intervention in different activities during WAAM, various techniques are used to make the entire process automatic including slicing of CAD model, tool path generation, selection of optimal bead profile and process variables for deposition. WAAM can significantly enhance deposition efficiency and consequently reduce the wastage of material, energy and production time [Kazanas *et al*., 2012; Haden *et al*., 2017; Ogino *et al*., 2018; Shi *et al*., 2019].

A hybrid layered manufacturing (HLM) technique is used to fabricate parts by weld deposition and machined subsequently for removing irregularities to obtain near net shape and enhance the accuracy of fabricate 3D parts. Both additive and subtractive processes can be performed on the single CNC setup with additional fitted attachments which lead to proper utilization of space. In HLM technique, gas metal arc welding (GMAW) may be used as additive and conventional machining as a subtractive process on the same CNC machine by rotating the attachment alternatively for deposition and reshaping. The cost of an additional actuator is saved by performing both operations on the same machine. Furthermore, to facilitate the additive and subtractive processes, a multi-axis single workstation can be used for depositing complex internal and overhanging features with high dimensional accuracy and good surface finish. Offset distance, torch travelling speed and wire feed rate are important factors which need to be controlled optimally for depositing the parts with inclination features. Angle of inclination increased with increase of torch travelling speed and decreased with increase

in wire feed rate [Song *et al*., 2005; Karunakaran *et al*., 2010; Lee *et al*., 2014; Flynn *et al*., 2016].

Direct freeform fabrication (DFF) technique is used to build metallic parts using different build strategies by additive and subtractive combined process. In this technique, the GMAW process is used to deposit a layer and machined subsequently to enhance the dimensional accuracy of the deposited parts. With the optimization of process parameters, using methods of the DFF technique can be extended to fabricate complex prototypes [Song *et al*., 2005].

Solid freeform fabrication (SFF) based RP is a technique used to fabricate complex shaped parts which are otherwise difficult with traditional techniques. In SFF, the CAD model is converted into tangible products without actually using any tooling. Furthermore, the CAD model is sliced and subsequently each layer is realized at time without human intervention. However, the dimensional accuracy and surface finish of SFF parts are less than machined parts. This issue can be resolved by implementing a combined additive (welding) and subtractive (machining) techniques [Song *et al*., 2006].

Selective laser sintering (SLS) based AM is introduced to fabricate three-dimensional printed parts with the aim of reduction in weight as compared to conventional milling process. In SLS, a laser as an energy source is employed to point automatically according to the designed model, melting the material layer by layer. It is observed that the SLS part has reduced the 50% weight in comparison to conventional manufactured parts and can be fabricated in a single piece which is otherwise not possible with conventional processes [Ferro *et al*., 2017].

1.4 Process Parameters for GMAW

During welding operation, it is essential to control over the welding parameters which influence the depth of penetration, bead geometry and hence weld quality. The suitable selection of welding parameters increases the chances of producing welds of a desired quality. However, these parameters are interdependent and changing one parameter generally requires the changing of some of the others in order to obtain the desired result. If all these parameters are optimum, the welder can deposit higher quality weld metal and

produce sound weld joints. The selection of the welding parameters should be made after the workpiece material, filler metal and joint type have been determined. The welding process parameters specifically affect the geometry of the weld bead such as the penetration depth, bead reinforcement, weld bead width and the deposition rate which is the weight of the metal deposited per unit time. Some of the following important parameters are explained in detail [Rao, 2009].

- **Welding current**

  Selection of welding current depends upon various factors such as thickness of workpiece, electrode size, type of metal transfer and electrode feed rate. With the increase of electrode size and feed rate, welding current needs to increase for better welding results. High welding current results in deeper penetration and high deposition rate.

- **Arc voltage**

  The arc length is the most significant parameter in MIG that must be kept under control. High arc voltage may influence the shielding gas which results in wandering of arc and thus, affects the bead geometry and the penetration. Arc voltage also determines the type of metal transfer during welding.

- **Arc travel speed**

  The speed at which the welding arc moves along the path profile to be welded is defined as arc travel speed. With the increase of arc travel speed, weld bead width and penetration depth are reduced whereas, slower arc travel speed results in higher deposition rate.

- **Electrode size**

  The selection of electrode size depends upon the thickness of the workpiece to be welded. Electrode size affects the bead geometry and depth of penetration because different electrode sizes demand different welding current.

- **Electrode extension or stick-out**

  It is the distance between the contact tube and the tip of the electrode. Usually, stick-out may be kept between 16–20 mm. Too short stick-out may lead to excessive spatters produced during welding and get deposited on the tip of the nozzle. It can cause restriction in shielding gas supply and consequently porosity.

On the contrary, too long stick-out may lead to shallow penetration depth and poor weld bead with unstable arc.

- **Electrode position**

  Electrode position can be inclined to the workpiece or perpendicular in the direction of weld deposition. The electrode angle is generally kept within 10˚–20˚ on either side of the perpendicular position.

1.5 Bond Graph Technique for System Modelling

Different computational tools like MATLAB, Bond graph or Finite element modelling can be used to predict temperatures at different layers of metal deposition using the present setup. This model may be based on the fundamental equations of heat transfer and the high temperature metallurgical reaction kinetics. These computational tools may also be used to predict stresses at different parts of the metal deposited layers. The various optimization methods on the different welding process parameters can be applied to define the desired output variables using design of experiment (DOE) technique, Taguchi technique and statistical approaches for optimization. As there are different process parameters (welding current, voltage, gas flow rate, filler wire speed, base materials, types of activated flux etc.) of welding, single variable or multi-variable optimization technique with certain objective function may be used.

The bond graph is a system modelling approach based on conservation of power. This technique is useful if the components of the system lie in different energy domains. Only the kinematic equations are required for modelling any system using bond graph and the dynamic equations are automatically developed from the model. The bond graph modelling technique is very much algorithmic depending on the assignment of causality (relationship between cause and effect) in it. The modelling of any system is essential to understand and analyze the system responses for different inputs to the system. The bond graph modelling technique is unique or compact in nature i.e., only 7 elements (Inertial element (I), Compliance element (C), Resistive element (R), Transformer (TF), Gyrator (GY), Source of effort (Se) and Source of flow (Sf)) and 2 junctions (1 and 0 junction) are required to model systems residing in different energy domains (e.g., electrical, mechanical, chemical, thermal, hydraulic, financial system *etc.*). I, C and R are generally

single port (i.e., single bond connects these elements) passive elements (i.e., no power is generated) but, TF and GY are the two-port scaling elements. Two signals move along the bond (as the bond graph is bi-directional) which is represented by a line with a half arrow. The causal stroke (vertical line on the bond) indicates the direction of the effort signal and flow signal moves in the opposite direction of the bond. The causality of the storage elements (I and C element) is fixed. The junction elements (1 and 0 junctions) and converters (TF and GY elements) have constraints in causality. Only the causality of the free causal element (R element) is determined depending on the causality of other elements. Algorithms can be established easily assigning causalities to the bond graph elements and the system responses can be obtained quickly. The bond with a full arrow is called the information bond and this is used to add sensors in the system and this sensor provides output/response values. 1-junction is required to indicate equality of flow variables i.e., current, linear velocity or angular velocity. Similarly, 0-junction is used to denote equality of effort variables i.e., voltage, force or torque. Another advantage of BG modelling is that no dynamic equation is required for modelling any system and system equations can be derived from the model based on junction laws.

1.6 Background and Motivation

From the past few decades, automation in the developed industries for widespread engineering applications is helpful to improve the productivity and quality of tangible products as well as to reduce the scrap and labour cost. The automation in welding is capable of producing defect-free welding and reduces the lead time using thin as well as thick plates suitable for enormous applications like ship building, structural members, pressure vessels, tanks, pipes, automotive components *etc*. Weld depositions of intricate shapes desired by different applications involved in the advanced industries. Furthermore, the unique application of welding as 3D metal deposition is tremendously used for building products by layer over the layer deposition for various engineering applications. Metal deposition is an innovative concept to build high quality intricate 3D functional engineering products (prototypes and tooling) using robots and CNC machines. Automatic gas metal arc welding (GMAW) technique provides dimensional accuracy in weld bead, uniform heat input and penetration depth owing to constant contact tube to

work gap and constant speed of welding torch. However, owing to the high initial capital cost of robotic welding arms and CNC machines, they make the process unnecessarily expensive. This motivates the researchers to make cheaper automatic welding machine which may be used for metal 3D printing of different components.

1.7 Significance of the Research

3D complex shaped parts fabricated by additive manufacturing process offers enormous advantages such as high deposition efficiency, higher surface finish, fully dense structure, high dimensional accuracy and parts with overhanging features over conventional machined parts. In order to meet the increasing demand of the developing industries, several techniques such as laser-enhanced GMAW, WAAM, adaptive process control scheme (APCS), twin-wire GMAW, tandem laser GMAW have developed to enhance the metal deposition efficiency and process capabilities i.e., uniform bead geometry, deeper penetration and dense structure, however, these techniques involve expensive tooling and machinery i.e., dedicated robots and CNC machines. In this work, bi-directional automatic setup is designed and fabricated for GMAW with the aim to deposit weld beads of desired profile at given trajectory and print 3D metal products with least process steps, with reasonably well and acceptable weld bead quality without requirement of post-weld machining at significantly lower price.

The originality of the research work in the Thesis lies in the fact that the designed and developed bi-directional automatic movement setup which is used in this research work to obtain weld with uniform bead width along a desired path during GMAW is simple, indigenous, accurate and inexpensive. This setup has the capability to perform vertical layer deposition for different open and closed profiles utilizing gas metal arc welding. The developed machine is suitable for effectively tracking the reference path and executing welding of any shape. The constant contact tube to work distance is provided by the automated fabricated setup. Another novelty of this work is to perform system modelling of the fabricated setup using a bond graph technique to predict different system behaviour as well as to predict the weld bead geometric path.

1.8 Contribution of the Thesis

The significant contributions of work presented in thesis are as follows:

- A bi-directional automatic movement unit for planar welding is indigenously designed and developed in order to obtain weld with uniform bead width along a desired path at significantly lower price.
- In order to achieve the precise controlled movement of the welding torch during welding and metal printing on low carbon steel, electronic circuitry based on GRBL control is involved. The power supply is given to the SMPS and output from it is fed to the DM542 motor driver. The desired trajectory is written using G-code programming and this is fed to the Arduino UNO through serial manipulator. Motor drivers are used to control the two actuators (stepper motors) and the Arduino controls the drivers. The stepper motor drives the lead screw mounted on the setup which further enables it to perform the desired motion.
- System modelling of the fabricated setup is carried out using bond graphs to predict different system behaviours as well as to predict the weld bead geometric path. The effectiveness of the automatic planar movement setup is validated depositing weld beads at different speeds on low carbon steel workpiece.
- An indigenously fabricated bi-directional semi-automatic movement setup for GMAW is used for deposition of closed profiles (e.g., circular, elliptical) and opened profiles (e.g., spiral and S-shape). The bead width variations, geometric paths of different geometric shapes are measured and validated along with the microstructural characterizations of the base metal, heat-affected zone and welded zone.
- Bi-directional automatic movement setup was used to perform vertical layer deposition for different closed profiles i.e., cylindrical, elliptical and concave as well as open profiles i.e., semi-cylindrical, double semi-cylindrical and V-profile utilizing gas metal arc welding. The movement of the welding torch along the vertical direction is given manually whereas the motion of the welding torch in the horizontal plane is completely automatic.

- Planar welding was implemented to build three-dimensional specimens through different paths strategies for deposition i.e., spiral-in (circular and square), raster (Square, diagonal and circular). The given trajectory was followed to deposit metal layers over the layer for producing positive slope on the lower-half and negative slope on the upper-half section.

- The microstructural and mechanical properties of the dissimilar metals i.e., austenitic (AISI 304, AISI 316) and duplex 2205 stainless steels, welded using activated fluxes, were investigated using semi-automatic bi-directional GMAW setup. Three different activated fluxes i.e., SiO_2, TiO_2 and CrO_3 were used to enhance the depth of penetration during joining of different grades of stainless steels.

- Various process parameters such as welding current, voltage, filler wire, gas flow rate and activated flux were varied to observe their influences on tensile strength, bending strength, microhardness and microstructural properties. Optimization of the process parameters and experimental conditions were designed according to the L_{18} orthogonal array of Taguchi method.

1.9 Organization of the Thesis

The thesis is presented in six chapters in total including this chapter followed by a list of references referred in this work. An outline of the role of the contents of each chapter has been given as following:

Chapter 2 describes an extensive review of the literature pertinent to fabrication of three-dimensional metals printing products of regular or irregular shapes using various techniques such as wire and arc additive manufacturing (WAAM), hybrid layered manufacturing (HLM), rapid manufacturing (RM) and Shaped metal deposition (SMD) and other advanced techniques in AM. Literature on the influence of various process parameters on mechanical properties and microstructural characterization during gas metal arc welding is also explained in this chapter. This chapter also includes the literature related to several techniques adopted to enhance the metal deposition efficiency and process capabilities i.e., uniform bead geometry, deeper penetration and dense structure. Literatures on different difficulties in AM, thermal behaviour in AM, dissimilar

metals joining, effects of activated fluxes in welding and system modelling using bond graph technic are also discussed in this chapter. Finally, objectives of the present work have been identified from observations revealed in the literature.

Chapter 3 presents the design and development of a bi-directional automatic movement GMAW setup in order to obtain weld with uniform bead width along a desired path. The computer-aided design (CAD) model and a prototype, block diagram of the complete setup and connections between controller, drivers and stepper motors are presented in this chapter. Furthermore, system modelling of the fabricated setup using bond graph (BG) modelling approach to predict different system behaviours as well as to predict the weld bead geometric path is also discussed.

Chapter 4 deals with the sequence-wise procedures of different experiments performed using fabricated setup. Bead deposition along the desired trajectory and vertical layer deposition for different open and closed profiles utilizing automatic (GMAW) setup are discussed in detail. Metal deposition to build three-dimensional specimens with varying cross-sections through different paths strategies i.e., spiral-in (circular and square) and raster (square, diagonal and circular) is also presented. Subsequently to enhance the versatility of the fabricated setup, three-dimensional components having negative and positive slopes were deposited using different path strategies. To gain more insight into the mechanical properties and microstructural characterization of the deposited specimens, different testing techniques such as tensile test, bend test, microhardness test, spectroscopy, scanning electron microscopy (SEM), energy dispersive x-ray (EDX) are explained in detail.

Chapter 5 highlights the joining of dissimilar stainless steels by varying the bead geometry using an indigenously designed and fabricated bi-directional semi-automatic movement setup for GMAW. Taguchi's factorial design of experiments is presented to design experiments and analysis of variance (ANOVA) is implemented for subsequent analysis. The effects of three activated fluxes (SiO_2, TiO_2 and CrO_3) on penetration depth during joining of different grades of steels i.e., austenitic AISI 304/ 316 and duplex 2205 are explained. Furthermore, the effects of welding process parameters are also studied.

Chapter 6 contains the major conclusions from this research work and provides scope for future work in the selected subjects.

Subsequently, a list of references alphabetically arranged pertinent to the whole thesis is presented in the end. These references have already been cited at the relevant places in all chapters of the thesis.

Chapter 2

Literature Review

The consequences of a research work become more significant when pertinent literature is reviewed and analysed. In this chapter, the literature review is carried out to provide an overview on various welding profile formation and 3D metal printing techniques employed for fabricating metallic components using different welding processes. Afterwards, the literature on influence of various process parameters on bead geometry, depth of penetration, mechanical properties and microstructural characterization during gas metal arc welding (GMAW) is also explained in this chapter. This chapter also includes the literature related to several techniques adopted to enhance the metal deposition efficiency and process capabilities i.e., uniform bead geometry, deeper penetration and dense structure. Later on, a detailed literature review on dissimilar joining between various ferrous and non-ferrous metals in the presence of activated fluxes following Taguchi fractional factorial design of experiment (DOE) technique is carried out. Finally, the objectives of the present work have been summarized after finding observations made on the basis of existing literature. Literature related to bond graph modelling technique is also reviewed as the system modelling for the developed setup is done using bond graph technique. The detailed literature review of the Thesis work is categorized into seven sections and is presented here:

1. WAAM based rapid prototyping
2. Other rapid prototyping techniques
3. Different difficulties in AM
4. Advanced techniques in AM
5. Thermal behaviour in AM
6. Influence of process parameters on metallic properties
7. Dissimilar metals joining

8. Effect of activated fluxes in welding

9. Bond graph modelling

2.1 WAAM based Rapid Prototyping

Gas metal arc welding (GMAW) is a joining and deposition process which is widely employed for depositing intricate profiles in almost every industry. Various novel techniques are implemented to enhance the process capabilities by making the process automatic. However, in order to make the system automatic, expensive machines such as robotics arms and CNC are generally involved. To deal with such an issue, a simple and economic setup is the best alternative. Bead geometry plays a significant role and it largely depends upon the welding process parameters. This section reflects the contribution of various researchers in the field of path planning, prediction and deposition using different modes of engineering.

Rapid prototyping (RP) or rapid manufacturing (RM) or additive manufacturing (AM) is a unique technique which is generally employed to build components using different RP techniques such as direct metal laser sintering (DMLS) [Simchi *et al*., 2003], electron beam melting (EBM) [Heinl *et al*., 2008], selective laser melting (SLM) [Kruth *et al*., 2004], electron beam freeform fabrication (EBF) [Taminger *et al*., 2003], wire and arc additive manufacturing (WAAM) [Wang *et al*., 2013] and powder bed and inkjet 3D printing (3DP) [Utela *et al*., 2008]. In RP technique, the whole model is sliced into desired thickness and a single layer is realized at a time for deposition. However, the functional capabilities of polymeric components are not adequate. Laser sintering is a suitable option for fabricating functional components but, its expensive equipment cost is a major hurdle to adopt this technique. An economical alternative suggested [Zang *et al*., 2003] to deal with this issue is GMAW based rapid prototyping manufacturing which involves controlling the metal transfer by optimizing the process parameters for improving the bead geometry. The bead geometry can be easily controlled in wire and arc additive manufacturing (WAAM).

Wire and arc additive manufacturing (WAAM) is employed to fabricate metallic objects layer by layer by vertically keeping the welding torch over the work table

moveable and this leads to accessibility problems. To resolve this problem inclined objects are fabricated by positioning the welding torch and keeping the stationary work-table. It is mentioned that travelling speed of welding is a significant factor which influences the weld quality of deposited objects [Kazanas *et al*., 2012]. Metal deposition by micro droplets is a novel technique [Qi *et al*., 2012] with proper overlapping and bonding strength of metallic droplets is obtained during fabrication of functional objects. It is observed that proposed models are influenced by solidification angle and droplet diameter. Various models can be useful to predict weld bead profiles for obtaining higher density structure, better surface finish and accuracy during single and multi-bead deposition. Xiong *et al*. [2013] presents three models i.e., parabola, circular arc and cosine function to build parts optimally with high quality using GMAW based RP. It is studied that at higher welding speed, circular arc model whereas parabola model at low welding speed exhibit better surface finish. In WAAM, surface quality and dimensional accuracy are important aspects during deposition of single bead as well as multi beads. To achieve this, overlapping geometry models for single bead and multi beads are developed through different curve fitting techniques. Cosine and parabola functions for single bead deposition and tangent overlapping model for multi bead deposition are successfully proved [Ding *et al*., 2015]. WAAM technique [Haden *et al*., 2017] is used to deposit 2D and 3D intricate profiles in metal deposition using various welding techniques. Owing to the variation in thermal histories at different layers, variation in wear and hardness is observed. GMAW based WAAM may be applied to build intended near net shape structure with reasonable accuracy. GMAW based weld pool model [Ogino *et al*., 2018] is presented to numerically investigate the deposition conditions for controlling the bead geometry. It is observed that inter-pass temperature and welding torch motion influence the deposition shape. WAAM process may also be employed to build complex parts using aluminium alloys. Despite of issues regarding hot cracking and gas porosity, this process can be feasible with further optimization. Better mechanical and microstructural properties demonstrate the successful implementation of WAAM process on AA5183 aluminium alloy [Horgar *et al*., 2018]. WAAM can also be used to deposit steel plates by layer over the layer without distinguished boundaries exhibited anisotropic mechanical properties i.e., samples prepared at 45˚ orientation showed higher tensile

strength in comparison to the samples at 0˚ and 90˚ orientation [Duraisamy *et al*., 2019]. Tandem gas metal arc welding (T-GMAW) process [Shi *et al*., 2019] is a suitable alternative to deposit wider bead width of desired trajectory during WAAM which significantly enhances deposition efficiency and consequently reduce the wastage of material, energy and production time. In T-GMAW, two individual power sources are used to transfer metal for deposition. The diameter and material of filler may be same or different for two welding torches.

2.2 Other Rapid Prototyping Techniques

Rapid prototyping technique was originally developed for printing of non metallic components. Gradually this technique attracts engineers towards metallic near net shape products manufactured by layer upon layer strategies using different sources of heat i.e., laser beam, electron beam and electric arc. Many researchers have been contributing to make this technique more useful.

Direct freeform fabrication technique is used to build metallic parts using different build strategies by additive and subtractive combined process. In this technique, GMAW process is used to deposit a layer and machined subsequently to enhance the dimensional accuracy of the deposited parts [Song *et al*., 2005]. A hybrid process [Song *et al*., 2005] is explored in which GMAW is applied as additive and subsequently milling as subtractive technique to enhance the accuracy of fabricate 3D parts. Both additive and subtractive processes are performed on the single CNC setup with additional fitted attachments which led to proper utilization of space. Solid freeform fabrication (SFF) based RP [Song *et al*., 2006] is a technique used to fabricate complex shaped parts which are otherwise difficult with traditional techniques. However, the dimensional accuracy and surface finish of SFF parts are less than machined parts. This issue can be resolved by implementing a combined additive (welding) and subtractive (machining) techniques. 3D micro gas tungsten arc welding-based RP [Horii *et al*., 2008] is employed to build metallic parts. Wide ranges of metals and alloys may be used in this technique. Ti-Al alloy possess superior chemical and mechanical properties whereas forming process is complex and expensive. To avoid this issue, 3D micro printing can be implemented using Ti-Al alloy. Metal direct RP [Xiong *et al*., 2009] is a technique in which deposited

objects are machined subsequently to achieve the surface finish and dimensional accuracy similar to the conventional machining process. The machining removes the staircase impressions developed during RP to ensure dimensional integrity. A hybrid layered manufacturing technique [Karunakaran *et al.*, 2010] is used to fabricate parts by weld deposition and machined subsequently for removing irregularities to obtain near net shape. Low-cost attachment fitted on the same CNC machine to make the process economical. Hybrid layered manufacturing (HLM) based RP process [Somashekara *et al.*, 2011] is presented to fabricate parts by weld deposition in layers. In HLM, overlapping of beads during multi beads deposition leads to scales and scallops which are removed by subsequent machining process after each layer to ensure the dimensional accuracy in the vertical direction. It is observed that during single bead deposition, bead geometry is influenced by wire speed, welding torch speed and size of filler wire while during multi beads deposition, offset distance between consecutive beads is a significant factor. Metal active gas welding-based RP [Cao *et al.*, 2011] is another suitable alternate to deposit metallic objects with satisfactory surface finish. Bead geometry has significant purpose while depositing single bead or multi beads with overlapping feature. In this work, a mathematical model is proposed and analyzed to examine the optimum bead geometry and overlapping between two consecutive beads. A hybrid RP system is developed by Lee *et al.* [2014] to take the advantages of both RP and conventional machining processes using a five-axis machine. Fused deposition modelling (FDM) is used as additive and machining as subtractive process on the same five axis machine by rotating the attachment alternatively for deposition and reshaping. The cost of additional actuator is saved by performing both operations on the same machine. It is observed that the stiffness of FDM part with embedded metal part is increased. Selective Laser Sintering (SLS) based AM [Ferro *et al.*, 2017] is introduced to fabricate three dimensional printed parts with the aim of reduction in weight as compared to conventional milling process. It is observed that SLS part reduces the 50% weight in comparison to conventional manufactured part and can be fabricated in a single piece which is otherwise not possible with conventional process. Plasma transferred arc-based AM system [Mercado Rojas *et al.*, 2018] is employed to build 3D objects of different solid and hollow shapes. The plasma torch of the system is fixed whereas the table for

AM is moveable according to the given profile. Plasma based AM is a high energy process. Tungsten carbide-based metal matrix composites AM parts have better wear resistance which may lead to extending the life of components such as crushers, bucket teeth and shovels.

2.3 Different Difficulties in AM

Owing to growing necessity of ready to use metal printing components, it becomes challenging to overcome all those difficulties associated with AM. The literature related to problems and their suitable solutions offered by the few researchers are presented in this section.

Complex shape functional components can be built using AM with high geometrical accuracy and surface finish to meet the specific requirements of automotive, aerospace and rapid tooling industries. Residual stresses and distortions of components owing to excessive heat accumulation can be controlled by optimizing the process parameters [Ding *et al*., 2015]. After 3D metal printing, releasing of object from substrate is a problem during AM. A substrate release mechanism can be implemented to facilitate the releasing of substrate by providing coating of boron nitride, aluminium oxide and titanium nitride with minimum impact energy. Apart from this, modified welding condition, welding without shielding gas, use of aluminium-iron compounds for printing first layer may also facilitate the releasing of substrate without using cutting tools [Haselhuhn *et al*., 2015]. It is challenging to fabricate components with overhanging features without additional support during AM. Hence, a novel approach [Panchagnula & Simhambhatla, 2016] is developed to realize the complex shape overhanging features without the requirement of additional support. Use of higher order kinematics and order of placing the overhanging features during deposition made the process possible. Furthermore, non-uniform slicing and area filling are significant concepts which are required to realize during deposition. Double electrode GMAW based AM [Yang *et al*., 2016] is used to fabricate thin-walled components. Constant voltage and constant current power sources are used for GMAW and GTAW torches, respectively. Constant current power supply acted as bypass current supply. Material utilization is enhanced by controlling the weld bead width and height by adjusting the welding bypass current. The

sharp corners and the non-uniform deposition between the adjacent layers can be reasons of low quality and poor surface finish. This issue is addressed by utilizing path planning technique optimally for printing metallic objects during AM [Jin *et al*., 2017]. As manufacturing of thin-walled objects is the toughest task to deal with such issues, a mathematical model is proposed by Panchagnula & Simhambhatla [2018]. AM is used to deposit complex thin-walled components having the ability to be ready to use by providing an extra feature of aligning the overhanging layer over layer. AM offers high deposition rate, higher material and power efficiency and these make the process demanding in the industry. Surface finish after deposition during AM is the most desirable aspect. Oxide accumulation in the fusion zone may deteriorate the surface finish and may raise the possibility of porosity on layer over layer-built structure. Oxide formation also affects the arc stability and may result in poor layer dimensional accuracy. Oxide accumulation mechanisms [Xu *et al*., 2018] are employed to study the behaviour of molten pools in terms of wetting and spreading during deposition. 3D metal printer [Nilsiam *et al*., 2018] is employed for GMAW based AM of metallic parts with hanging features without support and high density. 3D printer is capable to fabricate high resolutions parts of near net shape by using steel and polymer together for special applications. Energy consumption during metal printing through AM is a serious concern and this influences the microstructure and subsequently mechanical properties of the deposited parts. In AM, energy is consumed at two levels i.e., machine and process level. Machine level energy can be computed through subsystems i.e., high energy source, control system, cooling setup *etc*. The process level energy can be calculated through energy flow consumption in AM process [Liu *et al*., 2018]. GMAW based AM is also implemented to build multi bead multi-layer components by overlapping the consecutive beads. Material shortage at edges of second layer and subsequent layers during deposition by overlapping layers is necessary to pay attention. A mathematical formulation is proposed to compensate the material shortage and consequently improve the dimensional accuracy. Problem of material shortage at edges can be resolved by modifying the process parameters during deposition [Li *et al*., 2018]. Cold metal transfer is a variant of GMAW and utilizes low heat to deposit beads over beads during AM. The reshaping and stabilization of the titanium weld bead is carried out by laser beam. Laser beam stabilized

the deposition process and improved the deposition rate and weld bead geometry of titanium during multi-layer deposition [Pardal *et al*., 2019].

2.4 Advanced Techniques in AM

Various techniques and models have been developed and explained in this section to achieve high precision thin walled structures with high surface finish to prevent post machining process using AM. As bead profile has direct relationship with the structure formation quality and surface finish therefore, it needs to be controlled optimally.

Vision-sensing system-based AM [Xiong *et al*., 2013a] may be implemented to deposit single pass multi-layer components for saving the materials and energies during GMAW. In AM weld, bead geometry plays a significant role and therefore, bead geometry should be controlled precisely. In order to achieve a fully dense structure fabricated by AM, a passive vision sensing system [Xiong *et al*., 2013b] may be implemented using GMAW. This passive vision sensing system controls the bead geometry online using high-definition cameras for real time detection of the deposited beads. Accurate bead geometry plays a significant role for obtaining thin wall components. An advanced welding system including 3-axis workstation and vision sensing system is implemented by Caggiano *et al*. [2014] to deposit desirable weld bead profiles on the given path. This system has the capability to automatically select the process parameters according to the given weld joint geometry. System also offers automatic planning and collision detection for successful implementation of the process. A path planning strategy [Ding *et al*., 2014] may be employed to generate tool path for 2D geometries automatically during WAAM. This strategy first divide the whole path into small segments and then by scanning each segment optimally a continuous path is generated to form a closed profile. Path planning strategy can be implemented to reduced start and stop points during deposition with high quality surface finish. Neural network and second order regression method are proposed by Xiong *et al*. [2014] to predict the bead width and height for dimensional precision and good surface finish of deposited components during robotic GMAW. It is reported that neural network method more efficiently predicts the bead geometry than the second order regression model. In order to control the bead geometry, online image processing is to be carried out using vision-

sensing system. Passive vision sensing technology [Xiong *et al.*, 2015] is implemented to study the forming characteristics of single pass multi-layered objects using GMAW based AM. It is observed that welding current, deposition speed and heat input influence the forming characteristics of the deposited parts. In automatic welding, path generation for bead deposition is a crucial task during wire and arc additive manufacturing (WAAM). The quality of the fabricated product lies in the accuracy of path generation. The medial axis transformation (MAT) technique can be used to generate the weld bead path to fill the entire geometry without any gaps. By optimizing the step over distance, the material efficiency improved significantly [Ding *et al.*, 2015]. To eliminate the human intervention in different activities during WAAM, Ding *et al.*, [2016] developed the adaptive medial axis transformation (MAT) technique. In adaptive MAT, entire process is automatic including slicing of CAD model, tool path generation, selection of optimal bead profile and process variables for deposition. Artificial neural network (ANN) technique is used to develop a relationship between bead profile and welding process variables. It is observed that the adaptive MAT technique can be used to fabricate void free components with high quality and dimensional accuracy. To facilitate the additive and subtractive processes, a multi axis single workstation is developed for depositing complex internal and overhanging features with high dimensional accuracy and good surface finish [Flynn *et al.*, 2016]. An automated welding experimental setup having capabilities to accommodate different diameter of pipes is used to weld by varying various welding process variables such as wire feed rate, voltage, and gas flow rate to influence the mechanical as well as microstructural properties of the weldment [Sudhakar *et al.*, 2017]. The quality of weld made by automated experimental setup is improved by optimizing the output results using statistical analysis. GMAW based 3D metal printing [Nilsiam *et al.*, 2017] is performed to fabricate complex shape parts. In order to make the whole process efficient, an automatic technique is used to slice the 3D CAD model and subsequently generate the program automatically. It is observed that this technique has the capability to avoid overlapping movement on previous bead and keep the system idle for cooling before depositing layer.

2.5 Thermal Behaviour in AM

Thermal behaviour has significant impact on surface quality, dimensional accuracy and thermal distortions developed during printing of near net shape components with AM techniques. To address this issue different models and techniques have been developed and implemented by many researchers and presented in this section.

Infrared pyrometry sensing technique [Kwak *et al*., 2002] is used to thermally scan the bead deposition for controlling the bead geometry of near net shapes components. Thermally scanned technique reduces the thermal distortions and eliminates the subsequent machining requirements by monitoring the weld bead geometry. Wire feed rate is controlled by the feedback system of this technique to obtain desired weld bead width. Shaped metal deposition (SMD) [Clark *et al*., 2008] is employed to fabricate near net shape aero engine parts of nickel based alloy. It is reported that cooling rate affects the microstructure and careful consideration is necessary to minimize thermal stresses. It is essential to understand the thermal behaviour as it may be the cause of poor surface quality and reduction in actual height during single pass multi-layer deposition objects by additive manufacturing. A combined thermo-mechanical solution [Chiumenti *et al*., 2010] is implemented to tackle the problem of thermal stress, distortion and cracking by using phase change phenomena which revealed release of latent heat and effect of shrinkage during shaped metal deposition. It is reported that the proposed solution successfully simulates the evolution of temperature and distortion and validated experimentally. In the RP process while [Zhao *et al*., 2012] depositing single pass multi layered welded components, complex thermal stresses and residual stress are developed and these may lead to excess deformation and even cracking. The residual stress and residual strain can be investigated by implementing a finite element model. Maximum residual stress is developed in the last layer due to the stress release effect of the previous layers on the next layers. Twin wire welding-based AM [Somashekara *et al*., 2016] is used for building metallic parts during GMAW. This technique has high deposition rate and provides the freedom to use dissimilar filler wire material for deposition. Despite of these advantages, the matter of thermal stress which is also associated with deposition of multilayer parts needs to be taken care of. Finite element analysis method can be used to

analyze the thermal stresses developed during deposition using different area filling patterns. Fabrication of inclined thin-walled parts [Xiong *et al*., 2017a] is performed during GMAW based AM without using any additional support. The welding torch is kept perpendicular to the substrate during deposition. Offset distance, torch travelling speed and wire feed rate affects the inclination of deposition. It is reported that angle of inclination increased with increase of torch travelling speed and decreased with increase in wire feed rate. Residual stresses, distortion and uneven solidification cracking are the critical problems developed during fabrication of thin-walled parts by WAAM. To avoid these problems, a 3D heat transfer model [Xiong *et al*., 2017b] is studied to observe the influence of substrate preheating on thermal behaviour during deposition. It is reported that substrate preheating affects the thermal behaviour which led to slower cooling of the molten pool. Infrared thermography [Yang *et al*., 2017] technique is used to measure the surface temperature of a weld zone and subsequently, it controls the heat accumulation. However, the cooling rate can be increased by increasing the inter layer timing which will make the process unnecessarily time consuming. Three different welding techniques i.e., arc, laser, and electron beam welding can be used as AM for building parts layer by layer. Laser beam welding consumes minimum energy per unit length of weld bead followed by arc welding and electron beam welding [Elmer *et al*., 2020]. It is analyzed that heat input rate and cooling rate define the microstructure which further describes the mechanical properties of the deposited parts.

2.6 Influence of Process Parameters on Metallic Properties

From the experimental investigation, it has been observed that a careful selection of optimum process parameters is essential for desired welding results during metal printing. Each process parameter influences the mechanical as well as metallurgical properties of the deposited metallic components. In this section, a light on the relevant work carried out by various researchers is thrown.

It is very essential to understand the relationship between welding process parameters and bead geometry for achieving high precision in welding results. A mathematical model [Kim *et al*., 2003] is developed to predict the penetration depth for single pass bead deposition during CO_2 robotic welding. It is observed from the

experimental results that welding current, voltage, travelling speed and torch angle influence the penetration depth. Cold metal transfer (CMT) based GMAW [Ahmad & Bakar, 2011] is performed to investigate the influence of post weld heat treatment on mechanical properties and microstructural characterization during joining of AA6061. CMT process provides enormous advantages such as low heat input, spatter free joining, high quality weld and excellent gap bridging properties. Post weld heat treatment improved the mechanical and microstructural properties of AA6061. A 3D mathematical model is proposed by Lu *et al*. [2014] to investigate the heat flow during GMAW. The proposed model has considered the momentum, energy flow and mass transfer of molten metal produced among interaction of plasma arc, filler wire and workpiece. The proposed model can be employed to obtain higher quality welds and dimensional accuracy with high energy efficiency.

The behaviour of molten droplet deposition on solid workpiece is affected by various mechanisms that include mass transfer, gravity effect, wetting and capillary forces. A unique experimental technique [Chapuis *et al*., 2013] is used to measure the bead geometry of a macro drop of molten metal developed during P-GMAW based deposition. Mass and heat transfers are responsible for gradual spreading whereas kinetic energy and direct arc heating on the workpiece results in initial rapid spreading of the macro-drop. In order to understand the metal transfer behaviour to predict the metal droplet size during alternating current GMAW. A mathematical model [Arif & Chung, 2014] is introduced to predict the metal droplet size to fill the varying gap between the thin worksheets. The developed model can be successfully employed with direct current GMAW and pulsed-GMAW. GMAW) and pulse GMAW (P-GMAW) processes are used to join modified medium manganese steel. P-GMAW has shown superior plastic deformation capacity over GMAW. Pulse current provides treatment to reduce the grain growth in weld which results in finer grain structure consequently ductility of the weld joint improved [Di *et al*., 2015].

The relationship between properties and microstructure is rarely analyzed in parts fabricated by AM. GMAW based 3D metal printing [Haselhuhn *et al*., 2016] is employed for deposition using different aluminium alloys to identify the suitable alloy system for

AM. Less than 2% porosity is observed in all test specimens. Sufficient time for cooling resulting in annealing and stress relieving consequently improved the mechanical properties. Optimum rate of cooling is crucial for specific microstructure which defines grain size and consequently desired mechanical properties. A unique technique is used to analyze the influence of additional cooling gas supply on hardness and microstructure during metal printing through AM. Uniform microstructure can be achieved by modelling the grain structure and size through composition of shielding gas [Henckell *et al*., 2017].

In welding, bead quality largely depends upon the process parameters. Welding speed and magnetic field due to excitation of current can produce backward flowing metal which leads to formation of humping beads during high speed GMAW. It is observed that magnetic field can significantly reduce the velocity of backward flowing metal consequently humping beads disappear [Wang *et al*., 2016]. A 3D reconstruction technique [Wang *et al*., 2019] is applied to analyze the effect of different process variables on flow of molten metal in the welding zone during high speed GMAW. In this technique the trajectory and velocity of tracer particles are measured and analyzed at different locations subsequently revealing the occurrence of humping bead defects. It is reported that fluid flow velocity significantly affects the bead geometry.

Polylactic acid composites are fabricated by incorporating natural fiber as reinforced material by hot compression using a film stacking process. The developed composite can be replaced with traditional synthetic fiber composites in various application areas owing to superior mechanical properties. Polylactic acid exhibited the best performance in terms of tensile, compressive and flexural strength. The improved tensile, compressive and flexural properties of the developed composites explained that the overall load carrying capability have significantly enhanced [Bajpai *et al*., 2012]. A friction stir processing technique is employed to fabricate hybrid aluminium composites by incorporating TiB_2 and BN particles into aluminium alloy AA6082. SEM images clearly indicate the uniformity in dispersion of TiB_2 and BN particles in the aluminium matrix with. No segregation is observed of TiB_2 and BN particles in hybrid aluminium composites. The inclusion of BN particles improved the wear resistance of developed composites by acting as a dry lubricant and forming a tribo boundary film [Palanivel *et*

al., 2016]. An acrylonitrile butadiene styrene tool is used to machine expandable polystyrene. Taguchi factorial design method is used to design experiments. Various process variables such as spindle speed, depth of cut and feed rate are varied to investigate their effects on surface finish and dimensional accuracy of the grooves machined by 3D printed thermoplastic. It is observed from the experimental results that the surface finish and dimensional accuracy are affected by spindle speed and depth of cut respectively [Sandhu *et al*., 2020].

2.7 Dissimilar Metals Joining

Joining of dissimilar metals is essential in order to meet the specific requirement of various industries including aerospace, chemical, nuclear and electronics industries for new structure development. Joining of dissimilar materials requires close look into the microstructural behaviour of metals to be joined owing to the differences in physical, chemical, mechanical and thermal properties. The work done on aforesaid topic by various researchers is reported in the preceding section.

Dissimilar stainless steels i.e., austenitic and duplex stainless steels are welded to investigate the effect of double layer shielding gas using GMAW. A simple modification is done on the existing welding setup to supply additional shielding gas. Double layer of shielding gas that is primary shielding gas along with additional supply of shielding gas improved the tensile strength and micro hardness [Kumar *et al*., 2015]. Furthermore, a simple modification in welding torch arrangement to supply CO_2 as secondary shielding gas along with suitable process parameters may affect the microstructure of fusion and interface and consequently change in mechanical properties during dissimilar steels joining [Bhattacharya & Kumar, 2016]. Austenitic stainless steel and alloy steel are welded using tungsten inert gas (TIG) welding to investigate the effects of various process parameters on mechanical properties. Furthermore, heat transfer efficiency can be improved by adding a small proportion of hydrogen gas in shielding gas which in turn enhances the melting and subsequently penetration depth [Bhattacharya & Singla, 2017].

GMAW-GTAW double side arc welding and brazing technique [Zhang *et al*., 2016] is employed to weld dissimilar metals i.e., aluminium alloy and stainless steel

using different process parameters. Joint strength is measured by conducting tensile tests. Results confirmed that good quality sound joints are produced by welding and brazing owing to less heat input as compared to conventional welding process. Titanium alloy and stainless steel are welded using two different filler wires to investigate the mechanical properties and microstructural properties during GMAW-GTAW double side arc brazing. The welding of Titanium alloy and stainless steel is successfully carried out and produces defect free joints [Liu *et al*., 2019].

GMAW welding of dissimilar stainless steels i.e., AISI 409 and AISI 316L is performed to investigate the influence of different process parameters on various mechanical properties. Taguchi factorial design of experiment (DOE) technique can be used to design experiments. It is reported that improper inclination of welding torch and fast travelling speed result in uneven penetration [Ghosh *et al*., 2017]. A coated electrode is designed and extruded on 309L filler to weld 2507 duplex stainless steel and API X70 alloy steel using shielded metal arc welding. The mechanical and microstructural properties of the welded specimens are investigated to compare the performance of developed electrodes with commercial one. Experimental results revealed that the developed electrode has exhibited high tensile strength and toughness in comparison to commercial electrodes [Khan & Chhibber, 2021]. The influence of arc offset during joining of dissimilar metals (AISI 304 stainless steel and copper) using the GTAW process. Owing to huge difference of material properties, uneven distribution of the heat at the weld interface and consequently arc offsetting towards copper plate is observed. A finite element model is developed to analyze the thermal behaviour due to offset of arc during welding [Singh *et al*., 2021]. Finite element analysis reveals that AISI 304 stainless steel melts even at a lower value of arc offsetting in comparison to copper.

Multi material design is the necessity of advanced automotive industries due to few specific reasons such as fuel efficiency and reduction in eco-unfriendly gas emission. Furthermore, joining of dissimilar metals is challenging due to differences in mechanical and thermal properties. GMAW based Cold metal transfer (CMT) based brazing technique [Singh *et al*., 2019] is implemented to weld aluminium and steel to examine the influence of process variables on mechanical properties. Low heat input induced during

CMT hinders the formation of intermetallic compounds at boundaries. GMAW based CMT is also employed to fabricate dissimilar weld between aluminium and mild steel. Interface of weld bead and mild steel is degraded with the presence of Al-Fe-Si intermetallic compound (IMC) layer. It is reported that IMC layer thickness is maximum at the toe region of weld bead and mild steel interface. Immense zinc accumulation is observed at the toe region [Sravanthi *et al*., 2019]. Dissimilar joining of aluminium and steel has tremendous applications in automotive, aerospace and shipbuilding industries owing to light weight which leads to high efficiency. Due to the high difference in melting point of two metals, it is not easy to join aluminium and steel and needs extra attention while joining. An experimental study is conducted to investigate the weldability behaviour of aluminium alloy and stainless steel during GMAW. Experimental result reveals that high hardness is achieved due to the presence of silicon traces and whereas chromium carbide is responsible for highly brittle intermediate compounds [Sachin *et al*., 2020].

A mathematical model is proposed by Huang *et al*. [2017] to study the effect of alternation of the droplet transfer for joining the aluminium alloy and mild steel using double electrode pulsed GMAW. Bonding mechanism and microstructural characterization are analyzed to investigate the effect of process parameters. The friction stir welding is performed between dissimilar metals i.e., stainless steel and mild steel. The tool (tungsten carbide) offset and rotational speed are analyzed on mechanical properties i.e.,, tensile strength, toughness and microhardness of dissimilar welded joints. Different transition zones such as sharp and gradual are observed in various regions of the stir zone of the weld joint [Tiwari *et al*., 2019].

2.8 Effects of Activated Fluxes in Welding

Enhancement in the weld penetration is always a matter of discussion while joining thick sections in a single pass. Although the welding parameters namely welding current, speed, torch inclination have significant influence on the depth of penetration, these parameters cannot go beyond a certain limit as it could lead to unwanted welding defects and consequently failure of weld. Activating flux is a suitable alternative to deal with such kinds of issues used by many researchers presented in the preceding section.

The influence of shielding gas composition and activated flux is investigated on bead geometry, distortion, hot cracking and mechanical properties of stainless steels during activated gas tungsten arc welding (A-GTAW). The results revealed that cross-sectional area of deposited bead and depth of penetration enhanced with the addition of nitrogen in argon supplied as shielding gas. The addition of nitrogen in shielding gas also reduced the weld distortion but increased the hardness and tensile strength [Huang, 2009]. Various welding process parameters along with three different types of activated fluxes such as SiO_2, Fe_2O_3, and $MgCO_3$ [Huang, 2010] are used to influence the bead geometry, specifically depth of penetration during joining of carbon steel using GMAW. It is reported that there is a direct relationship between the arc profile and depth of penetration which can be analyzed from recorded images of charge coupled device systems. Twin wire MIG is performed to weld aluminium alloy with SiO_2 activated flux applied prior to welding. About 26% deeper penetration is achieved with the use of SiO_2 flux. The constricted arc and huge arc temperature are main factors affecting the penetration depth during twin wire MIG [Ruan *et al*., 2012].

The effect of various activated fluxes i.e., KCl, TiO_2 and $CaCl_2$ is analyzed on the spatter loss and metal transfer behaviour during joining of magnesium alloy by MIG welding. The results revealed that KCl activated flux has mitigated the spatter loss and produces smooth metal transfer. Furthermore, the metal transfer on KCl activated flux is enhanced by electromagnetic force which is further related to increase of welding current [Zhang *et al*., 2012]. The effect of TiO_3 activated flux is studied by Tathgir *et al*. [2015] to analyze the depth of penetration during joining of dissimilar metals by varying welding current and shielding gas at different levels during tungsten inert gas (TIG) welding. The results showed enhancement of depth of penetration with the use of TiO_3 activated flux. The constricted arc enhanced the energy density and resulted in deeper penetration. Influence of oxide fluxes TiO_2, Fe_2O_3, MnO_2, CrO_3, CaO and ZnO on bead profile deposited by A-TIG on P91 (9Cr–1Mo) modified steel. Optimized process variables are used to obtain desired penetration depth with adequate heat input. Bead width and penetration depth variation can be determined as a function of welding current at constant travelling speed. It is reported that full penetration depth is achieved with the application of these oxide fluxes [Dhandha & Badheka, 2015].

In order to increase the penetration depth, use of activated fluxes is a suitable option for thick plates with a smaller number of passes. Effect of different activating fluxes and compositions of shielding gas are analyzed to observe the arc behaviour and depth of penetration during A-TIG joining of dissimilar grades of low alloy steel, stainless steel AISI 304/316 & duplex steel [Tathgir & Bhattacharya, 2016]. Eight different activating fluxes having different oxygen contents are applied before welding to investigate the weld bead geometry using GMAW joining of structural carbon steel by Varbai *et al*. [2017] and reported that SiO_2 and MnO fluxes have relatively greater effects on depth of penetration. Furthermore, oxygen content has direct proportion to the bead width whereas inverse proportion to the bead height. The influence of different oxide activating fluxes was investigated by Vora & Badheka [2017] on reduced activation ferritic / martensitic (RAFM) steels to examine the weld bead geometry during activated TIG. The results revealed that the fluxes Co_3O_4 and MoO_3 produced full depth of penetration. Stainless steel is welded by GMAW process using two kinds of activated fluxes SiO_2, Cr_2O_3 for varying the bead profile. Apart from this the process parameters such as welding current, voltage, travelling speed and torch angle have significant effect on penetration depth. From the experimental results it is reported that constricted arc and centripetal Marangoni convection has enhanced the penetration depth of joints [Chaudhari *et al*., 2018].

2.9 Bond Graph Modelling

This section addresses the literature review on the application of bond graph modelling for simulation of various systems such as fault diagnosis problems, development of a thermal model and other different mechanisms. In the present work, system modelling of the fabricated setup is carried out using bond graph (BG) technique to predict different system behaviours as well as to predict the weld bead geometric path. Different components such as power source, stepper motor, controller, mechanical parts lying in different energy domains were modelled using BG technique. The BG models along with system responses in single direction as well as in two directions are presented.

An automatic setup for GMAW with automatic movement of the welding torch is developed to investigate the effect of different welding variables on bead geometry.

System behaviours are studied using bond graph modelling technique. Apart from this, BG modelling technique is also used to predict welding time and speed subsequently used for bead deposition. The welding results revealed higher deposition efficiency, low spatters and uniform penetration depth [Bhattacharya & Bera, 2014]. Unidirectional automatic movement setup for GMAW was proposed by Bhattacharya *et al.* [2014] for bead deposition. Fusion zone profile and penetration depth are predicted using bond graph modelling technique and validated by measuring the fusion profile and deposited bead subsequently. The results revealed that high gas flow rate as well as cooling rate of weld pool significantly influences the toughness as high gas flow rate increases the solidification rate which results in fine grain structure and consequently, high toughness of joint is observed. A semi-automatic GMAW setup for planar welding profile is developed by Kumar *et al.* [2019] to decide the effect of process parameters on geometrical shape of weld. Bond graph modelling technique is used to predict the different system behaviours. Furthermore, weld bead profile is also predicted using BG modelling technique. It was observed that deposited beads had reasonable uniformity along the path for welding. Predicted bead profile is validated with deposited beads. A two directional automatic setup is used to deposit any desired profile using GMAW. Whole setup including the mechanical, electrical or electronic control unit is modelled using a bond graph modelling approach. This technique can provide system responses without prior trial before experimentation. The performance of the setup is validated for deposition of various open and closed profiles [Kumar & Bera, 2020].

Bond graph modelling approach can be implemented as fault diagnosis problems of any arbitrary system. Interval analytical redundancy relations methodology is used to prevent missed alarms, false alarms and robustness issues. A dedicated sliding mode differentiator is used to improve the accuracy of the measurements derivatives estimation in the proposed methodology. For the successful detection of fault measurements, the Fourier-Motzkin Elimination (FME) technique is integrated within the I-ARRs [Jha *et al.*, 2017]. Most of the existing fault detections and diagnosis applications are based on massive data driven. Due to massive data handling the system becomes complex. To resolve this issue bond graph modelling technique is proposed as it is a multidiscipline energetic approach therefore it can be used to achieve a graphical nonlinear model of the

Tennessee Eastman Process (TEP) for simulation as well as monitoring tasks by generating fault indicators [Tidriri *et al*., 2017]. Bond graph based 3D model is presented for modelling and obstacle avoidance of a biped robot. Subsequently a hybrid obstacle avoidance algorithm is developed by using the merits of the line following, tangent bug and wall following algorithm. The practicability of the algorithm is validated in two cases depending upon the positions of the obstacle. Eventually, the validation of the simulation and experimentation work is considered successfully [Singh & Bera, 2019].

Bond graph approach is used to develop a thermal model for the twin tube hydraulic shock absorber. Force and temperature are measured at the rear shock absorber of a commercial passenger sedan. Simulation results are compared with experimental results and validated successfully. Results revealed that the volume flow rate of hydraulic fluid is less in the lower chamber than that in the upper chamber [Singh & Bera, 2016]. A four-bar mechanism driven knee exoskeleton (KE) is used to compare which is capable of accommodating both the rotary and the linear actuators. Bond graph (BG) technique is used to perform the modelling and simulation of the performance comparisons of a four-bar mechanism-driven KE. The results successfully revealed that both actuators offered desired ranges of motions required for STS motion [Jain *et al*., 2020].

2.10 Observations from Literature

After doing detailed review of above-mentioned literature on different aspects such as 3D metal printing techniques, influence of process parameters, joining of dissimilar metals and application of activated fluxes, the observations from the relevant literature are as follows:

- It has been found that the layer deposition in GMAW is a new concept.
- It has also been observed that an alternatively a low-cost planar welding setup may be designed and fabricated.
- Very few literatures are available on activated flux in GMAW.

2.11 Objectives of the Present Work

It is concluded from literature review that most of researchers have reported joining of dissimilar metals in the presence of activated fluxes during TIG. Therefore it is required to be work done on activated fluxes for dissimilar metal joining using GMAW. Based on the above discussion, the following objectives have been derived for the present work:

1. To design and fabricate planar (bi-directional) movement setup for GMAW.
2. To model the developed planar (bi-directional) movement setup for the system response.
3. To perform planar welding for a given trajectory and profile.
4. To observe the effects of activated flux on GMAW.
5. To implement bi-directional GMAW for metallic layer deposition.
6. To investigate the effect of process parameters (welding current, voltage, travelling speed, gas flow rate) on welding bead geometry (bead width, bead height, penetration), arc stability and voltage-current characteristics.
7. To study the effect of welding process parameters on micro-structural and mechanical properties of dissimilar steels joining.

Chapter 3

Fabrication and Modelling of GMAW Setup

A bi-directional automatic movement setup for welding was indigenously designed and developed in order to obtain weld with uniform bead width along a desired path at significantly lower cost. The fabricated gas metal arc welding (GMAW) setup was used to deposit different open and closed profiles in single bead layer deposition, single bead multi layers depositions and multi beads multi layers deposition with positive and negative slopes to measure the capabilities/effectiveness of the automatic movement setup. The computer-aided design (CAD) model and a prototype, block diagram of the complete setup and connection between controller, drivers and stepper motors are presented in this chapter. System modelling of the fabricated setup was also carried out using bond graph (BG) technique to predict different system behaviours as well as to predict the weld bead geometric path.

Before proceeding towards the detailed discussion about the fabrication of a bi-directional automatic movement setup it is important to mention here that the weld beads were deposited manually as well as with fabricated unidirectional GMAW setup (Bhattacharya and Bera, 2014) during initial development stage of the present setup. The same setup is upgraded for the bi-directional metal deposition in the present work. A substantial difference was observed between two beads deposited differently. Hand stability during manual bead deposition played significant role which, of course was observed absent and to over cum this issue, a uni-directional automatic setup was developed and used which provided constant contact tube to work distance consequently uniform heat input, penetration depth and bead width. As the uniformity and accuracy of the welds produced with the earlier developed setup with the conventionally available GMAW machine were checked, therefore no more comparison was done for the present setup.

3.1 Computer-Aided Design (CAD) Model and a Prototype

A computer-aided design (CAD) model and a wooden prototype of bi-directional movement setup for planar welding was first made for conceptualization and then the setup is fabricated. The CAD model of the setup was made using Creo designing software. The CAD model and the conceptual prototype of the bi-directional movement setup for planar welding are shown in Fig. 3.1(a) and 3.1(b), respectively.

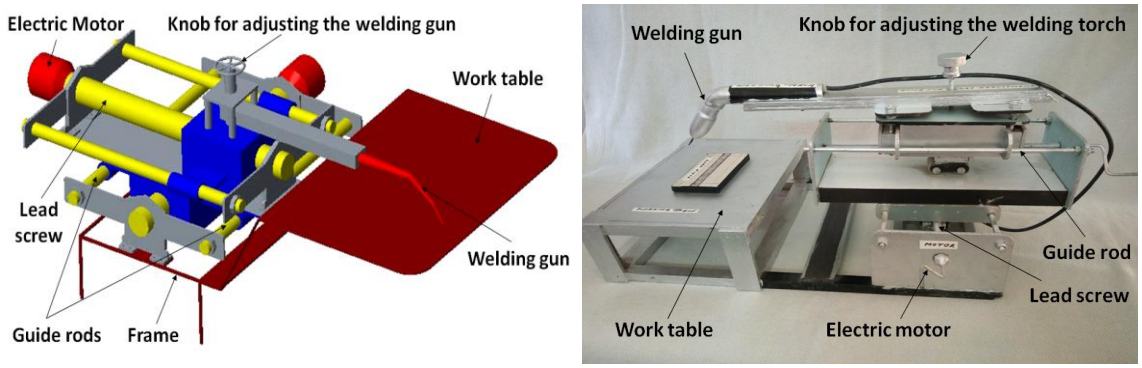

(a) (b)

Figure 3.1 Planar movement setup for GMAW: (a) CAD model and (b) a wooden prototype

3.2 Fabrication of GMAW Setup

Initially, the automatic planar movement setup for GMAW was operated with two direct current (DC) motors at two different speeds only and subsequently, realizing the necessity of improving/upgrading the accuracy of the fabricated setup to deposit intricate profiles, DC motors were replaced with two stepper motors having 200 steps per revolution. The detailed discussion about the setup is provided in the following paragraphs.

During the initial stage, the automatic planar movement setup consisted of four key elements i.e., DC motors, transmission system, carriage and the guide ways as depicted in Fig. 3.2(a). Two separate and independently controlled actuators were used for controlling the planar movement of welding torch along x and y axes. Separate regulators for independent control of motions along two different axes i.e., x and y axes were provided. Both the DC motors have power ratings of 0.5 kW, torque of 50 N-m and angular speeds of 36 and 50 rpm. A gear having 44 teeth was mounted on the output shaft of each drive motor and meshed with the pinion having 25 teeth. The positions of gear

and pinion were altered to increase the welding speed. The shaft on which the pinion is mounted is attached with the lead screw (pitch 2.4 mm) and the nut of the lead screw is attached with the carriage for the movement along *x* or *y*-direction. The maximum traveling distance along lead screw was 550 mm in each direction. Thus, the total work envelope available for welding is 550 mm × 550 mm. The arrangement for holding the welding gun and the attachment for vertical height adjustment of welding torch were fabricated on the *y*-directional carriage. The attachment for the height adjustment of the welding torch along vertical direction can be used to set the nozzle tip-to-workpiece distance based on the thickness of the workpiece to be welded.

After subsequent modification of the weld setup, the main components of the automatic movement setup for GMAW are stepper motors, lead screws, couplings for connecting motor shafts with the lead screws, carriages, guide rods for smooth movement of the carriages, welding torch, work table and knob for adjusting the height of the welding torch as shown in Fig. 3.2(b). Figure 3.2(c) shows the complete automatic GMAW setup with welding arrangements i.e., setup with weld table, serial monitor for the input of the desired welding path. The motor attached with the lower lead screw has more torque rating (1.85 N-m) than the motor (1.28 N-m) connected with the upper lead screw as former has not only to move the corresponding lead screw but also to move the carriage along with other set of motor-lead screw arrangement. The specifications of the bigger motor are input-voltage of 3.2 V, current of 2.8 A per phase, inductance of 3.6 mH, armature resistance of 1.3 Ω per phase and 200 steps per revolution. The specifications of the smaller motor are input-voltage of 2.5 V, current of 2.8 A per phase, inductance of 2.5 mH, armature resistance of 0.9 Ω per phase and 200 steps per revolution. The welding torch (Torando MIG350) is connected with the upper carriage of the setup.

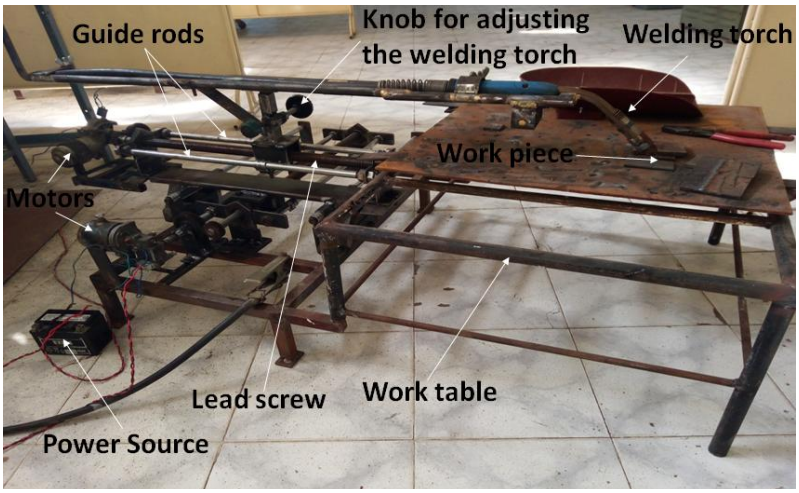

(a)

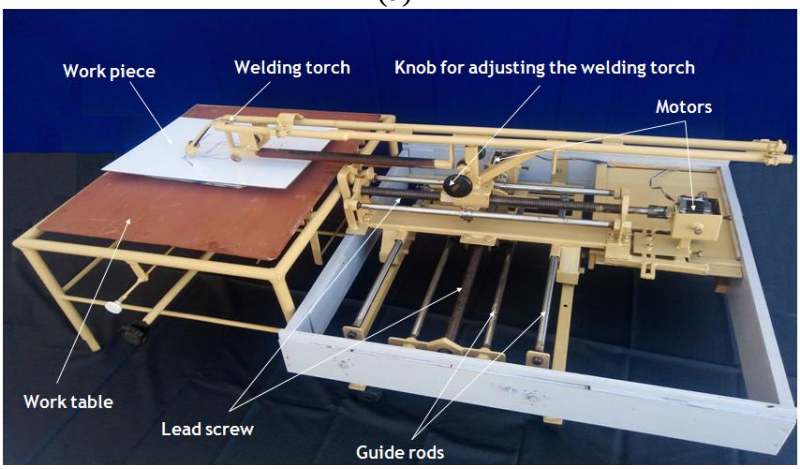

(b)

(c)

Figure 3.2 Automated welding machine: (a) fabricated setup at initial stage, (b) fabricated setup after modifications and (c) complete fabricated setup with welding arrangement

3.2.1 Block Diagram of the Setup

Figure 3.3 showed the block diagram of the present setup. A dedicated electronic control unit was developed to independently control both the stepper motors along two different axes for the desired positions of the welding torch during deposition of metal. Initially, the given trajectory was fed through the serial monitor in terms of G-code programming. The controller Arduino UNO sent signals to the motor drivers (DM542) which received power through switched mode power supply (SMPS). A 220 V AC power supply was given to the SMPS and output from it was the voltage of 24 V and current of 4.5 A. Since the Arduino operated at 4.5 V, it could not directly control the actuator (stepper motor) which ran on higher voltage. Therefore, motor driver was used and the Arduino controlled the driver. The stepper motor drove the lead screw mounted on the setup which further enabled to perform the desired motion.

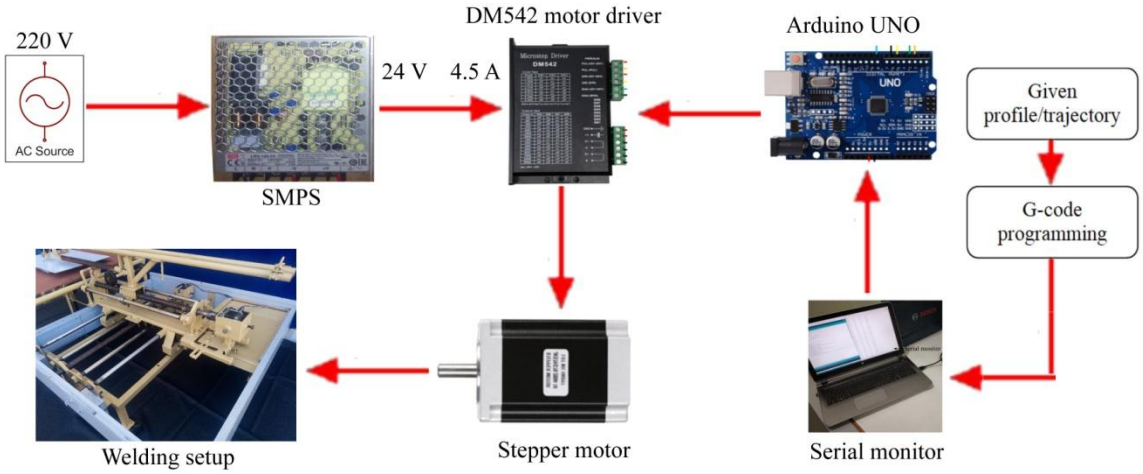

Figure 3.3 Block diagram of the setup

3.2.2 Connectivity between Controller, Driver and Motor

The interfacing and connectivity of the drivers (DM542) and stepper motors with the microcontroller were depicted in Fig. 3.4. Terminal 1 and 2 of the drivers were connected with the 24 V, 4.5 A DC power supply from the SMPS and the ground, respectively. Bipolar drives which generated greater torque were designed for bipolar motors with four leads. The driver alternately reversed the current in each phase to drive the rotor. The

terminals 3–6 of the drivers were connected with the two phases of the motors. The pulse, direction and enable terminals were connected with the corresponding ports of Arduino UNO.

3.3 Bond Graph Modelling of Bi-Directional Movement Setup of GMAW

The modelling of bi-directional movement setup for GMAW was done using BG technique. The BG is a system modelling approach based on conservation of power. This technique is useful even if the components of the system lie in different energy domains. Only the kinematic equations are required for modelling of any system using BG and the dynamic equations are automatically developed from the model. The BG modelling technique is very much algorithmic depending on the assignment of causality (relationship between cause and effect) in it. The modelling of this planar setup is essential to understand and analyze the system responses for different inputs to the system. As an example, for a particular value of voltage fed to the system, the current and torque developed by the DC motor or the speed of welding (speed of welding torch) can be assessed for this particular value of the voltage. The BG modelling technique which is bi-directional for flow of signal has been used here as it is unique or compact in nature i.e., only seven elements (Inertial element (I), Compliance element (C), Resistive element (R), Transformer (TF), Gyrator (GY), Source of effort (Se), and Source of flow (Sf)) and two junctions (1 and 0-junction) are required to model systems residing in different energy domains (e.g., electrical, mechanical, chemical, thermal, hydraulic, financial system etc.). Three elements i.e., I, C, and R are generally single port (i.e., single bond connects these elements) passive elements (i.e., no power is generated), but TF and GY are the two-port scaling elements. Two signals move along the bond (as BG is bi-directional) which is represented by a line with a half arrow. The causal stroke (small perpendicular line on the bond) indicates the direction of effort signal and flow signal moves in the opposite direction along the bond. The causality of the storage elements (I and C element) is fixed. The junction elements (1 and 0-junctions) and converters (TF and GY elements) have constraints in causality. Only the causality of the free causal element (R element) is determined depending on the causality of other elements and junction laws. Algorithm can easily be established by assigning causalities to the BG elements and the system responses can be quickly obtained. The bond with full arrow is

called the information bond and this type of bond is used to represent sensor in the system and this sensor provides output/response. 1-junction is required to indicate equality of flow variables i.e., current, linear velocity, or angular velocity. Similarly, 0-junction is used to denote equality of effort variables i.e., voltage, force, or torque. Another advantage of BG modelling is that no dynamic equation is required for modelling of any system and system equations can be derived from the model based on junction laws. Here, BG technique has been adopted as the motor and rest of the system remain in electrical and mechanical domain, respectively and it is very easy to model using BG for this type of multi-domain system. No system equation was used to model this system and only the knowledge of cause-effect relationships (causality) of different components of the system i.e., physics behind the input and output of each sub-system is required for modelling through BG technique.

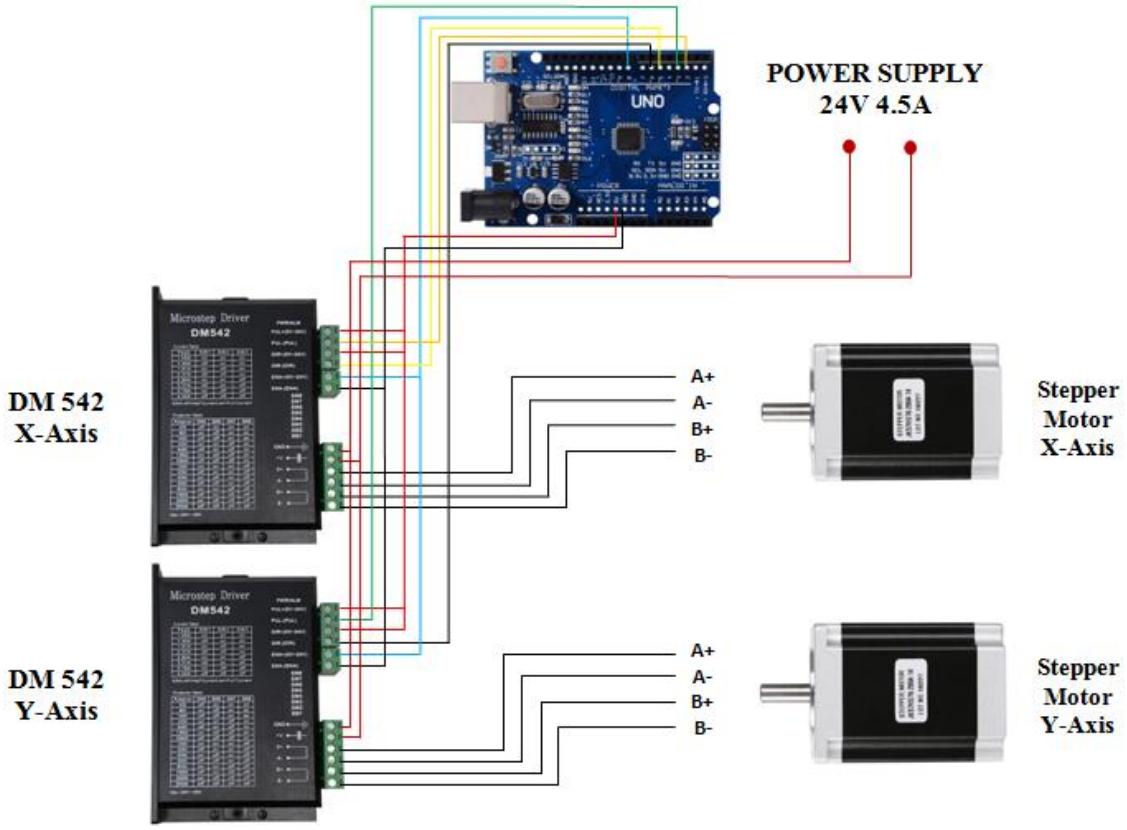

Figure 3.4 Connectivity between controller, drivers and motors

Bond graph modelling technique has been adopted here for modelling of the welding setup. Bond graph modelling has been considered here as the different components (controller, power source, stepper motor, mechanical part) lie in different energy domains. This modelling tool is better than other methods as it does not require dynamic equations of the system and it only needs kinematic equations. The dynamic equations can be generated easily based on the number of state variables present in the system. A simplistic bond graph model has been developed assuming that the voltage input to the stepper motor is a function of the weld bead profile to be generated by the planar welding setup. The heat generated in two bearings in both sides of the lead screw is not considered in the model. The values of the torsional stiffness and the stiffness of the guides are assumed as linear stiffness. The word bond graph of the welding setup is shown in Fig. 3.5. This diagram relates the energy interactions between different parts of the system. The controller compels the power source to provide exact amounts of voltages to the motors. The motor provides torque to the lead screw through coupling capacitor (torsional stiffness of the lead screw). The lead screw provides linear motion to the welding torch. Two separate sets of components are used for motions along *x* and *y* directions.

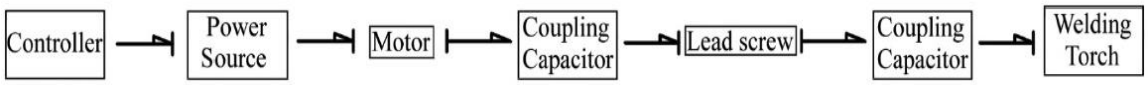

Figure 3.5 Word bond graph of the setup

3.3.1 Bond Graph Modelling in Single Direction

The bond graph model of the complete setup along *x*-directional movement is shown in Fig. 3.6. A similar model is also developed for the *y*-directional movement. The bi-directional movement setup for GMAW consists of two direct current (DC) motors, two pairs of gears, two lead screws, guides, welding torch etc. Two DC motors are required for independent movement of welding torch along *x* and *y* directions on horizontal plane (plane of workpiece). The voltage (*v*) supplied to the DC motor is represented by the source of effort (Se) element connected at 1-junction. The armature inductance (L_a) and

armature resistance (R_a) are represented by inertial element (I) and resistive element (R), respectively and those are connected at the same 1-junction as the current is same (due to series circuit) for all the elements of the input electric circuit of the DC motor. The current (i) in the armature circuit is sensed by the current sensor which is represented by Df (flow detector). The torque (τ) developed by the motor is represented by the modulated source of effort (MSe) and this torque is given by $k_m i$ where k_m is the motor constant (in N/m). This MSe element is connected to the 1-junction which denotes the angular velocity ($\dot{\theta}_m$) of the output shaft of the motor. The back electromotive force (emf) of the motor is represented by the modulated source of effort (MSe) element and this back emf is given by $k_b \dot{\theta}_m$ where k_b is the back emf constant (in V-s/rad). The mass moment of inertia (J_f) of flywheel and viscous damping (R_v) are represented by inertial element (I) and resistive element (R), respectively and those are connected at the same 1-junction as the angular speed is same for all the elements connected to the 1-junction. The gear ratio G is represented by the transformer element (TF) which converts one flow signal (here, angular velocity) to other flow signal in the arrow direction of the bond or one effort signal (here, torque) to the other effort signal in the opposite direction of the bond. The damping of two bearings is represented by R_{b1} and R_{b2}. The torsional stiffness (K_t) of the shaft is denoted by the compliance element (C) which is a potential energy storing element. The inertia element (I) represents the mass moment of inertia of the lead screw. The transformer element (TF) with modulus $\frac{L}{2\pi}$ is used to convert rotary motion of the lead screw to the linear motion ($\dot{x}_1$) of the nut where L is the lead of the lead screw. For the smooth running of the carriage with nut over the lead screw, two guides which are kept parallel to the lead screw are used and the damping (R_g) due to two guides is represented by R element. K_f represents the linear stiffness or reciprocal of flexibility of the lead screw. The mass (M_s) of the support along with welding torch is denoted by the I-element connected at $1_{\dot{x}_2}$ junction. The velocity as well as displacement of the welding torch can be found out using the velocity sensor (flow detector or Df) connected at the same 1-junction. The similar bond graph model can be framed for the movement (y_2) of the welding torch along y-direction. If the two motors run simultaneously, the welding torch will move along a line with a slope ($\tan\theta$) of $\frac{y_2}{x_2}$ when the weld path makes an

angle of θ measured from the x-axis. The integrator block provides the integral (linear or angular displacement, here) of its input (linear or angular velocity, here) at the current time step. The purpose of sink is to display or to export data.

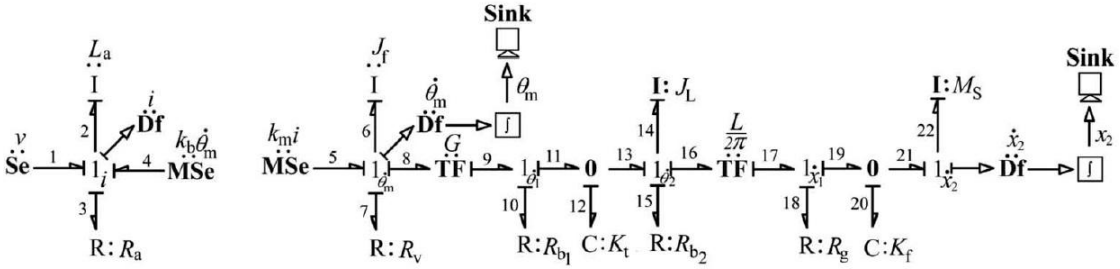

Figure 3.6 Bond graph model of the setup for x-directional movement

3.3.2 Bond Graph Modelling in Two Directions

Figure 3.7 indicates the bond graph model of the welding unit. Se-element indicates the voltage provided to the DC stepper motor. The voltages v_x and v_y are decided by the controller. In this case, the voltages are modulated depending on the profile to be traversed by the welding torch. The bonds 1–4 denote the electrical parts of the motor and the bonds 5–8 denote the mechanical parts of it. The voltage fed to the motor is received by the inductance (I-element) and it returns current to the system. This current is converted to the torque (current × motor constant) developed by the motor and in the backward direction, back emf (angular velocity × back emf constant) is developed. R_a and R_v are the resistance of the armature circuit and viscous damping, respectively. J_f and J_L are the mass moment of inertia of the rotary part of the motor and the lead screw, respectively. R_t is the torsional stiffness of the lead screw. The transformer element (TF) having modulus of $\frac{L}{2\pi}$ converts the rotational speed ($\dot{\theta}$) of the screw to the linear speed of the nut mounted on it. R_x, K_f and M_s are linear damping, stiffness and the mass of the welding torch along with the holding device. In controller, Sf indicates the rotational speed of welding. The transformer with modulus μ_x or μ_y is used to convert rotational speed to the linear speed. The voltage fed to the motor is directly proportional to the angular speed indicated by the element Sf.

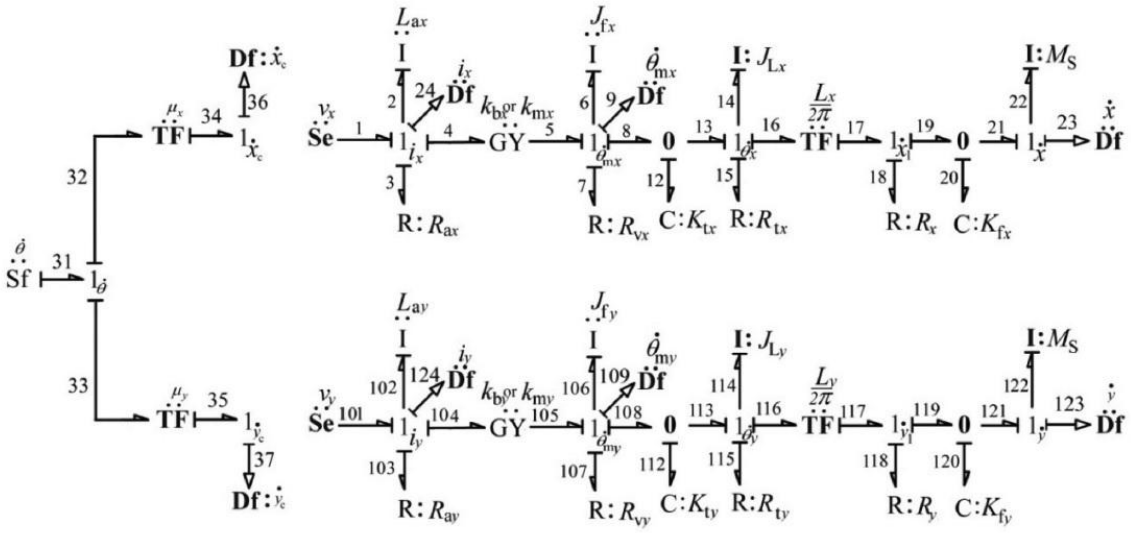

Figure 3.7 Bond graph model of the setup in two directions

For a particular displacement or speed of welding torch during its movement along a profile, the torque developed by the motor or the voltage fed to the motor can be determined by bond graph modelling of the setup.

3.4 System Response

The system response of the model of the bi-directional movement setup for GMAW was appraised before performing experimentation.

3.4.1 Bond Graph Response in Uni-Direction Motion

The automatic movement setup for GMAW was used for welding at two different values of weld speeds (S_w) i.e., 2.5 mm/s (hereafter, mentioning as slow speed) and 3.5 mm/s (mentioning as fast speed). For these two speeds, the armature resistances of the DC motor (Lucas TVS Limited, Chennai, India) are assigned as 3 Ω and 4.13 Ω, respectively. All the parameters (input voltage, input current, torque, angular speed) of DC motor are taken from the product data sheet. The other parameter values used for simulation are given in Table 3.1. The parameters related to gear and lead screws are taken from the supplier's catalogue. Most of the parameter values were taken from the experimental setup but few parameters were decided by comparing system responses of simulation with experimental results. The stiffness and viscous damping parameters are adjusted in

the simulation by comparing the travelling speed of the welding torch during experimentation. The mass of the guide and welding gun of the setup is directly measured. The parameter value of motor constant is obtained from simulation by trial to match the input current and torque developed by the motor. Similarly, the parameter value of motor back emf constant is obtained from simulation by trial to match the input current and angular velocity of the motor.

The current in the armature circuit and torque developed by the DC motors during low speed (2.5 mm/s) and high speed (3.5 mm/s) are shown in Fig. 3.8(a). The currents in the input circuit of the motors are 3 A and 4.17 A (output of current sensor Df at 1_i junction in BG model) for the low and high speed, respectively. Similarly, the torques developed by the motors (output of MSe element at bond number 5 in BG model) during low and high speeds are 50.01 N-m and 69.59 N-m, respectively. The current and torque plots become steady within very short duration of starting of the motors. The variations of angular speed of motor and linear speed of the welding torch with time are shown in Fig. 3.8(b). The angular speeds of the motors are 3.77 rad/s and 5.24 rad/s (output of angular velocity sensor Df at 1_{ω_m} junction in BG model) when it reaches to a steady state. Similarly, the linear travel speeds of the welding torch at steady state during low and high speeds of the motors are 2.53 mm/s and 3.52 mm/s, respectively (output of velocity sensor Df at 1_{v_2} junction in BG model). If the two motors run at the same speed, the welding torch should move theoretically with an angle of 45° with the *x*-axis and from the simulation, it is predicted as 45.02° as shown in Fig. 3.8(c). With the simultaneous rotation of two motors at 5.24 rad/s and 3.77 rad/s, respectively for *y* and *x*-directions, the weld path at an angle of 53.8° is predicted by simulation in comparison to the experimental value of 56.22° with the *x*-axis. Similarly, when the two motors rotate simultaneously along *y* and *x*-directions at a speed of 3.77 rad/s and 5.24 rad/s respectively, the welding torch movement at an angle 36.1° is predicted in comparison to the theoretical value of angle 36.2° with the *x*-axis (refer Fig. 3.8(c)). Simulation was also performed to analyze the change of linear acceleration of the welding torch when the speed of the motor either increases or decreases from the initial speed. With increase in motor speed from 3.77 rad/s to 5.24 rad/s at any instant (as an example at 3s, refer Fig.

3.8(d)), the acceleration of the welding torch changes to 3.02 mm/s^2 (output of rate of change of momentum over mass at bond number 22 in BG model). Similarly, when the speed of the motor decreased from 5.24 rad/s to 3.77 rad/s, the deceleration of the welding torch changed to 3.52 mm/s^2 shown in Fig. 3.8(d). It may be noted from Fig. 3.8(d) that once the speed is changed, the responses after the disturbance become steady within a very short duration.

Table 3.1 Parameter values used for modelling in uni-directional motion

Parameters	Values	Parameters	Values
Voltage (v)	12 V	Damping in bearing1 (R_{b_1})	0.5 N-s/m
Inductance (L_a)	0.5 H	Torsional stiffness of shaft (k_t)	10^3 N/m
Resistance (R_a)	3 Ω, 4.125 Ω	Damping in bearing2 (R_{b_2})	0.5 N-s/m
Motor constant (k_m)	16.67 N-m/A	Moment of inertia of lead screw(J_L)	0.0012 kg-m^2
Back emf constant(k_b)	0.1 V-s/rad	Lead of lead screw (L)	2.4 mm
Viscous damping (R_v)	10.2 N-s/m	Damping in guide (R_g)	1 N-s/m
Moment of inertia of flywheel (J_f)	1 kg-m^2	Stiffness of guide (k_f)	10^6 N/m
Gear ratio (G)	1.76	Mass of guide and welding gun (M_s)	4 kg

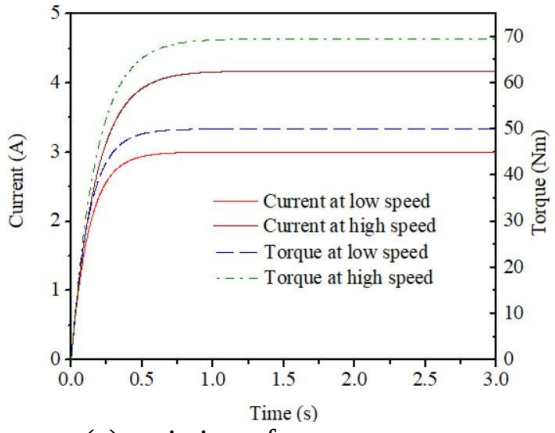

(a) variation of motor current

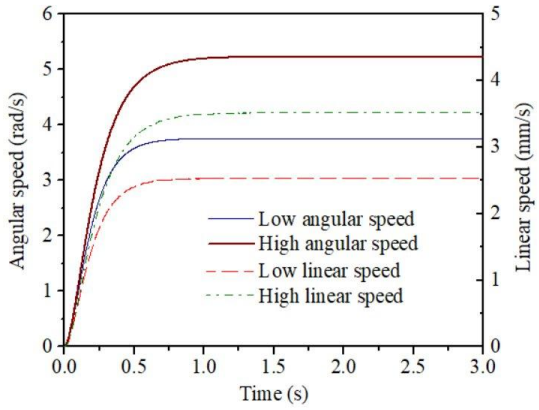

(b) variation of motor angular speed

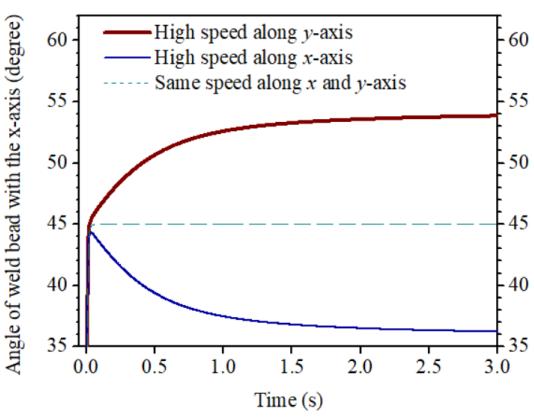

(c) weld path angle prediction

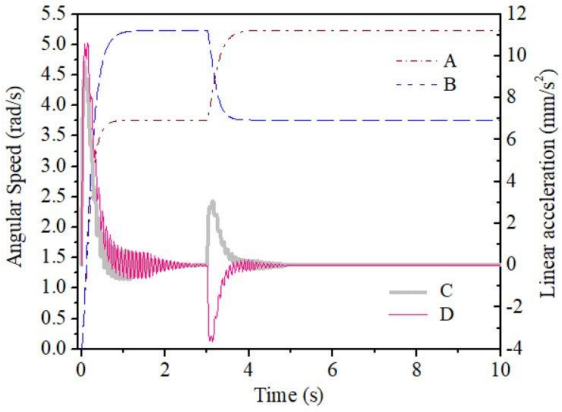

(d) system response for change in speed
A: Increase of speed,
B: Decrease of speed,
C: Increase of acceleration and
D: Decrease of acceleration at 3s

Figure 3.8 System responses of the planar welding setup in single direction

3.4.2 Bond Graph Response in Bi-Directional Motion

The bond graph model of the planar welding with control is discussed in this section. For simulation using this model, the parametric values used are given in Table 3.2. The parameters for the motors and the mechanical components were taken from the user's manual but, the stiffness and damping parameters were chosen suitably.

Table 3.2 Parameters required for modelling in bi-directional motion

Parameters	Values	Parameters	Values
Inductance (L_{ax}, L_{ay})	3.6 mH	Damping in bearing (R_x, R_y)	0.5 N-m-s
Resistance (R_{ax}, R_{ay})	1.13 Ω	Inertia of lead screw (J_{Lx}, J_{Ly})	0.0012 kg-m^2
Motor constant (k_{mx}, k_{my})	0.5 N-m/A	Lead of lead screw (L_x, L_y)	0.02 m
Back emf constant (k_{bx}, k_{by})	0.3 V-s/rad	Damping in guide (R_x, R_y)	1 N-s/m
Viscous damping (R_{vx}, R_{vy})	10.2 N-s/m	Stiffness of guide (K_x, K_y)	10^6 N/m
Inertia of rotary part (J_{fx}, J_{fy})	1 kg-m^2	Mass of guide and weld gun (M_s)	4 kg
Torsional stiffness of shaft (K_{tx}, K_{ty})	10^3 N/m		

The different profiles considered for welding are shown in Fig. 3.9. The circle with radius of 50 mm, ellipse with semi major and minor axis of 50 mm and 30 mm, respectively are considered as two closed profiles for welding. S-shape with straight path

and the radius of the curved path of 75 mm and 25 mm, respectively and Archimedean spiral with radius of 3 mm are considered as two opened profiles for welding.

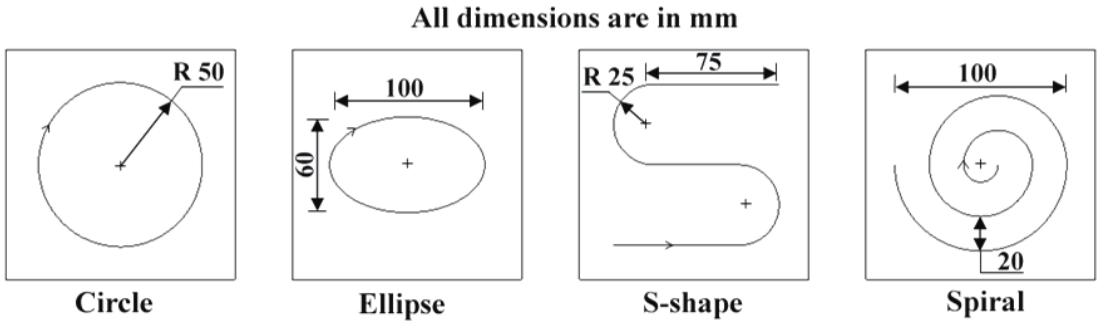

Figure 3.9 Different profiles for welding

Figure 3.10 shows the systems responses of the setup for different welding profiles. The modulated voltage given to the motor by the driver of the motor and the corresponding armature-current during welding in a circular profile are depicted in Fig. 3.10(a). The motor runs for first 0.25 s without any load and the steady-state voltage and the current during that period are 3.2 V, 2.86 A in *x*-direction and 2.5 V, 2.24 A in *y*-direction as shown in the inset of Fig. 3.10(a). As seen in the figure, both current (0.002–2.5A) and the voltage (0.002–2.8V) in both the directions vary during welding in a circular path. As seen in the Fig. 3.10(b), both torque (0.014–1.25 N-m) and the angular velocity (0.004–0.11 rad/s) in both the directions vary during welding in a circular path. The modulated voltage supplied to the motor and the corresponding current in the armature circuit during welding in an elliptical profile are shown in Fig. 3.10(c). Maximum variation of current (0.002–3.04 A) occurs along *x*-direction and the voltage (0.002–3.04 V) in *y*-direction during welding in an elliptical path. In Fig. 3.10(d), maximum changes of torque (0.014–1.52 N-m) and the angular velocity (0.002–0.14 rad/s) vary along *x*-direction. The voltage and current for welding along *x*-direction are 2.03 V and 1.82 A, respectively for S-shaped welding as shown in Fig. 3.10(e). The variation of voltage and current are 0–3.5 V and 0–3.1 A in both *x* and *y*-direction during welding along curved path of S-shaped portion. The torque and angular speed of motor shaft for welding along straight *x*-direction are 0.9 N-m and 0.08 rad/s, respectively for S-shaped welding as shown in Fig. 3.10(f). The variation of torque and rotary speed are 0–1.56 N-m and 0–0.145 rad/s in both *x* and *y*-direction during welding along curved path

of S-shaped portion. As shown in Fig. 3.10(g), the voltage and current gradually increase to 4.6 V and 4.5 A, respectively as the rotational speed is same from starting point to the end point (more radius) during welding on a spiral path. As shown in Fig. 3.10(h), the torque and angular speed also gradually increase to 2.08 N-m and 0.19 rad/s, respectively.

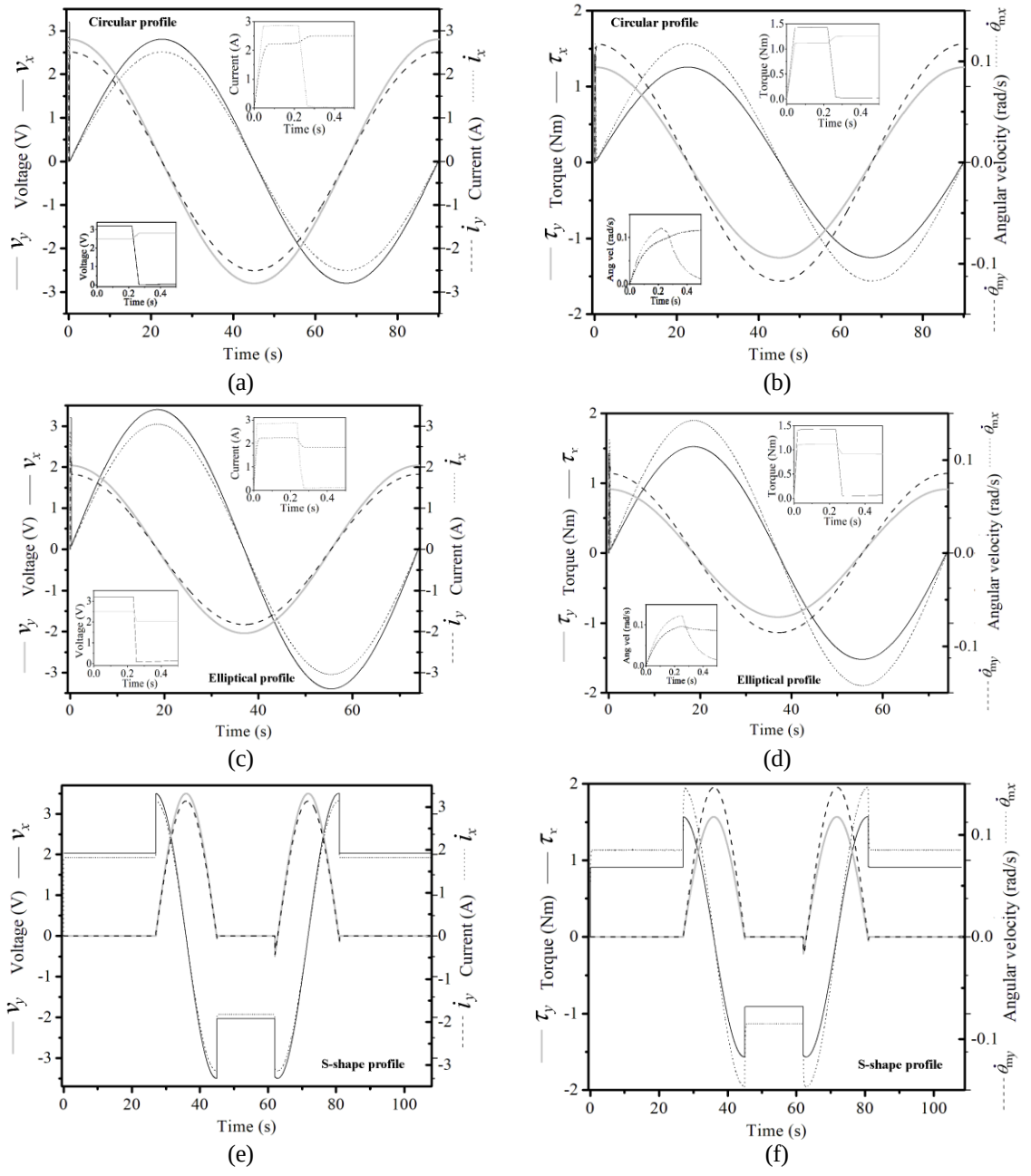

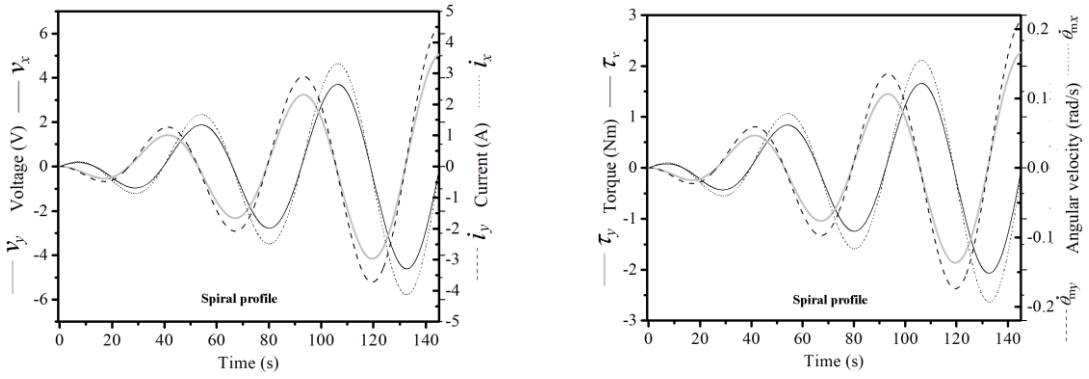

(g) (h)

Figure 3.10 System responses of planar welding setup (a, c, e, g) Input voltage and armature current for circular, elliptical, S-shaped and spiral profile, respectively (b, d, f, h) Torque and angular velocity of motor for circular, elliptical, S-shaped and spiral profile, respectively

The motor with input voltage of 24 V and current of 4.5 A is used for the setup. It is seen from the response of the motor that the voltage and the current behave properly. For the present welding profiles, the torque and the angular velocity of the motors are 3 N-m and 2 rpm, respectively.

In this chapter, the detailed discussion about modelling and fabrication of an automatic movement GMAW setup for depositing weld beads according to the given trajectory is presented. Before proceeding towards the actual fabrication of the setup, CAD model and a wooden prototype were developed for getting concepts. Then, BG modelling technique was used to get the characteristics of the GMAW setup. This modelling technique has been adopted here for modelling of the GMAW setup at two stages of the fabrication of the setup i.e., before and after modifications. Different components such as power source, stepper motor, controller, mechanical parts lying in different energy domains were modelled using BG technique. The BG models along with system responses in single direction as well as in two directions are presented in this section. The layer deposition with different build strategies and joining of dissimilar stainless steels with different activated fluxes using the bi-directional automatic movement GMAW setup would be discussed in details in Chapter-4 and Chapter-5, respectively.

Chapter 4

Layer Deposition with Different Build Strategies

This chapter presents the sequence wise procedure to achieve the research objectives. The plan of experimental work was started with the selection of materials i.e., workpiece, filler material and process parameters through literature review. In this chapter, a bi-directional automatic movement setup was used to perform bead deposition along the desired trajectory and vertical layer deposition for different open and closed profiles utilizing gas metal arc welding (GMAW) were discussed in detail. Gas metal arc welding-based metal-deposition was also implemented to build three dimensional specimens with varying cross-sections through different paths strategies i.e., spiral-in (circular and square) and raster (square, diagonal and circular). The given trajectory was followed by providing programmed inputs to the controller of the setup to deposit metal layer over the layer for producing a positive slope on the lower half and a negative slope on the upper half section of the deposited objects. In order to investigate the mechanical properties and microstructural characterization of the deposited specimens, different testing techniques such as tensile test, bend test, microhardness test, spectroscopy, scanning electron microscopy (SEM), energy dispersive x-ray (EDX) were adopted and those would be presented in the following sections.

4.1 Performance Analysis of Semi-Automatic Movement Setup

The welding gun of a GMAW machine (Tornado MIG350, make: Ador, Bangalore, India) having maximum welding current of 350 A at 60% duty cycle was attached with the fabricated setup for metal depositing purpose as shown in Fig. 3.2(c) (refer Chapter-3). For depositing weld beads at different speeds, process parameters such as welding voltage (V_w) of 23 V and current (I_w) of 110 A were kept constant for all welds. Electrode wire (ER70S-6) of 1.2 mm diameter was used (from the spool) at a feed rate of 8 m/min and the flow rate (15 l/min) of CO_2 as a shielding gas was also kept constant.

Independent (individual) control of drive movement of the present fabricated setup was validated by depositing weld beads on the workpiece at different weld speeds.

Independent control along *x*-axis at a given speed (maintained constant during the weld) was followed by switching off the motion along *y*-axis or vice-versa for welding along a L-shaped path. The variation of weld speed would result in different weld bead width (consequently penetration as heat input rate varies) in the two arms of the L-shape weldment. A simultaneous motion/movement in both the axes would result in an inclined path with respect to the axes. This path may be at 45º (when both *x* and *y* directional speeds are the same) or any other angle depending on the values of the speed of each drive.

4.1.1 Chemical Composition of Workpiece and Sample Preparation

The planar welding using the present automatic movement setup was performed by welding (bead deposition) on low carbon steel (mild steel) workpiece. The chemical compositions of the workpiece material and other details are provided in Table 4.1. The chemical compositions of the substrate and material of electrode wire were obtained using optical emission spectroscopy analysis (Make-Foundry Master by WAS, Germany) as shown in Fig. 4.1(a).

Table 4.1 Work material used in the present study

Workpiece material	Low carbon steel
Composition measured (wt%)	C: 0.104–0.135%, Si: 0.504–1.18%, Mn: 0.824–1.43%, P: 0.0.56–0.217%, S: 0.15%, Fe: balance
Workpiece dimensions	90 mm × 90 mm × 10 mm

After the weld beads were deposited, the complete weld profile was traced with the help of CMM (Accurate Gauging, India) as depicted in Fig. 4.1(b). From the weld profile, the widths of weld at different locations were calculated. Weld beads were cut, polished and etched in order to measure depth of penetration and metallurgical changes with the help of a measuring microscope (Carl Zeiss, Germany) and SEM (JEOL, USA) as shown in Fig. 4.1(c) and Fig. 4.1(d), respectively. The welded samples were transversely sectioned (transverse to weld bead) using chop saw followed by belt grinder for rough polishing. Subsequently, the samples were sequentially polished using different grades of emery papers (from 220 to 2000) and finally, diamond paste polishing on a disc

grinder polisher. The polished samples were etched with nital solution (with concentration of 2% nitric acid and 98% ethanol) for the metallurgical studies.

(a)

(b)

(c)

(d)

Figure 4.1 Instruments used for testing: (a) spectroscopy machine, (b) coordinate measuring machine, (c) profile measuring microscope and (d) SEM machine

4.1.2 Validation of System accuracy with Equal Speeds in Both Directions

The accuracy/effectiveness of the developed system was validated by depositing beads on workpiece with different speed conditions and measuring the uniformity in the weld bead in terms of the profile and width variation. First, weld beads were deposited providing

movement with equal speeds in *x* and *y* directions (both at 3.5 mm/s) with individual motion to each axis. Figure 4.2 shows the transverse cut section of the weld bead geometries obtained at different conditions by depositing beads on the workpiece.

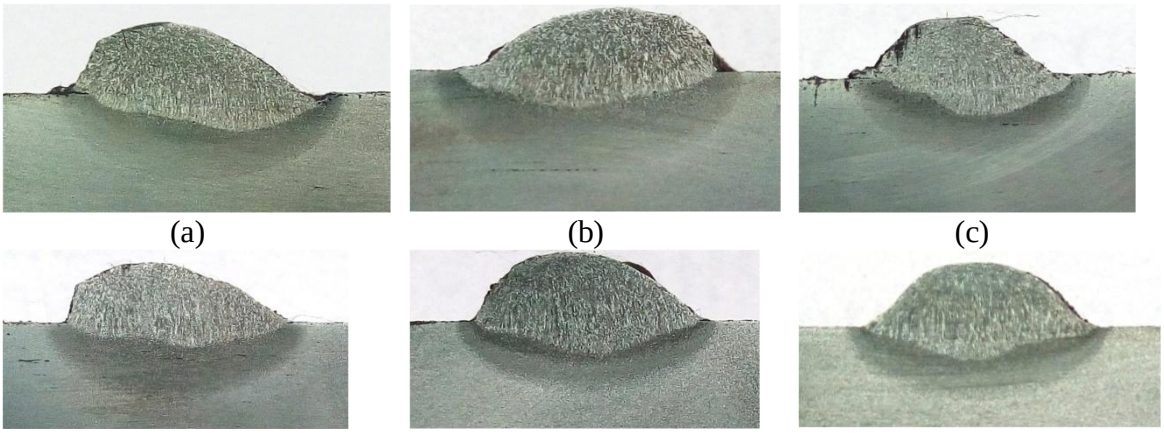

Figure 4.2 Representative weld bead geometry after GMAW using the presently developed setup at: (a) fast speed, L shape, (b) slow speed, L shape, (c) fast speed, 45°, (d) slow speed, 45°, (e) simultaneously fast along *x*-direction and slow along *y*-direction, and (f) simultaneously fast along *y*-direction and slow along *x*-direction

L-shaped deposited bead obtained with equal speeds in individual movements of the welding torch along both the axes is shown in Fig. 4.3(a). The measured profile of the complete weld bead and the variation of bead width measured at different locations of the deposited weld are shown in Fig. 4.3(b) and (c), respectively. The weld speed maintained at high speed (3.5 mm/s) with correspondingly lower heat input rate ($H_i = \frac{V_w . I_w}{S_w} = \frac{23 \times 110}{3.5} = 722.86$ J/mm) resulted in a thinner bead width and low depth of penetration. It might be noted that a reasonably good uniformity in bead width had been achieved with an average bead width of 7.65 mm (with standard deviation, σ = 0.31 mm over 24 data points). The depth of penetration was measured as 3.482 mm and the weld profile was achieved mostly symmetric. It may be noted that during the weld torch movement, it is important to maintain the uniformity in torch angle, arc length or tip-to-workpiece distance in order to preserve the arc stability, uniform heat input and consequently to get smooth material transfer, uniform penetration and symmetric weld profile. With the present setup, a reasonably good uniformity of the weld bead width has been achieved.

The microscopic image (Fig. 4.3(d–g)) of the weld zone shows the fusion and subsequent heat affected zone with grain refinement in the fusion zone. Figure 4.3(d) clearly indicates the boundaries between weld bead-HAZ and HAZ-base metal. Figure 4.3(e) and 4.3(f) show the SEM image of the weld bead and HAZ, respectively. Unaffected micro-structure of base metal is revealed in Fig. 4.3(g). More consistency in grain growth and no solidification micro cracks were observed from SEM images owing to constant work to tip the gap during deposition and consequently, uniform heat input.

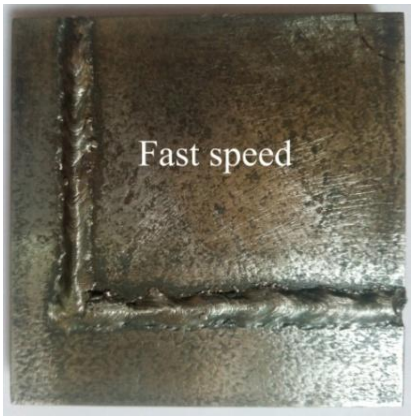

(a) Weld bead appearance

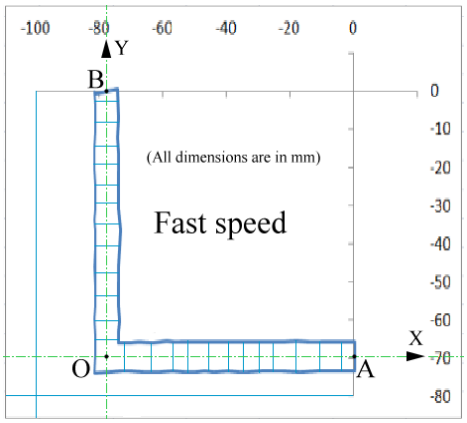

(b) Measured weld profile

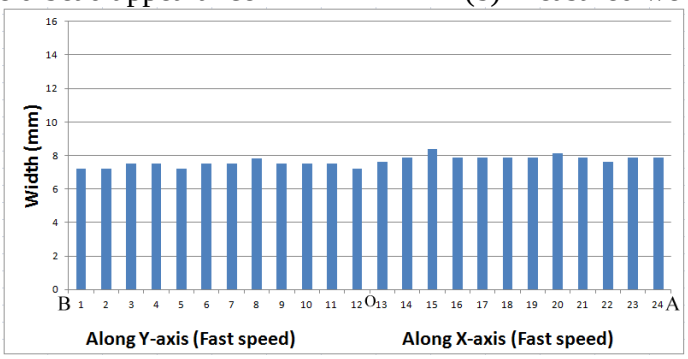

(c) Bead width variation

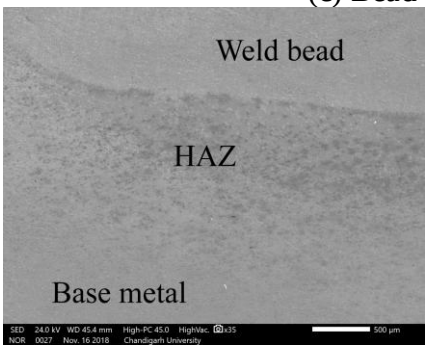

(d) SEM image of interfaces between weld bead, HAZ and base metal

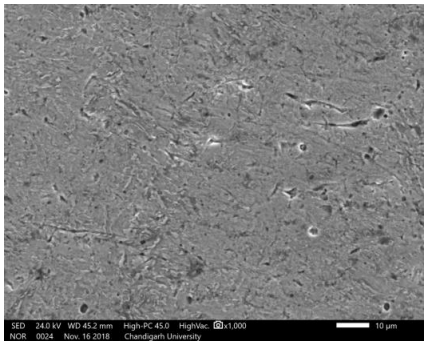

(e) SEM image of Weld bead

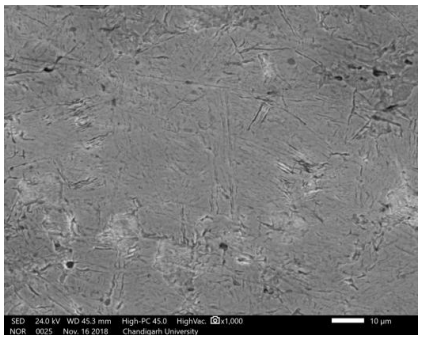

(f) SEM image of HAZ

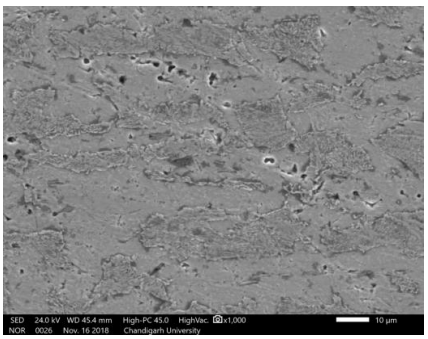

(g) SEM image of base metal

Figure 4.3 Single direction individual movement control with uniform speed in each axis (fast speed 3.5 mm/s, L-shape bead)

Figure 4.4 shows the weld bead appearance, micrographs and the measured profile with the bead width variation for single directional independent movement at slow weld speed (2.5 mm/s). Welding at slower speed is expected to result in wider bead width as well as higher penetration owing to the relatively high heat input rate. The weld bead appearance obtained at slow speed i.e., 2.5 mm/s (correspondingly heat input 1012 J/mm) is shown in Fig. 4.4(a). Figure 4.4(b) shows the measured profile at slow speed. The variations of weld bead width were measured at 24 different locations (refer Fig. 4.4(c)) and the average bead width was calculated as 10.89 mm (σ = 1.34 mm). It may be noted that the depth of penetration and bead width found as 3.843 mm and 10.89 mm, respectively are reasonably higher than observed in previous cases of fast weld-speed. The reasonably good uniformity in bead width along both x and y-directions for both cases with slow and fast weld speeds were thus achieved using the present setup. SEM image (Fig. 4.4(d)) revealed the clear demarcation between the weld bead, HAZ and base metal. Figure 4.4(e) illustrates the grain growth after solidification in the fusion zone. Epitaxial grain zone in HAZ and unaffected base metal are depicted in Fig. 4.4(f) and Fig. 4.4(g), respectively. Slightly higher grain size may be noted when slow speed (higher heat input rate) is used as compared to the previous case of welding at fast speed.

(a) Weld bead appearance

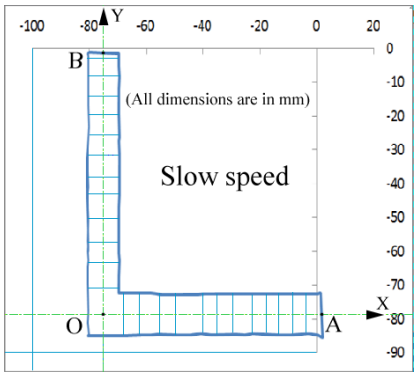

(b) Measured weld profile

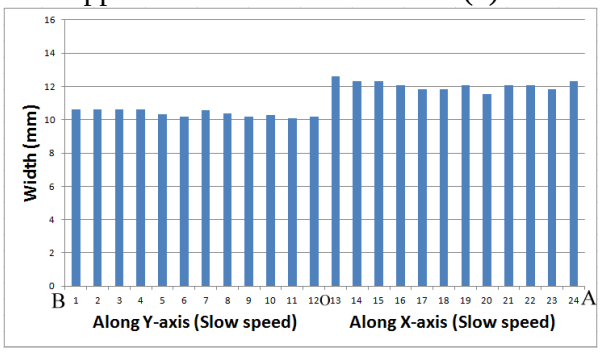

(c) Bead width variation

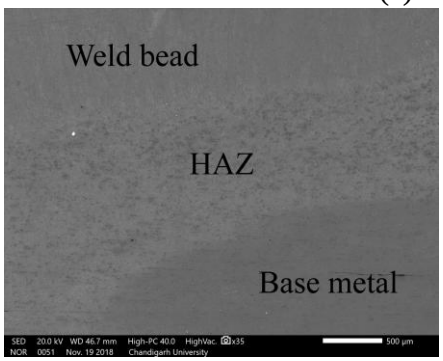

(d) SEM image of interfaces between weld bead, HAZ and base metal

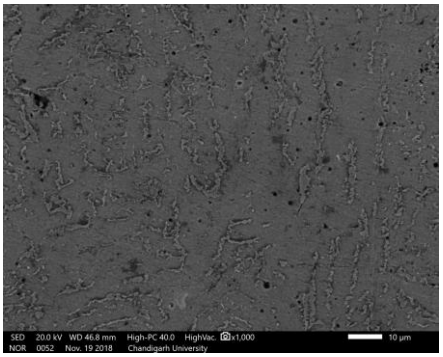

(e) SEM image of Weld bead

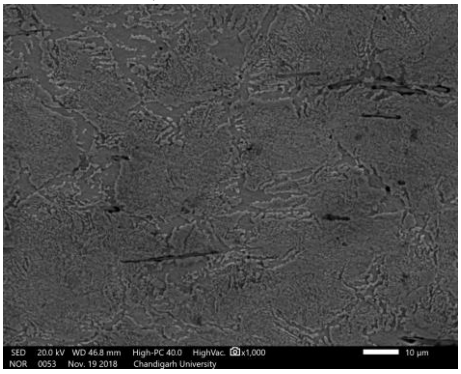

(f) SEM image of HAZ

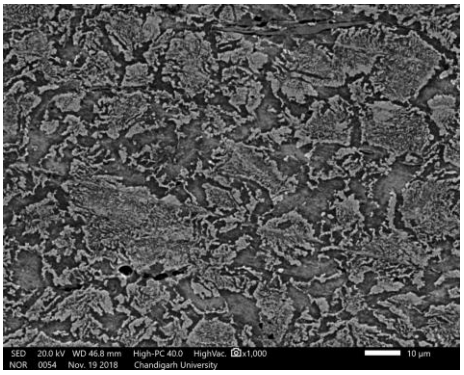

(g) SEM image of base metal region

Figure 4.4 Single direction individual movement control with uniform speed in each axis (slow speed 2.5 mm/s, L-shape bead)

Weld bead appearance during simultaneous movements along both the axes at constant velocity of 3.5 mm/s (fast speed) is shown in Fig. 4.5(a). It was expected to deposit a weld bead at 45º angle with *x* or *y* axis for simultaneous movements in *x* and *y* axes at the same uniform speed. Due to fast speed, the weld bead widths as well as the penetration depth were expectedly low. Measured weld path or weld-profile is shown in Fig. 4.5(b). The depth of penetration of the weld bead was measured as 3.273 mm. The initial variation observed in weld bead width (close to point A, Fig 4.5(b)) could be attributed to the time lag to reach the steady state and stabilize the smooth, uniform speed of movement as well as the initial disturbance during starting of motion of the lead-screw arrangement. Figure 4.5(c) shows the SEM image at the interface of weld fusion and heat affected zone (HAZ). The magnified images at different zones i.e., fusion zone, HAZ and base metal are individually represented in Fig. 4.5(d–f). The distinct grain growth pattern in the weld fusion zone can be clearly observed from the SEM micrographs. Minor variation in bead width at few locations of the deposited weld can be observed due to minor uneasiness in movement, inhomogeneity, spatter *etc*. However, the profile of the deposited bead was very close to the desired one i.e.,, measured orientation at 46.19° in comparison to the expected orientation at 45°.

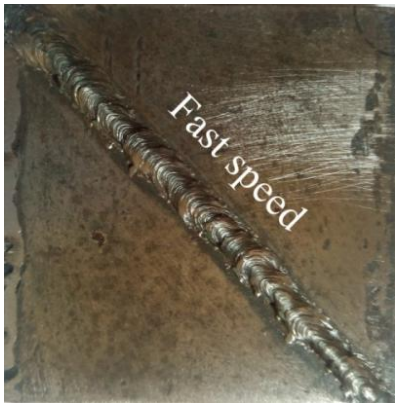

(a) Weld bead appearance

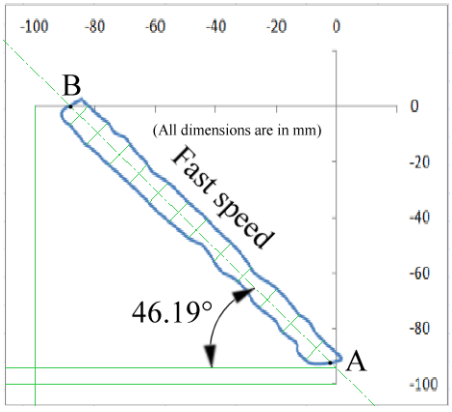

(b) Measured weld profile

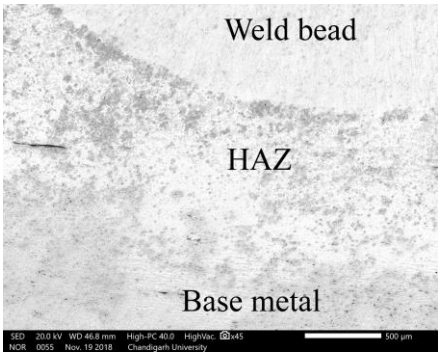

(c) SEM image of interfaces between weld bead, HAZ and base metal

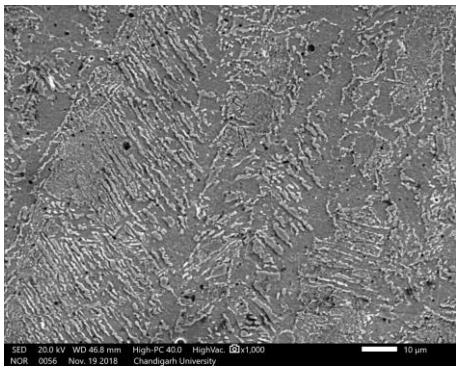

(d) SEM image of Weld bead

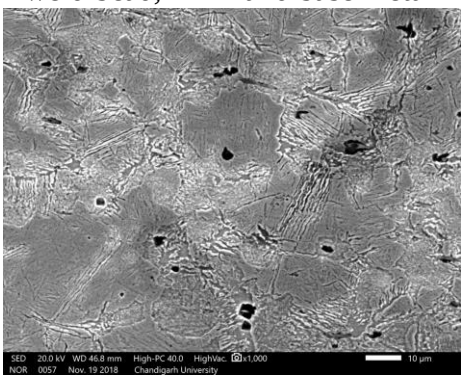

(e) SEM image of HAZ

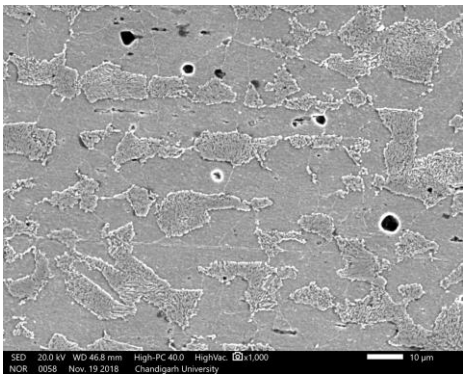

(f) SEM image of base metal region

Figure 4.5 Simultaneous movement control in both axes with uniform high speed (3.5 mm/s) in both axes

Appearance of weld bead during simultaneous movements along both the axes at speed of 2.5 mm/s (slow speed) is shown in Fig. 4.6(a). The deposited weld bead path was measured at an angle of 46.18° in comparison to the desired angle of 45° and the depth of penetration was measured as 3.439 mm. Reasonably uniform bead width of the deposited weld can be noticed in Fig. 4.6(b). However, the deposited bead was relatively wider as compared to the previous case at fast speed (Fig. 4.5(b)) owing to a higher heat input rate and melting at lower welding speed. The SEM micrographs of the weld zone interface as well as the individual regions like weld bead, HAZ and the surrounding base metal region are shown in Fig. 4.6(c–f). Comparatively fine grains were observed in the weld fusion zone as shown in Fig. 4.6(d). Fine dendritic grain growth structure, presence of white ferrite phase and dark grey pearlite phase were observed in HAZ as shown in Fig. 4.6(e). Figure 4.6(f) depicts the unaffected microstructure of base material.

(a) Weld bead appearance

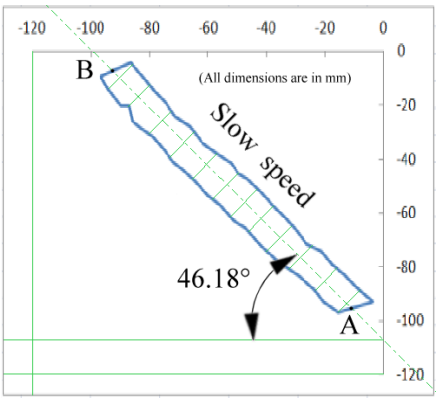

(b) Measured weld profile

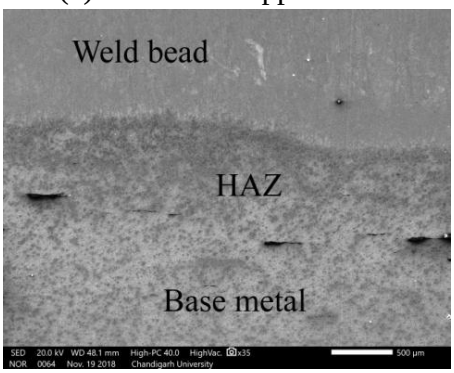

(c) SEM image of interfaces between weld bead, HAZ and base metal

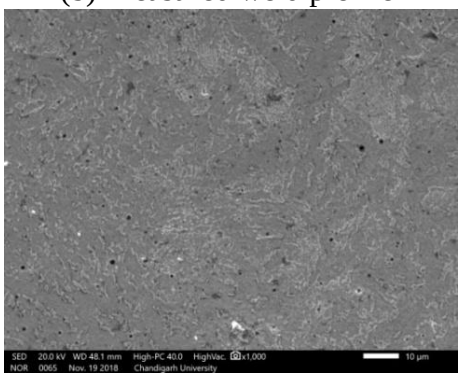

(d) SEM image of Weld bead

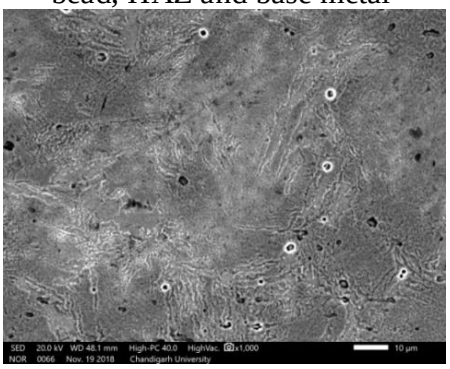

(e) SEM image of HAZ

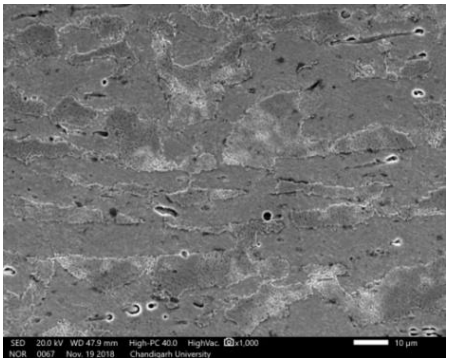

(f) SEM image of base metal region

Figure 4.6 Simultaneous movement control in both axes with uniform speed (2.5 mm/s) in both axes

4.1.3 Validation of System Accuracy with Unequal Speed in X and Y Direction

The fabricated setup was also employed to deposit beads with individually applied unequal speeds along *x* and *y*-axis. Figure 4.7(a) and (b) show the weld bead and width variation with measured weld profile when slow speed (2.5 mm/s) and fast speed (3.5 mm/s) are employed along *x* and *y*-axis, respectively. Thus, bead width as well as penetration of the weld bead along *x*-axis was more than that of *y*-axis. However, a

reasonably uniform bead width can be noted from Fig. 4.7(b) and (c). The average bead width along *x*-axis was 10.52 mm (with σ = 0.79 mm) and for *y*-axis, the average width was 7.44 mm (σ = 0.62 mm). It may be noted that these average widths were very close to the previous results with slow and fast speed (10.89 mm and 7.65 mm, refer results in Fig. 4.4 and 4.3, respectively). This also demonstrates the repeatability of the system in achieving the uniform weld bead width and an error in the range 2.7%–3.4% with respect to the previous case was noted.

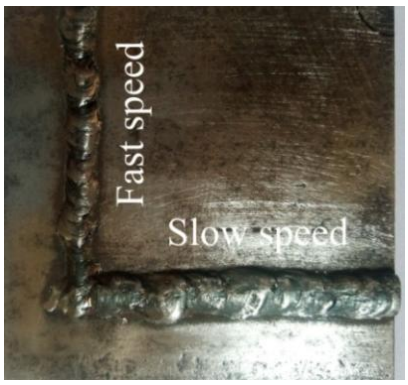

(a) Weld bead appearance

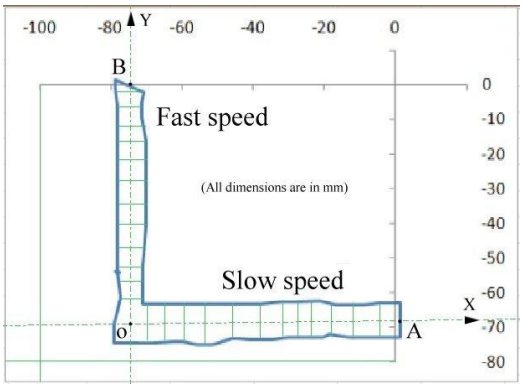

(b) Measured weld profile

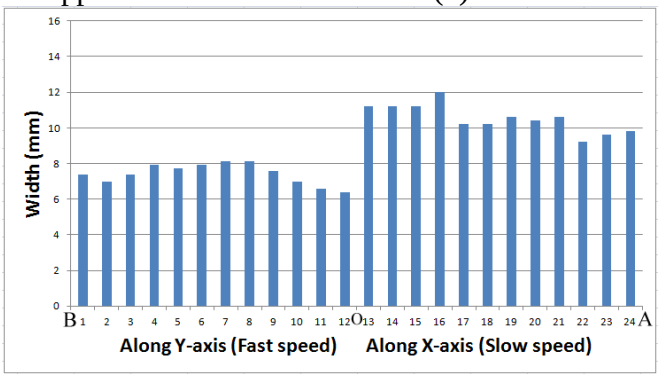

(c) Bead width variation

Figure 4.7 Single direction movement control with slow speed in *x*-axis and fast speed in *y*-axis, L-shape bead

Weld beads deposited with simultaneous movement of carriages in *x* and *y* axes at unequal speed along with the measured bead geometries are shown in Fig. 4.8 and 4.9. The weld bead appearance, measured bead profile for weld with fast speed along *x*-axis with slow speed along *y*-axis (bead deposition along path at angle <45º with *x*-axis) are shown in Fig. 4.8(a) and (b), respectively. The weld bead appearance, measured bead

profile with slow speed along *x*-axis with fast speed along *y*-axis (bead deposition along path at angle >45º with *x*-axis) are shown in Fig. 4.9(a) and (b), respectively. A reasonably uniform bead width measured for both the cases can be noted in Fig. 4.8(b) and 4.9(b). The depths of penetrations for both the cases are 4.015 mm and 3.866 mm, respectively. The morphologies of the fusion zone, HAZ and base metal for both the cases are also presented with the help of the SEM images as shown in Fig. 4.8(c–f) and Fig. 4.9(c–f) where the distinguished gain growth pattern as well as the distribution can be noted.

(a) Weld bead appearance

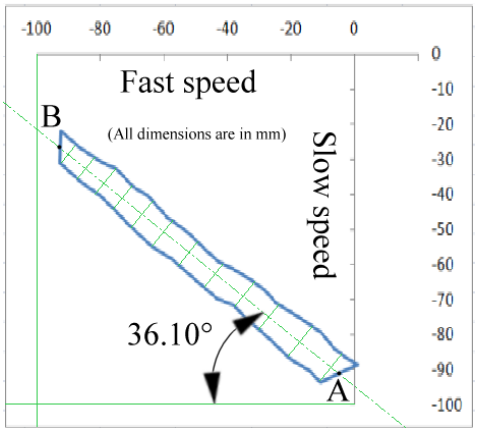

(b) Measured weld profile

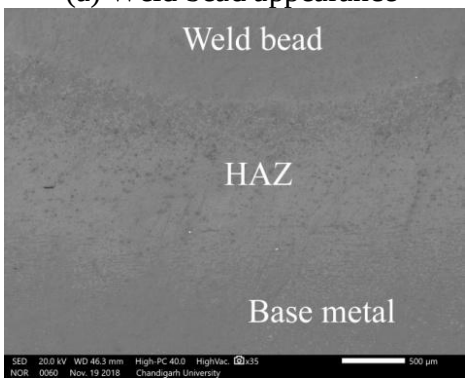

(c) SEM image of interfaces between weld bead, HAZ and base metal

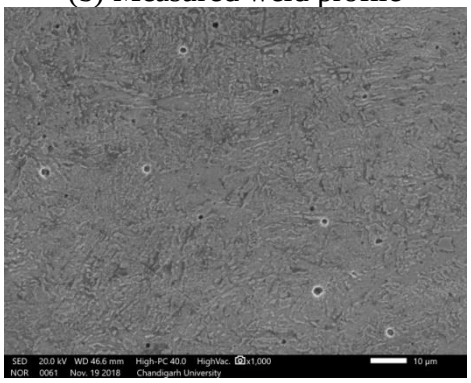

(d) SEM image of Weld bead

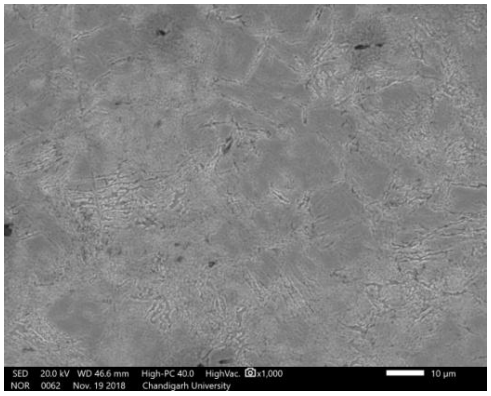

(e) SEM image of HAZ

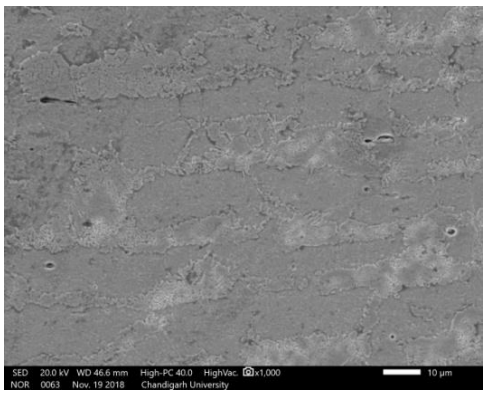

(f) SEM image of base metal

Figure 4.8 Simultaneous movement control in both axes with unequal speed in both axes (fast speed in *x*-axis and slow speed in *y*-axis)

(a) Weld bead appearance

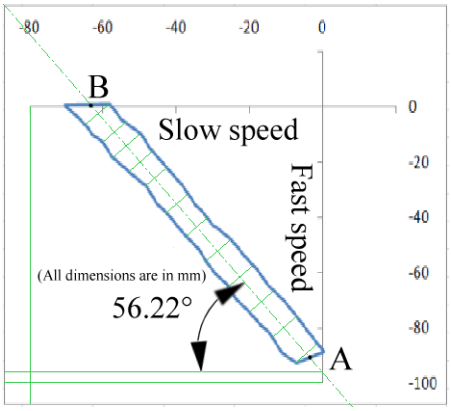

(b) Measured weld profile

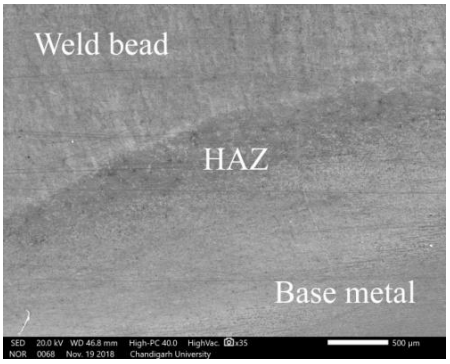

(c) SEM image of interfaces between weld bead, HAZ and base metal

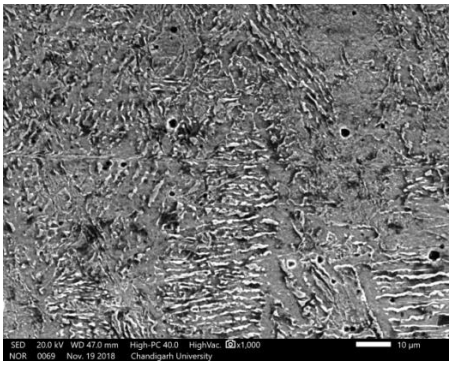

(d) SEM image of weld bead

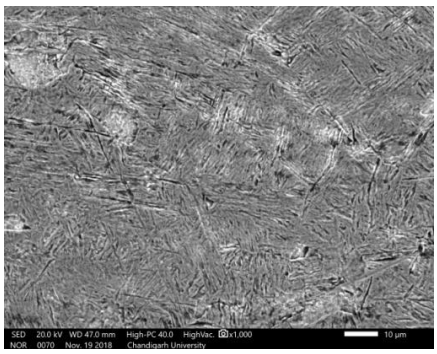

(e) SEM image of HAZ

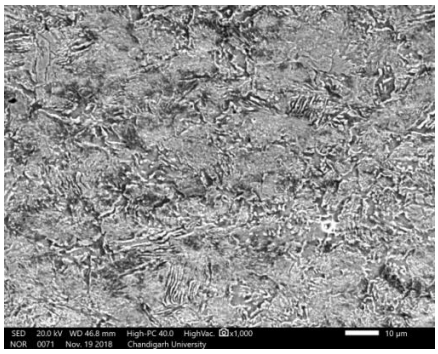

(f) SEM image of base metal

Figure 4.9 Simultaneous movement control in both axes with unequal speed in both axes (slow speed in *x*-axis and fast speed in *y*-axis)

4.1.4 Comparison of Weld Bead between Experimental and Simulation Results

The centre line of the weld path was obtained from the measured profile of each weld bead and the same was compared with the predicted path from the bond graph simulation in order to assess the geometric accuracy of the deposited weld path in comparison to the predicted weld path. For weld bead deposition with individual movements along *x*- and *y*-axis (L-shape weld bead) at slow or fast speed, the deviation from the predicted path was measured from the minimum value of 0.11º to the maximum value of 1.55º as given in Fig. 4.10(a). For the weld bead generated at simultaneous movements of both the axes at equal speeds (either high or low speeds for both *x* and *y*-directions), the deviation in angle from 45º was maximum 1.19º (Fig. 4.10(b)) i.e.,, an error of 2.6%. Maximum of 1.9º deviation was noted for L-shaped weld bead with individual movement at unequal speed i.e.,, slow speed along *x*-direction and high speed along *y*-direction (Fig. 4.10(c)) and minimum 0.1º to maximum 2.42º deviation (error 1.1% to 4.8%) was noted for weld beads deposited with simultaneous movement with unequal speed in both axes (Fig. 4.10(d)). Thus, the present setup was observed to produce satisfactory welding with reasonably uniform weld beads and good geometric accuracy in the weld path.

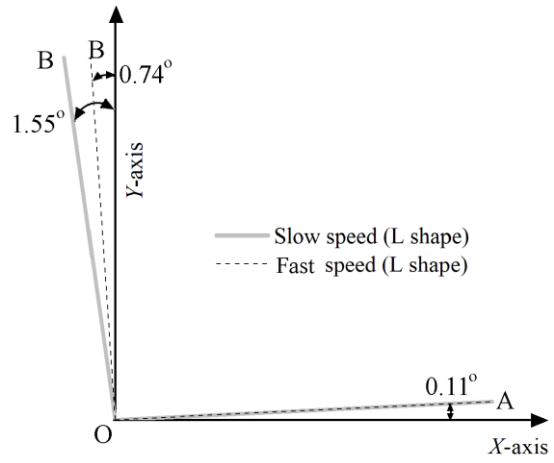

(a) Slow, fast speed, individual movement

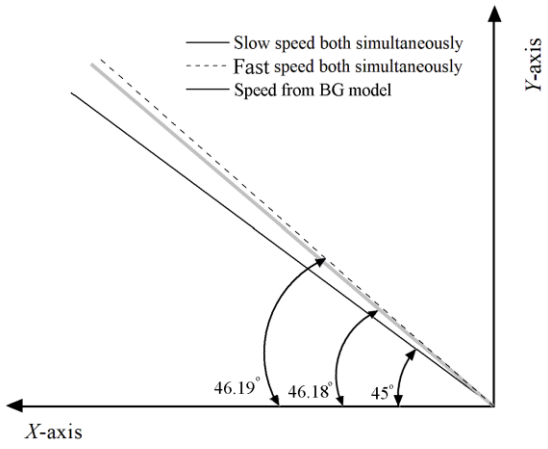

(b) Slow, fast speed, simultaneous movement

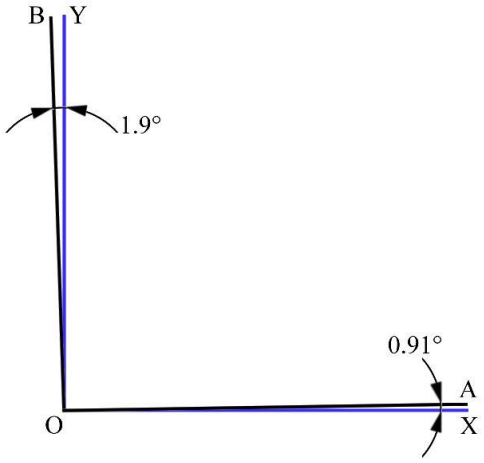

(c) Slow and fast speed, individual movement

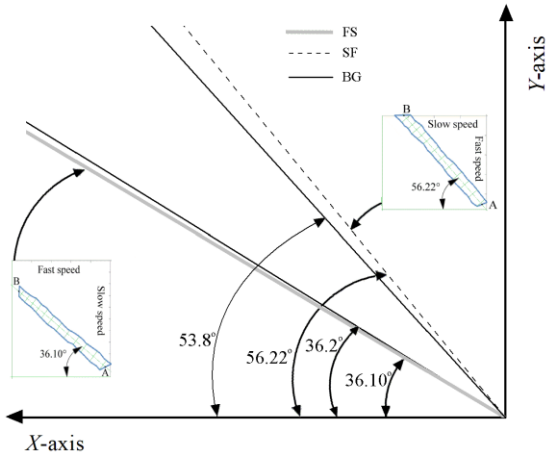

(d) Slow-fast, fast-slow speed, simultaneous movement

Figure 4.10 Weld path geometric accuracy comparison between deposited path and predicted weld paths. (Note for legends of Fig (d) - FS: Simultaneous fast speed and slow speed along *x* and *y*-direction respectively, result from experiment, SF: Simultaneous slow speed and fast speed along *x* and *y*-direction respectively, result from experiment, BG: Simulated values from bond graph model for both the cases)

The absolute errors for the straight path profiles with same or different speeds in two mutually perpendicular directions are depicted in the Table 4.2.

Table 4.2 Absolute errors for various straight path profiles with same or different speeds

S. No.	Condition of Speeds	Type of Weld Bead	Absolute Error		
			From *X*-Direction	From *Y*-Direction	From Desired Direction
1.	Equal speed along both directions	Fast speed with individual movement (L-shape)	0.11˚	0.8 ˚	-
2.		Slow speed with individual movement (L-shape)	0.11˚	1.55˚	-
3.		Fast speed with simultaneous movement (45˚)	-	-	1.19˚
4.		Slow speed with simultaneous movement (45˚)	-	-	1.18˚
5.	Unequal speed in *X* and *Y*-directions	Slow speed in *X*-axis and fast speed in *Y*-axis with individual movement (L-shape)	0.91˚	1.9˚	-
6.		Fast speed in *X*-axis and slow speed in *Y*-axis with simultaneous movement (45˚)	-	-	0.1˚
7.		Slow speed in x-axis and fast speed in y-axis with simultaneous movement (45˚)	-	-	2.42˚

4.2 Single Layer Bead Deposition of Open and Closed Profiles

The planar welding for different closed and opened profiles with this present welding setup was carried out on the workpiece made of low carbon steel. The welding torch (Tornado MIG350) was attached to the automated machine as shown in Fig. 3.2(c) (refer Chapter-3). The selected voltage, current and the inert gas for the welding of all the profiles were 30 V, 200 A and argon gas, respectively. The wire (low carbon steel, ER70S-6) diameter and feed rate were 1.2 mm and 1.16 cm/s, respectively.

The different profiles considered for welding are shown in Fig. 4.11. The circle with radius of 50 mm, ellipse with semi major and minor axis of 50 mm and 30 mm, respectively were considered as two closed profiles for welding. S-shape with straight path and the radius of the curved path of 75 mm and 25 mm, respectively and Archimedean spiral with radius of 3 mm were considered as two opened profiles for welding.

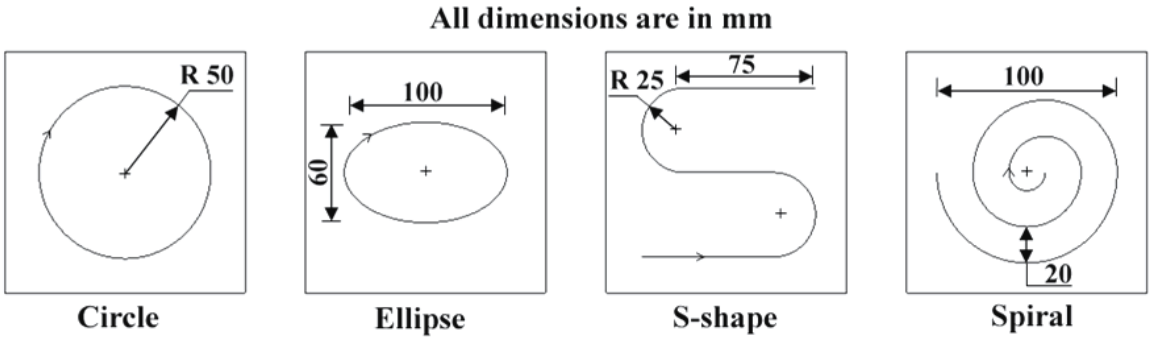

Figure 4.11 Different profiles for welding

4.2.1 Chemical Composition of Workpiece and Sample Preparation

The spectroscopic analysis provides chemical compositions and dimensions of the workpiece materials as provided in Table 4.3. The welded specimens were marked and were cut across a cross-section of the weld bead with the dimensions of 15×20 mm^2 at different locations of the profile to observe the effect of heat accumulation with the span of welding time and welding speed. Then these cut welded samples were grinded using a belt grinder for rough finish. The mirror like finish was achieved using different grades of emery papers (220, 320, 400, 800, 1000, 1500 and 2000) and diamond paste on polishing cloth disc was used in disc grinder polisher (Model - Master, Made - SSA Yanthra Vigyan) to prepare the samples for scanning electron microscopy (SEM). The sufficient flow of water was used to take away the dust particles from the samples during grinding. The nital as etchant with the concentration of 2% nitric with 98% ethanol was used to etch the welded samples for SEM. The samples were immersed into the etchant for about 45 seconds and then, cleaned thoroughly with water to get desired samples for SEM.

Table 4.3 Spectroscopy results of workpiece utilized in the present work

Material	Low carbon steel
Composition (wt%)	C: 0.267–0.276%, Si: 0.231–0.247%, Mn: 0.531–0.535%, P: 0.0429–0.0461%, S: 0.0232–0.0271%, Fe: 98.5%
Dimensions	150 mm × 150 mm × 10 mm

4.2.2 Weld Bead Geometries of Different Profiles

The geometries of weld beads using the fabricated unit for circle, ellipse, S-shape and spiral are shown in Fig. 4.12. The average depth of penetrations for circle, ellipse, S-shape and spiral profiles were 1.65 mm, 1.747 mm, 1.758 mm and 1.85 mm, respectively. Similarly, the average bead height for circle, ellipse, S-shape and spiral profiles were measured as 3.736 mm, 3.94 mm, 3.781 mm and 3.683 mm, respectively. The average welding speed for all the profiles was approximately 3.4 mm/s but it varied in different zones of the profile. During beads deposition for open profiles, the speed of deposition is kept relatively slow as the chosen open profiles (S-shaped and Spiral) have more curvatures than the closed profiles (Circle and Ellipse). For this reason, the average heat input is comparatively higher than those of closed profiles. Hence, the average depth of penetration was found to be more for open profiles.

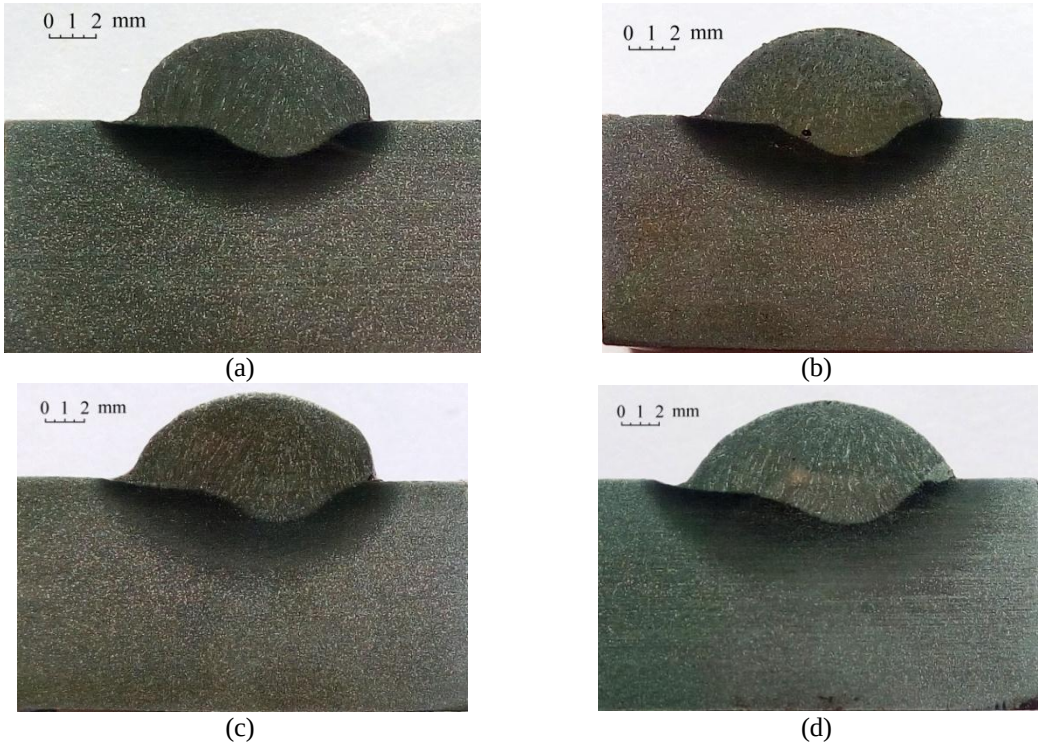

Figure 4.12 Geometries of weld beads for: (a) circle, (b) ellipse, (c) S-shape and (d) spiral

4.2.3 Bead Deposition with Different Profiles

Figure 4.13(a) and (b) show the deposited weld bead for circular profile. Figure 4.13(c) and (d) show the measured weld profile and the variation of width of weld bead at different positions, respectively. The average heat input rate for voltage of 30 V, current of 200 A and for average speed of welding of 3.415 mm/s is 1756.95 J/mm. It has been observed from Fig. 4.13(d) that reasonably better consistency in bead width was obtained with an average bead width of 9.985 mm having standard deviation of 0.535 mm using 20 data points. The trend line based on cubic polynomial regression with coefficient of determination (R^2=27.78%) and the corresponding equation are given in Fig. 4.13(d). Consistency in angle of welding gun, arc length, or CTW distance cause even transfer of material, identical penetration, and consistent weld bead. The scanning electron micrograph of the weld interface zone is shown in Fig. 4.13(e) and micrographs of the weld profile, HAZ and base metal are shown in Fig. 4.13(f), (g) and (h) respectively. Small dendritic structure growth was noticed in the fusion area of weld micrographs, whereas recrystallized grains can be noted in HAZ.

(a)

(b)

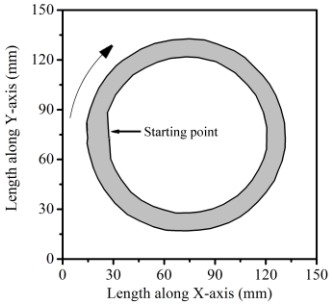

(c)

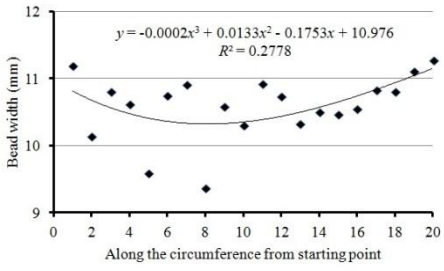

(d)

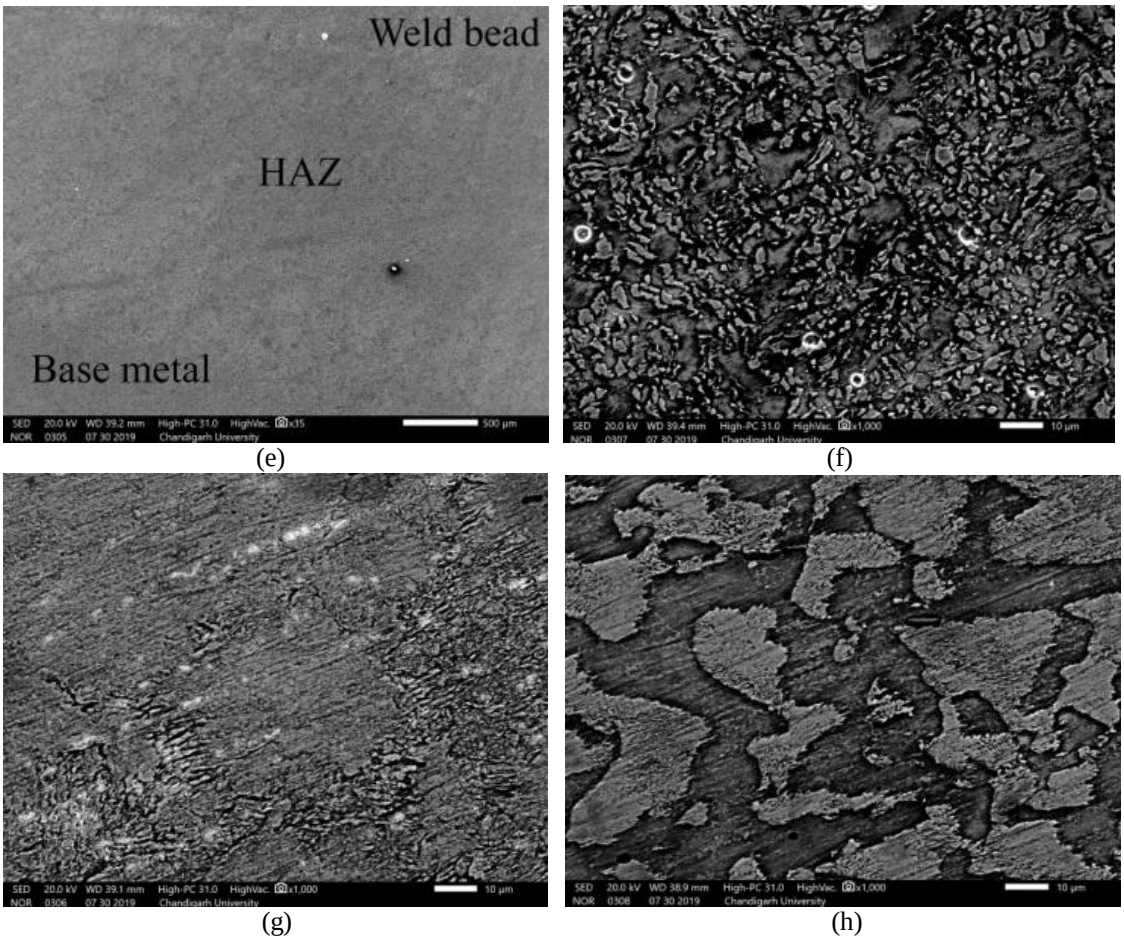

Figure 4.13 Welding of circular profile (a) Weld of circular profile, (b) Weld bead appearance, (c) Measured weld profile, (d) Bead width variation, (e) SEM image of interfaces, (f) SEM image of weld fusion zone, (g) SEM image of HAZ and (h) SEM image of base metal

Figure 4.14(a) and (b) show the deposited weld bead for elliptical profile. Figure 4.14(c) and (d) show the measured weld profile and the deviations of weld profile, respectively. The average heat input rate for voltage of 30 V, current of 200 A and for average 3.449 mm/s speed of welding was 1739.63 J/mm. In GMAW, welding was performed at constant voltage (V_w) and as the welding was done using semi-automatic welding setup, the speed (v) of welding was also constant. With reference to the paper [1], it was seen that the variation current (I_w) using semi-automatic welding was almost uniform. Hence, the heat energy ($V_w I_w / v$) does not fluctuate more and it remains almost uniform. It has been observed from Fig. 4.14(d) that reasonably better consistency in bead width was obtained with an average bead width of 10.091 mm. The trend line based

on cubic polynomial regression with coefficient of determination (R^2=14.59%) and the corresponding equation are given in Fig. 4.14(d). As the coefficient of determination (R^2) was within the allowable limit (30%), the trend of the bead width variation was acceptable. The SEM micrograph of weld interface zone Fig. 4.14(e) shows the boundary of the fusion zone surrounded by the HAZ. The microscopic images of the individual zones e.g., welding area, HAZ and base metal are also shown in Fig. 4.14(f–h).

(a)

(b)

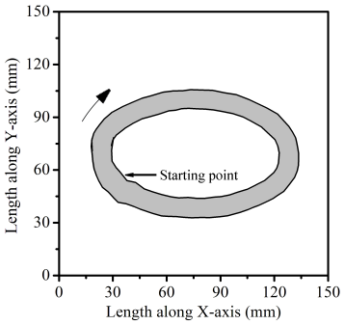

(c)

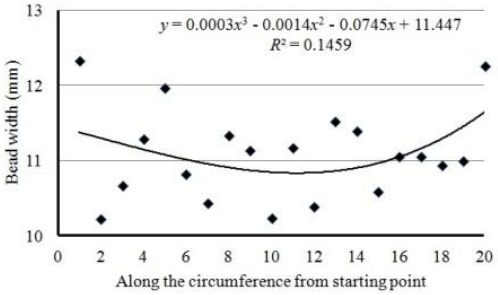

(d)

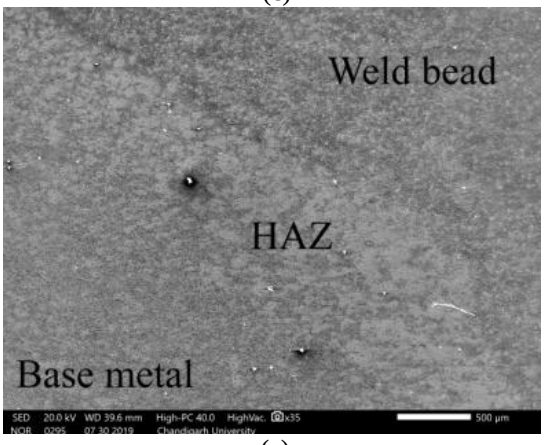

(e)

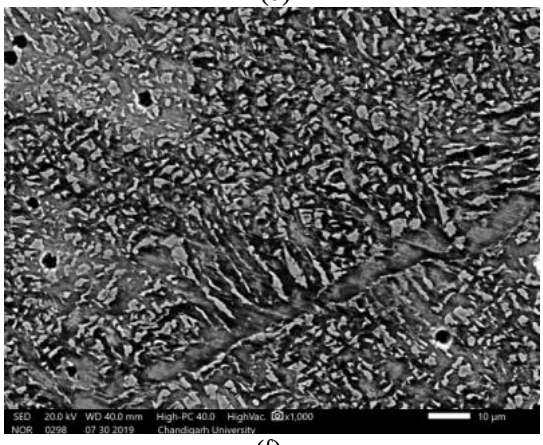

(f)

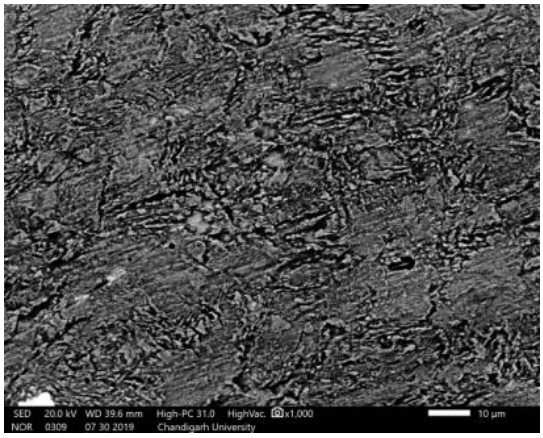

(g)

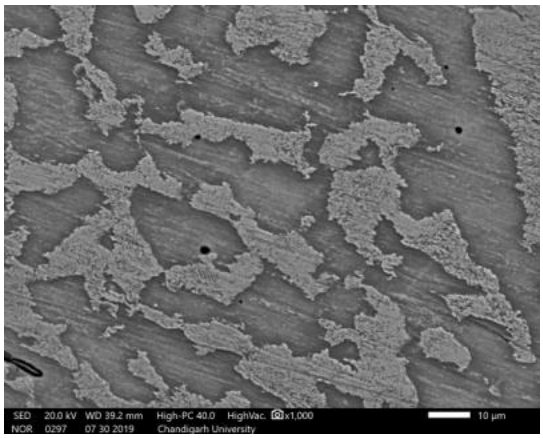

(h)

Figure 4.14 Welding of elliptical profile: (a) Weld of elliptical profile, (b) Weld bead appearance, (c) Measured weld profile, (d) Bead width variation, (e) SEM image of interfaces, (f) SEM image of weld fusion zone, (g) SEM image of HAZ and (h) SEM image of base metal

Figure 4.15(a) and (b) show the deposited weld bead for S-shape profile. Figure 4.15(c) and (d) show the measured weld profile and the deviations of weld profile, respectively. The average heat input rate for voltage of 30 V, current of 200 A and for average 3.401 mm/s speed of welding was 1764.19 J/mm. It has been observed from Fig. 4.15(d) that reasonably better consistency in bead width was obtained with an average bead width of 10.183 mm. The trend line based on cubic polynomial regression with coefficient of determination (R^2=18.43%) and the corresponding equation are given in Fig. 4.15 (d). As the coefficient of determination (R^2) was within the allowable limit (30%), the trend of the bead width variation was acceptable. Figure 4.15(e) shows the SEM micrograph of the boundary of the fusion zone and HAZ. Relatively finer and approximately equiaxed dendritic structure can be noted in weld bead microstructure Fig. 4.15(f) and Fig. 4.15(g) and (h) show the microscopic images of heat-affected zone (HAZ) and base metal, respectively.

(a)

(b)

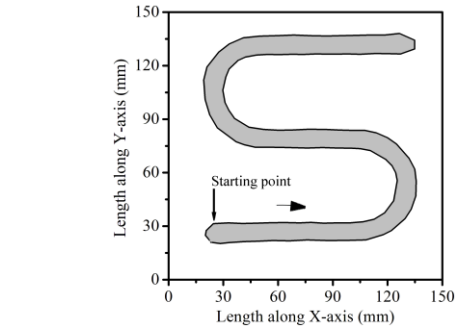

(c)

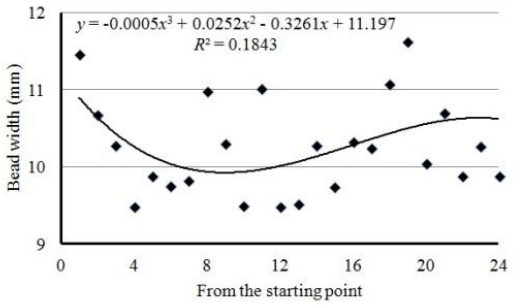

(d)

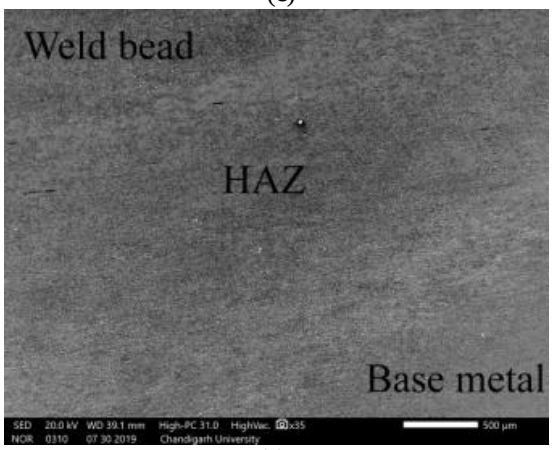

(e)

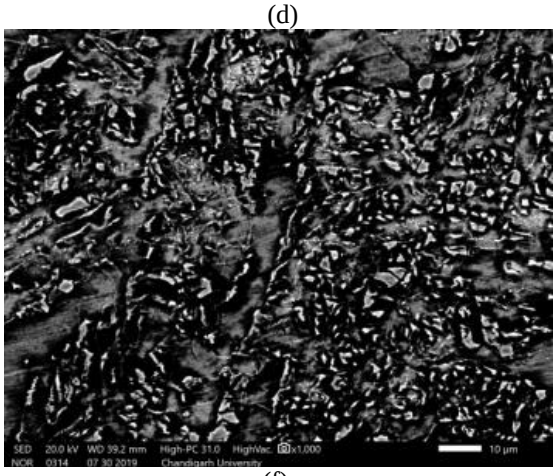

(f)

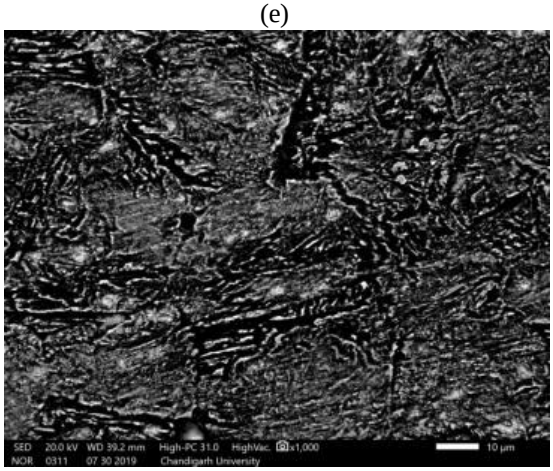

(g)

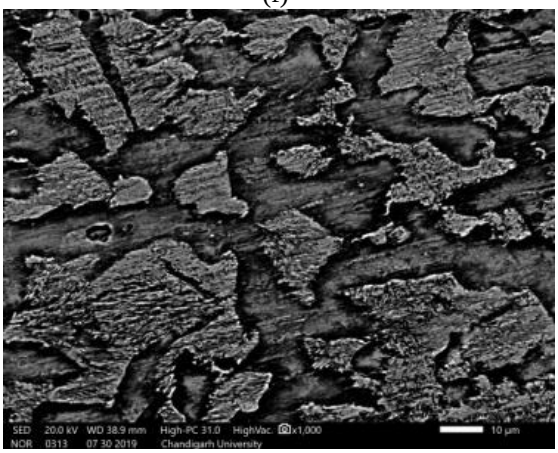

(h)

Figure 4.15 Welding of S-shape profile (a) Weld of S-shaped profile, (b) Weld bead appearance, (c) Measured weld profile, (d) Bead width variation, (e) SEM image of interfaces, (f) SEM image of weld fusion zone, (g) SEM image of HAZ and (h) SEM image of base metal

Figure 4.16(a) and (b) show the deposited weld bead for spiral profile. Figure 4.16(c) and (d) show the measured weld bead and the deviations of weld profile, respectively. The average heat input rate for voltage of 30 V, current of 200 A and for average speed of 3.250 mm/ in welding was 1846.15 J/mm. It has been observed from

Fig. 4.16(d) that reasonably better consistency in bead width was obtained with an average bead width of 10.933 mm. The trend line based on cubic polynomial regression with coefficient of determination (R^2=18.14%) and the corresponding equation are given in Fig. 4.16(d). As the coefficient of determination (R^2) was within the allowable limit (30%), the trend of the bead width variation was acceptable. Figure 4.16(e) shows the weld fusion zone and HAZ interface in the micrograph. At relatively higher input of heat, finer equiaxed grains are observed in weld fusion zone of Fig. 4.16(f), whereas recrystallized grains with grain growth can be observed in the micrograph of HAZ in Fig. 4.16(g). The SEM image of a region from base metal is shown in Fig. 4.16(h).

(a)

(b)

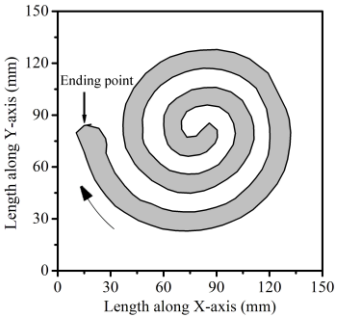

(c)

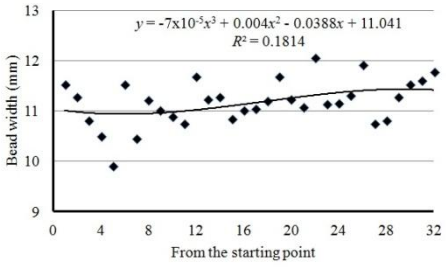

(d)

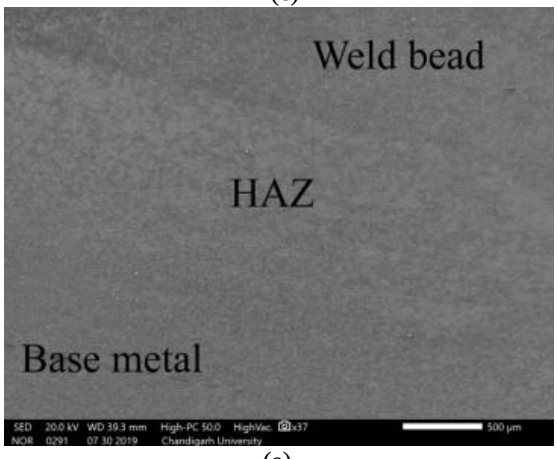

(e)

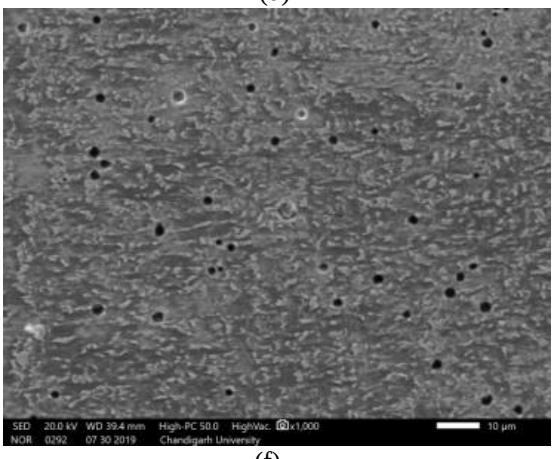

(f)

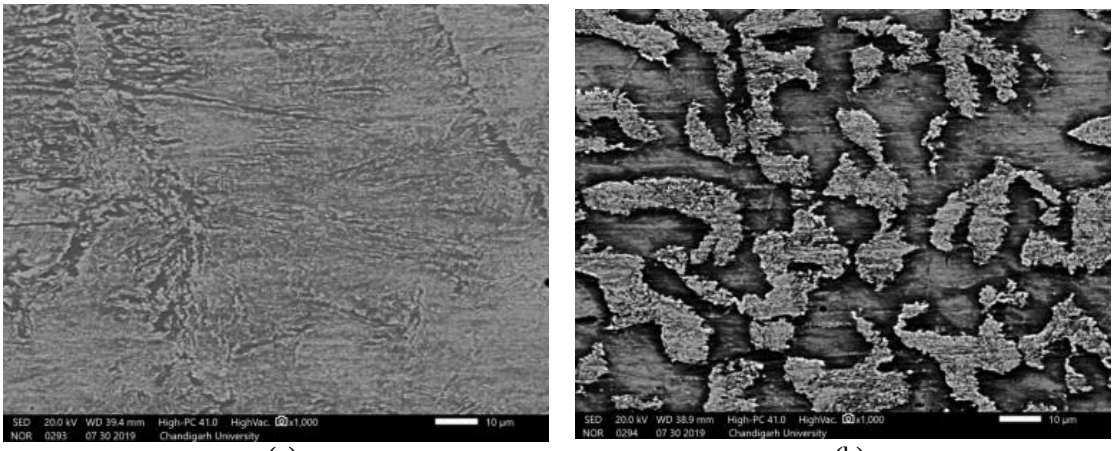

(g) (h)

Figure 4.16 Welding of spiral profile (a) Weld of spiral profile, (b) Weld bead appearance, (c) Measured weld profile, (d) Bead width variation, (e) SEM image of interfaces, (f) SEM image of weld fusion zone, (g) SEM image of HAZ and (h) SEM image of base metal

Figure 4.17 shows the variation of micro-hardness in different zones for different weld profiles. It was observed in all the profiles that micro-hardness was maximum (227.9–264.1 VHN) in the heat affected zone; micro-hardness of the weld-bead (196.7–226.2 VHN) was more than the base metal (182.4–223.7 VHN) but less than the HAZ.

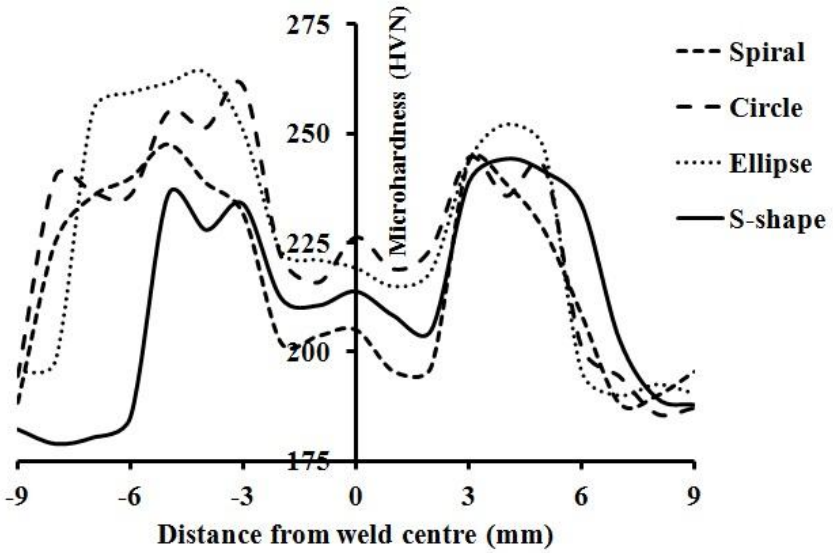

Figure 4.17 Micro-hardness of different profiles

In this experiment of the research work, the speed of deposition during ellipse profile was faster as compared to all other speeds for all other profiles (refer Table 4.4) . Consequently, heat input was lower for ellipse profile than heat inputs for other profiles. This resulted in rapid cooling and formation of fine grain structure. As a result of this, high microhardness value was observed for ellipse profile.

Table 4.4 Speed of welding during deposition of different profiles and corresponding heat input

S. No.	Type of Profile	Speed of welding (mm/s)	Heat Input (J/mm)
1	Ellipse	3.449	1740
2	Circle	3.415	1757
3	S-shape	3.401	1764
4	Spiral	3.205	1846

4.2.4 Comparison of Weld Bead in Experiments and Simulation

The centreline of the predicted path (red coloured dashed line from simulation) was compared with the centreline (black colour) of the measured profiles as shown in Fig. 4.18. The maximum variation between predicted and deposited different profiles is depicted in Table 4.5. A reasonably good accuracy in measured profile with the predicted profile can be noticed for all the geometric profiles validated in the present study. Hence, the two-directional automatic movement system for GMAW improved the quality of the metal printing process. As the average depth of penetration (1.75 mm), average bead height (3.78 mm) and the average bead width (10.28 mm) were almost similar for any complex geometry with 30 V voltage, 200 A current, the fabricated two-directional automated machine for GMAW is suitable for any complex geometry with least process steps with reasonably well and acceptable weld bead quality without requirement of post weld machining at lower cost.

Table 4.5 Maximum variation produced during deposition of different profiles

S. No.	Type of Profile	Maximum Variation (mm)
1	Ellipse	3.44
2	Circle	3.81
3	S-shape	2.98
4	Spiral	3.27

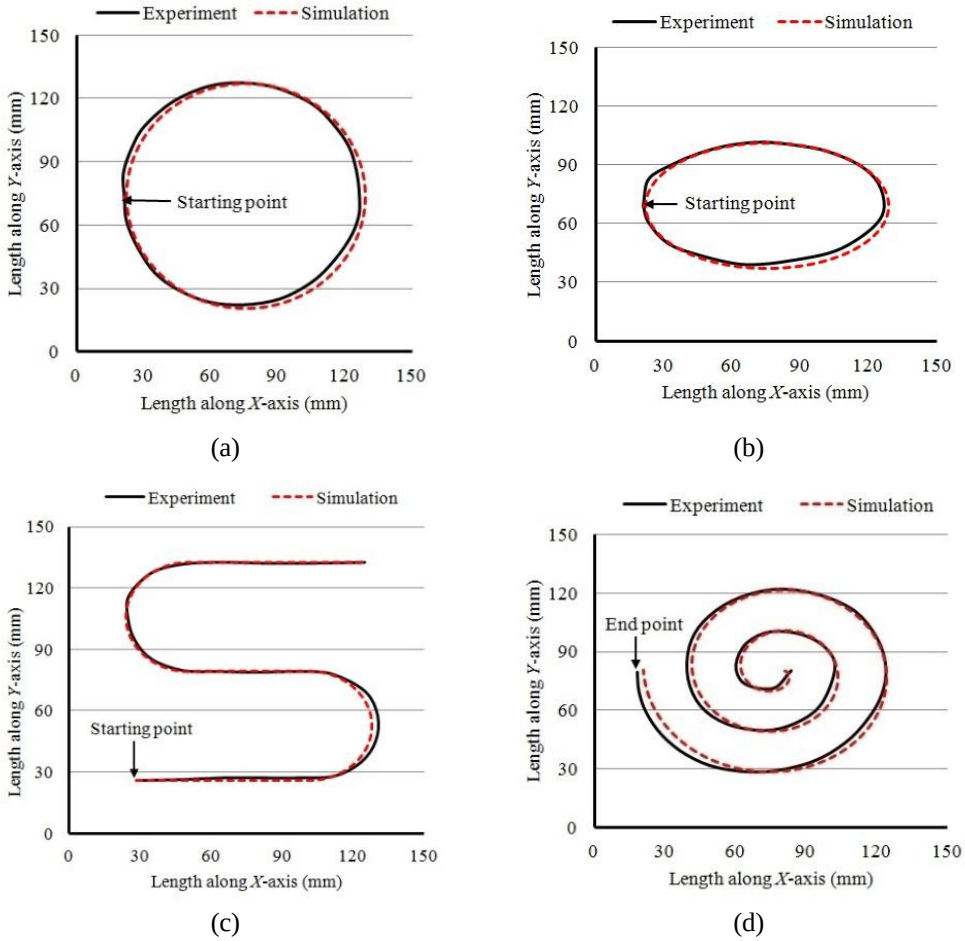

Figure 4.18 Comparison of weld bead in experiment and simulation

4.3 Multi-Layer Bead Deposition of Open and Closed Profiles

The fabricated setup used in the present work to build the layers one above the other for different open and closed profiles using GMAW has already been discussed in the previous chapter. It mainly consists of stepper motors, carriage, transmission system and guide ways. The welding torch was kept perpendicular to the substrate during deposition of all profiles. A trigger was provided under the torch holding device to on/off the welding torch manually whenever required. Low carbon steel was used as a substrate. The wire (ER70S-6) having 1.2 mm of diameter was used for metal deposition using a GMAW machine (Tornado MIG350, make: Ador, Bangalore, India) as shown in Fig.

3.2(c) (refer Chapter-3). Pure argon was supplied during metal deposition to protect the deposited zone from atmospheric contamination.

The closed profiles i.e., cylindrical, elliptical and concave as well as open profiles i.e., semi-cylindrical, double semi-cylindrical and V-profile were fabricated in wall form by depositing total 16 numbers of layers one over the previous one by keeping all process parameters constant such as welding current of 140 A, voltage of 20 V and gas flow rate of 18 l/min. The average deposition speed for circle, semi-circle and double semi-circle is approximately 6.6 mm/s whereas the deposition speed for ellipse, concave and V-profile is approximately 6.55 mm/s which varies in different zones of the profile during metal deposition.

4.3.1 Chemical Composition of Workpiece and Sample Preparation

The chemical composition of the substrate material used to deposit different profiles and other related information is given in Table 4.6. After deposited beads, the profiles of all the metal deposited samples were measured and traced for bead width using coordinate measuring machine (CMM) (Accurate Gauging, India). After that, the deposited metal was cut into small pieces using chop saw; the specimens were grinded up to 2000 grit emery papers and polished by diamond paste. Etching was performed using 2% nital plus 98% ethanol solution for metallurgical examination with the help of measuring microscope and scanning electron microscope (SEM). Selected specimens (a closed type profile i.e., cylindrical profile and an opened type profile i.e., V-profile) were examined using scanning electron microscopy (JSM-IT500, JEOL) equipped with Energy Dispersive X-ray Detector (EDX) to determine the elemental composition in the deposited layers. Subsequently, the micro-hardness of the specimens was measured at three zones i.e., deposited metal, heat affected zone (HAZ) and base metal. The microhardness test was performed using Vickers microhardness tester (make: Metatech Industries, Pune, India, capacity: 1000g) by applying load of 500 g with 20 seconds dwell time.

Table 4.6 Material composition

	Material	Composition (wt%)	Dimensions
Workpiece	Mild steel	C: 0.154–0.158%, Si: 0.234–0.247%, Mn: 0.711–0.780%, P: 0.0302–0.0561%, S: 0.0274–0.0276%, Fe: Balance	200 mm × 200 mm × 10 mm
Welding wire	Carbon steel (ER70S-6)	C: 0.06–0.15, Si: 0.80–1.15, Mn: 1.40–1.85, P: 0.025 max, S: 0.035 max, Cu: 0.50 max: Fe: balance	Diameter 1.2 mm

4.3.2 Different Open and Closed Profiles

Different open and closed profiles were deposited on the substrate to measure the developed bead width and layer height variation. The geometries of all closed profiles (cylindrical, elliptical and concave) as well as open profiles (semi-cylindrical, double semi-cylindrical and V-profile) are shown in Fig. 4.19. Firstly, G-codes programming was used to position the welding torch to follow the given profiles for depositing the metal deposition by controlling both the stepper motors simultaneously through Arduino UNO microcontroller. The transverse cut sections of the deposited metal using fabricated setup for cylindrical, elliptical, concave, semi-cylindrical, double semi-cylindrical and V-profile are shown in Fig. 4.20(j), 4.21(i)–4.24(i) and 4.27(g). The profiles of all the metal deposited samples were measured and traced for bead width and height using coordinate measuring machine (CMM) (Accurate Gauging, India). The average layer height for cylindrical, elliptical, concave, semi-cylindrical, double semi-cylindrical and V-profile are 25.8 mm, 25.6 mm, 25.9 mm, 25.3 mm, 25.8 mm and 25.7 mm, respectively. The average deposition speed for all the profiles is approximately 6.55 mm/s which varies in different zones of the profile during metal deposition.

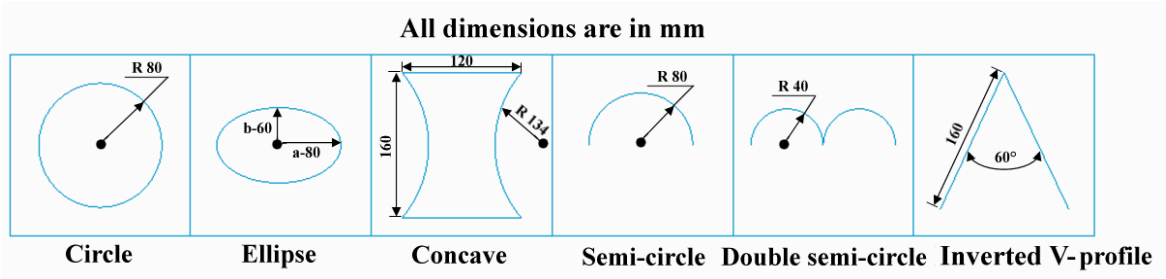

Figure 4.19 Different profiles for material deposition

4.3.3 Bead Deposition with Different Profiles

The deposited metal for cylindrical profile is shown in Fig. 4.20(a). The start point of the deposition is indicated in the figure and the welding torch rotates in the clockwise direction looking from the top. The dimensions of the deposited profile were measured by CMM and the 3D wireframe model based on the measured values of the deposited profile is shown in Fig. 4.20(b). The average inner radius of the cylindrical metal deposition was about 80 mm. The variation in total layer height at different positions as graduated in Fig. 4.20(a) and bead width at a height of 12 mm from the base Fig. 4.20(b) are shown in Fig. 4.20(c) and (d), respectively. The average heat input rate for voltage of 20 V, current of 140 A and for average deposition speed of 6.6 mm/s was 424.24 J/mm. It has been observed from Fig. 4.20(c) and (d), that reasonably better consistency in layer height and bead width, respectively was obtained with an average layer height of 25.8 mm and bead width of 11.2 mm. The consistency in torch angle, arc length, or tip-to-workpiece distance cause even material transfer, identical penetration and symmetric shape. The scanning electron micrograph of the metal deposition zone at the interface between two layers is shown in Fig. 4.20(f). Figure 4.20(e) and (g) show the SEM image of the top and bottom layer, respectively of the interface zone as shown in Fig. 4.20(f). The locations of measurements used in SEM and EDX have been encircled on macrograph indicated by letter f, depicted in Fig. 4.20(j). The EDX spectrum for cylindrical profile is shown in Fig. 4.20(h). The EDX spectrum revealed that Si and Mn along with Fe are present in deposited specimens. The cut section of the deposited specimen for the cylindrical layer deposition is illustrated in Fig. 4.20(j). In this figure, the interface of two layers, heat affected zone (HAZ) and the base metal are properly marked. Figure 4.20(i) and (k) show the SEM image of the HAZ and the base metal, respectively.

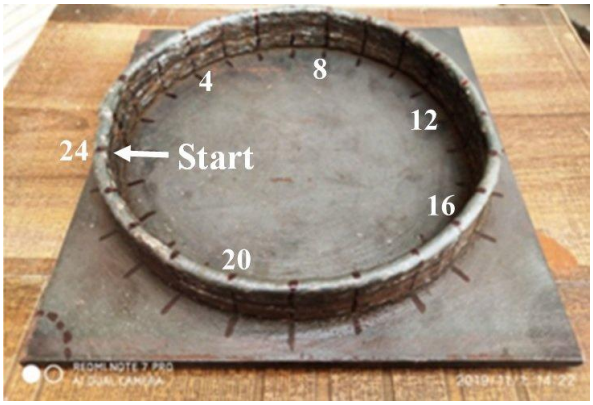

(a)

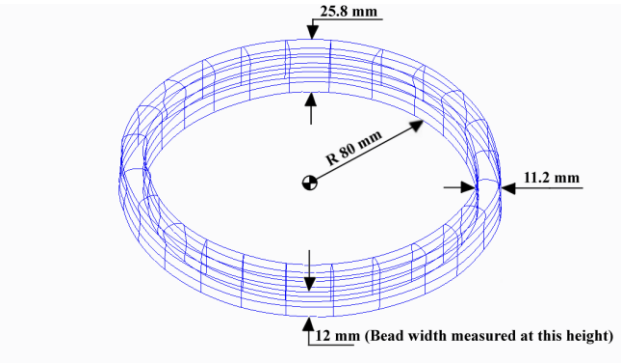

(b)

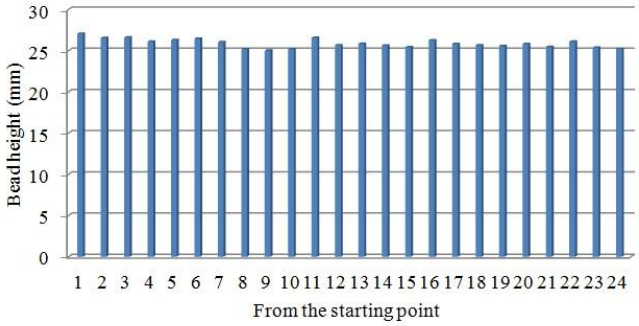

(c)

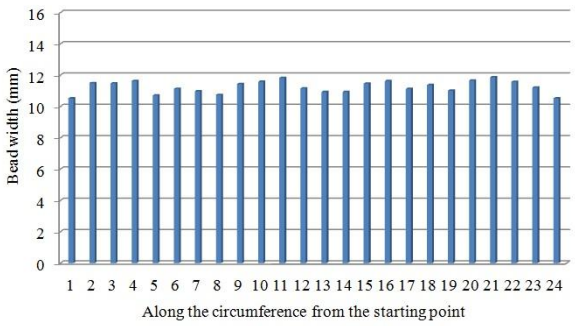

(d)

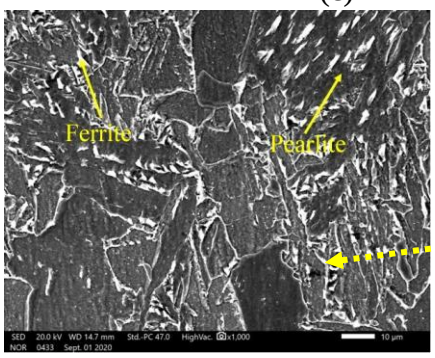

(e)

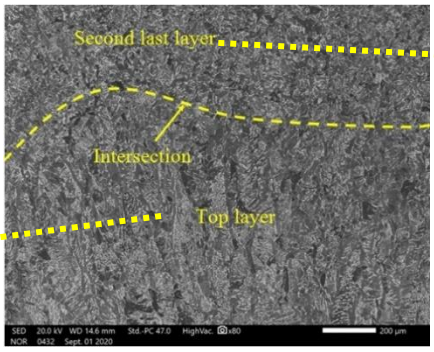

(f)

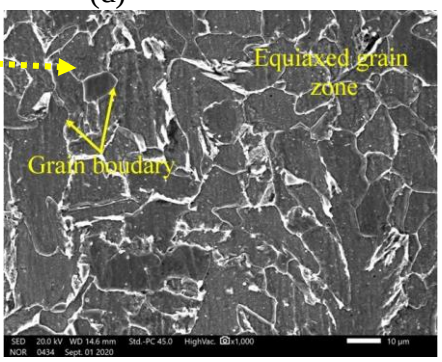

(g)

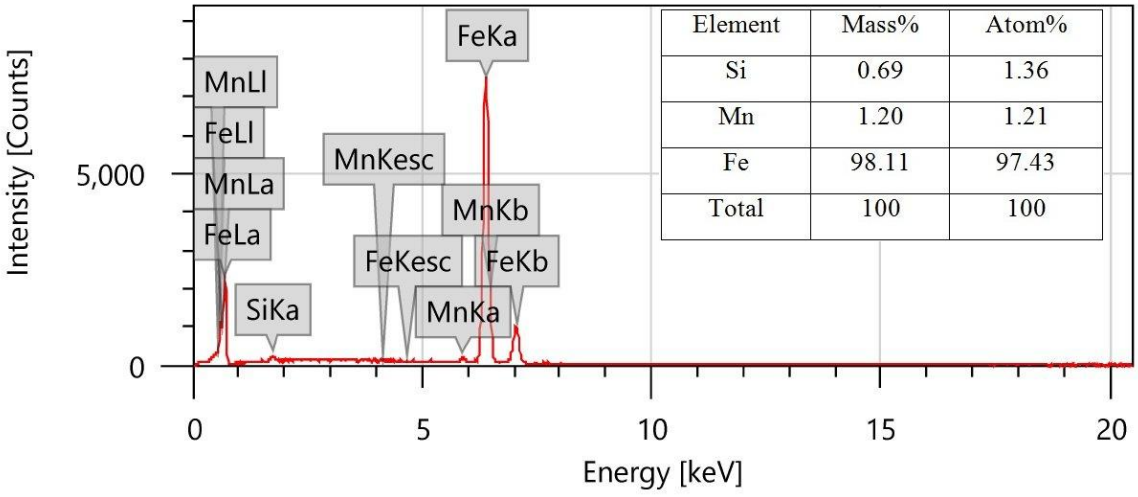

Element	Mass%	Atom%
Si	0.69	1.36
Mn	1.20	1.21
Fe	98.11	97.43
Total	100	100

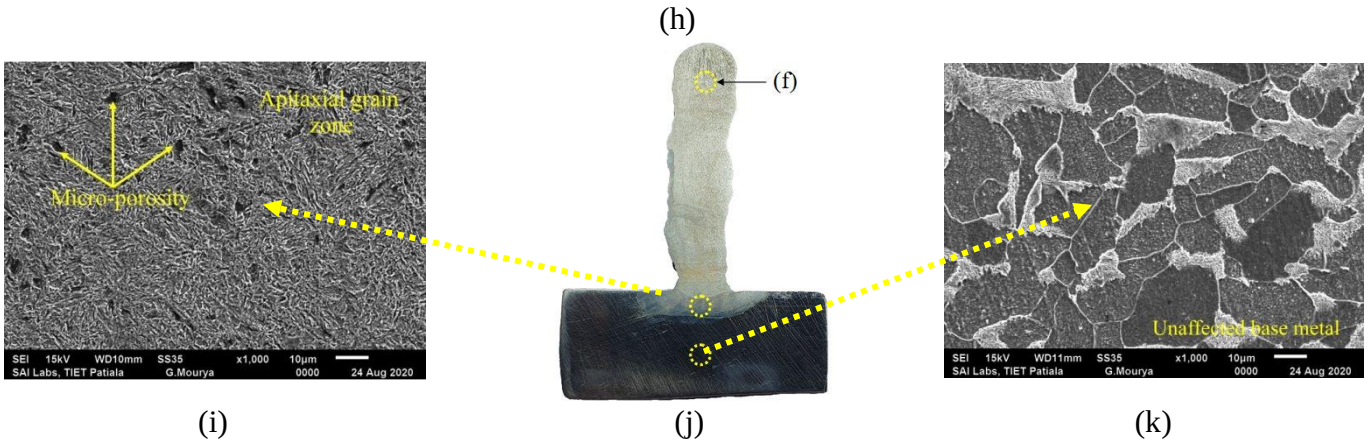

Figure 4.20 Material deposition of cylindrical profile: (a) material deposition of cylindrical profile, (b) wireframe of 3D measured material deposition, (c) layer height variation, (d) bead width variation, (e) SEM image of metal deposition zone at top layer, (f) SEM image of metal deposition zone at intersection of two layers, (g) SEM image of metal deposition zone at second last layer, (h) EDX spectrum showing peaks of elemental composition in deposited specimen, (i) SEM image of HAZ, (j) cross section of metal deposited specimen and (k) SEM image of base metal

Figure 4.21(a) illustrates the deposited material for elliptical profile. The starting point of the deposition is depicted in the figure and metal was deposited in the clockwise direction looking from the top. CMM was used to measure deposited profiles and the 3D wireframe model based on the measured values of the deposited profile is illustrated in Fig. 4.21(b). The average inner half major and minor radius of the elliptical metal deposition were 80 mm and 60 mm, respectively. The variation in total layer height at different positions graduated in Fig. 4.21(a) and bead width at a height of 12 mm from the base Fig. 4.21(b) are shown in Fig. 4.21(c) and (d), respectively. The average heat input rate for voltage of 20 V, current of 140 A and for average deposition speed of 6.5 mm/s is 430.76 J/mm. It has been observed from Fig. 4.21(c) and (d) that reasonably better consistencies in layer height and bead width, respectively were obtained with an average layer height of 25.6 mm and bead width of 11.8 mm. The scanning electron micrograph of the metal deposited zone at the interface between two layers is illustrated in Fig. 4.21(f). Figure 4.21(e) and (g) show the SEM image of the top and bottom layer, respectively of the interface zone as shown in Fig. 4.21(f). The cross section of the specimen for the cylindrical layer deposition is illustrated in Fig. 4.21(i). In this figure,

the interface of two layers, heat affected zone (HAZ) and the base metal are properly marked. Figure 4.21(h) and (j) show the SEM image of the HAZ and the base metal, respectively.

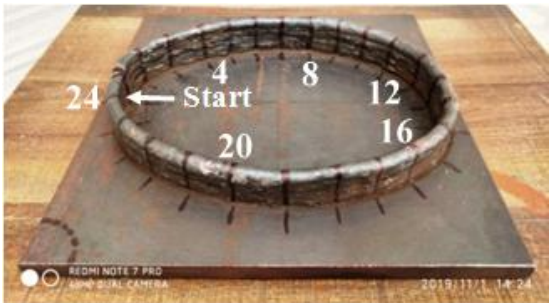

(a)

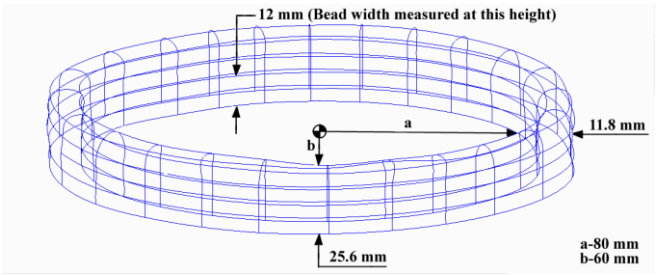

(b)

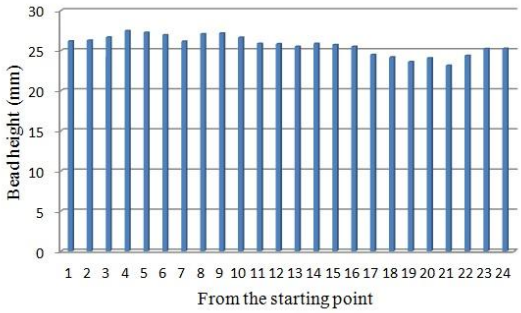

(c)

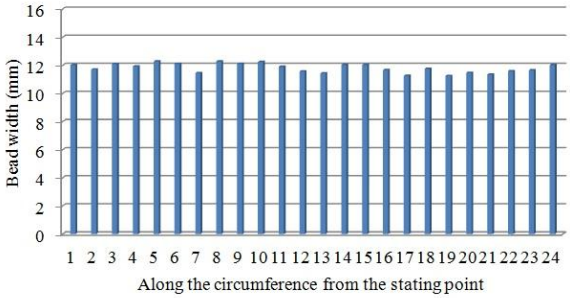

(d)

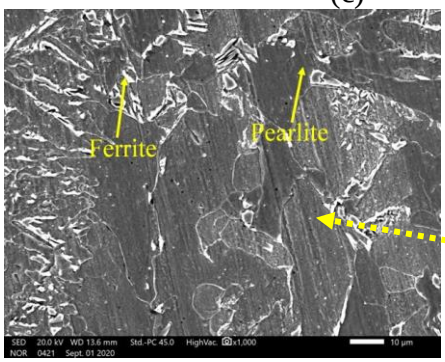

(e)

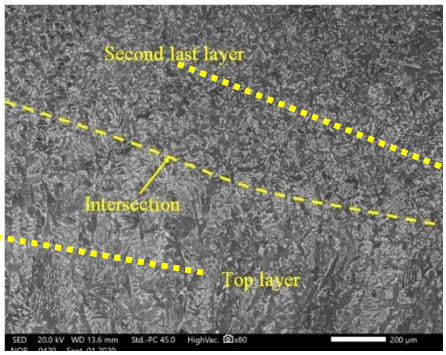

(f)

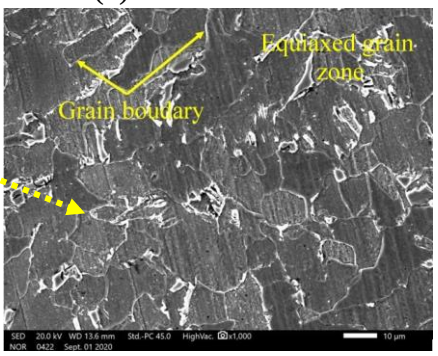

(g)

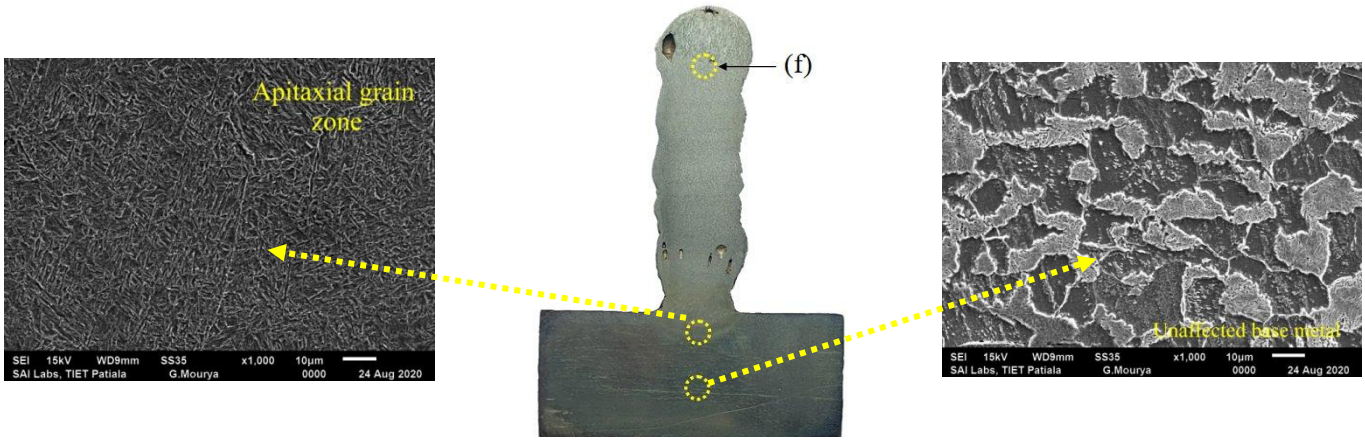

Figure 4.21 Metal deposition of elliptical profile: (a) material deposition of cylindrical profile, (b) wireframe of 3D measured material deposition, (c) layer height variation, (d) bead width variation, (e) SEM image of metal deposition zone at top layer, (f) SEM image of metal deposition zone at intersection of two layers, (g) SEM image of metal deposition zone at second last layer, (h) SEM image of HAZ, (i) cross section of metal deposited specimen and (j) SEM image of base metal

The deposited metal for closed concave profile is illustrated in Fig. 4.22(a). There is a clear indication of the start point of the metal deposition in the figure and the welding torch follows the contour in the clockwise direction looking from the top. The dimensions of the deposited profile were measured by CMM and the 3D wireframe model based on the measured values of the deposited profile is shown in Fig. 4.22(b). The average radius of the concave metal deposition was 134 mm. The variation in total layer height at different positions graduated in Fig. 4.22(a) and bead width at a height of 12 mm from the base Fig. 4.22(b) are shown in Fig. 4.22(c) and (d), respectively. The average heat input rate for voltage of 20 V, current of 140 A and for an average deposition speed of 6.5 mm/s was 430.76 J/mm. It has been observed from Fig. 4.22(c) and (d) that reasonably better consistencies in layer height and bead width, respectively were obtained with an average layer height of 25.9 mm and bead width of 11.6 mm. The scanning electron micrograph of the deposited zone at the interface between two layers is shown in Fig. 4.22(f). Figure 4.22(e) and (g) illustrate the SEM image of the top and bottom layer, respectively of the interface zone as shown in Fig. 4.22(f). The cut section of the specimen for the cylindrical layer deposition is shown in Fig. 4.22(i). In this

figure, the interface of two layers, heat affected zone (HAZ) and the base metal are properly marked. Figure 4.22(h) and (j) show the SEM image of the HAZ and the base metal, respectively.

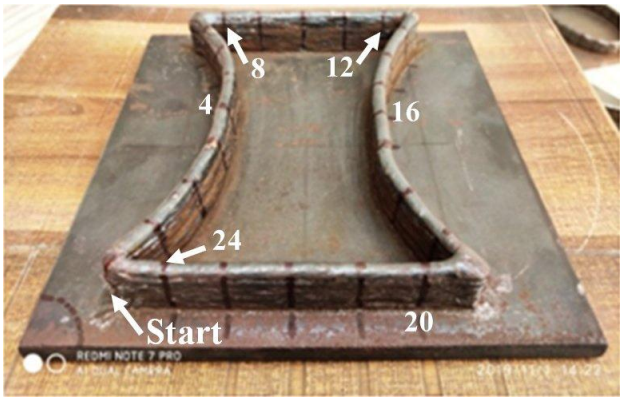

(a)

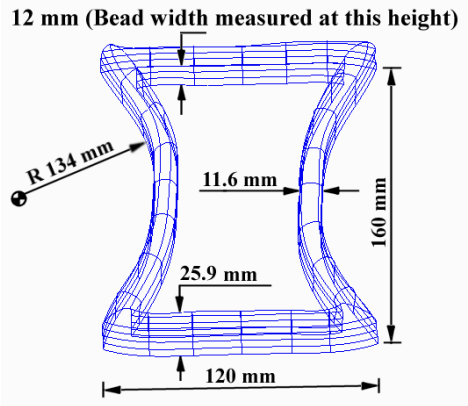

(b)

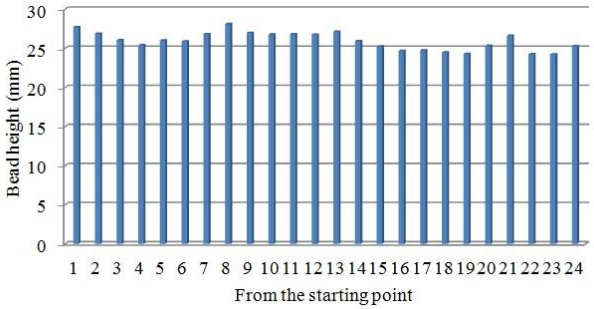

(c)

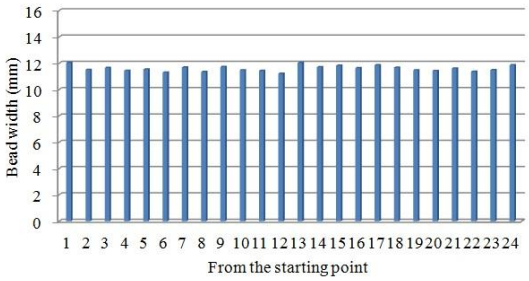

(d)

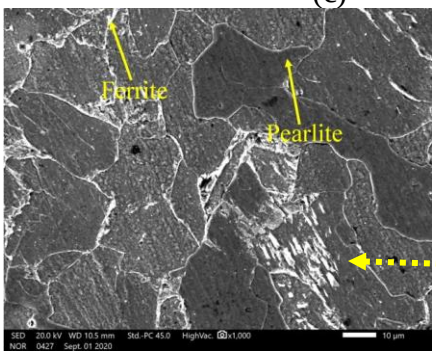

(e)

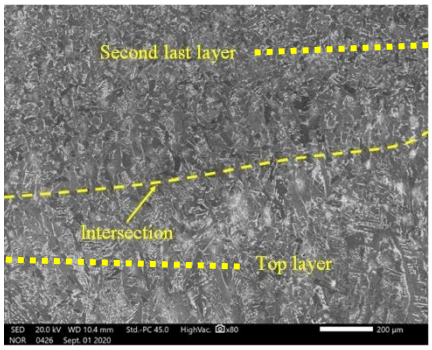

(f)

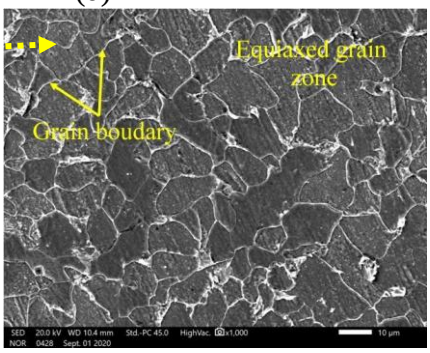

(g)

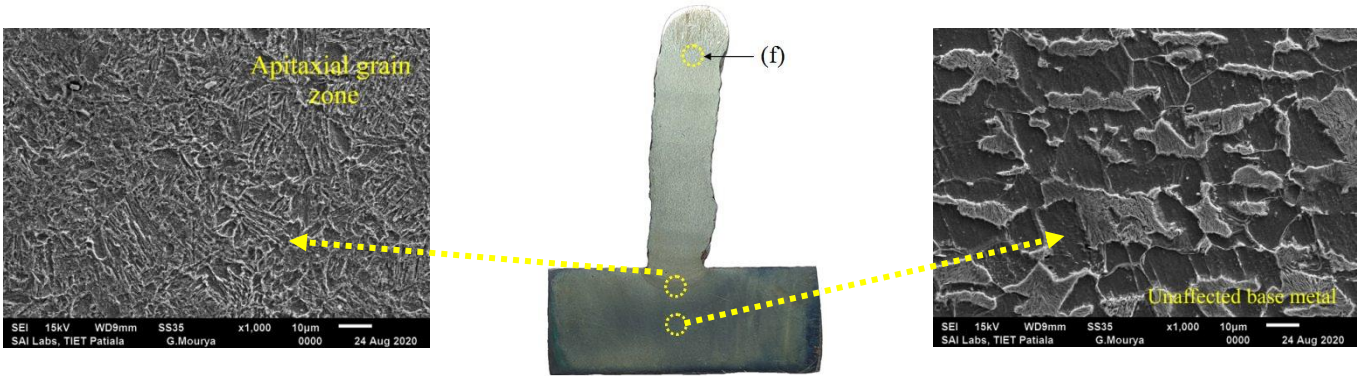

(h) (i) (j)

Figure 4.22 Metal deposition of concave profile: (a) material deposition of cylindrical profile, (b) wireframe of 3D measured material deposition, (c) layer height variation, (d) bead width variation, (e) SEM image of metal deposition zone at top layer, (f) SEM image of metal deposition zone at intersection of two layers, (g) SEM image of metal deposition zone at second last layer, (h) SEM image of HAZ, (i) cross section of metal deposited specimen and (j) SEM image of base metal

The metal deposited layer by layer for a semi-cylindrical profile is shown in Fig. 4.23(a). The starting of the deposition is revealed from the figure and the welding torch rotates in the clockwise direction looking from the top. The deposited profile was measured by CMM and subsequently the 3D wireframe model based on the measured values of the deposited profile is shown in Fig. 4.23(b). The average radius of the semi-cylindrical metal deposition was 80 mm. The variation in total layer height at different positions graduated in Fig. 4.23(a) and bead width at a height of 12 mm from the base Fig. 4.23(b) are shown in Fig. 4.23(c) and (d), respectively. The average heat input rate for voltage of 20 V, current of 140 A and for average deposition speed of 6.6 mm/s was 424.24 J/mm. It has been observed from Fig. 4.23(c) and (d) that reasonably better consistencies in layer height and bead width, respectively were obtained with an average layer height of 25.3 mm and bead width of 11.1 mm. The scanning electron micrograph of the metal deposited zone at the interface between two layers is shown in Fig. 4.23(f). Figure 4.23(e) and (g) show the SEM image of the top and bottom layer, respectively of the interface zone as shown in Fig. 4.23(f). The cross section of the specimen for the semi-cylindrical layer deposition is shown in Fig. 4.23(i). In this figure, the interface of

two layers, heat affected zone (HAZ) and the base metal are properly marked. Figure 4.23(h) and (j) show the SEM image of the HAZ and the base metal, respectively.

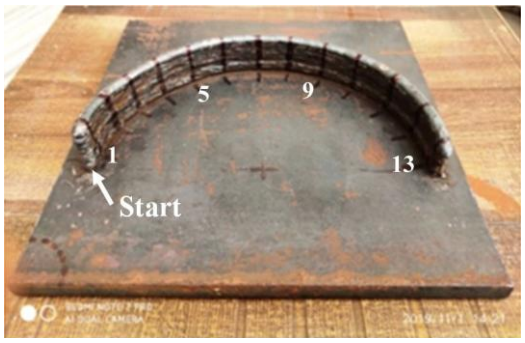

(a)

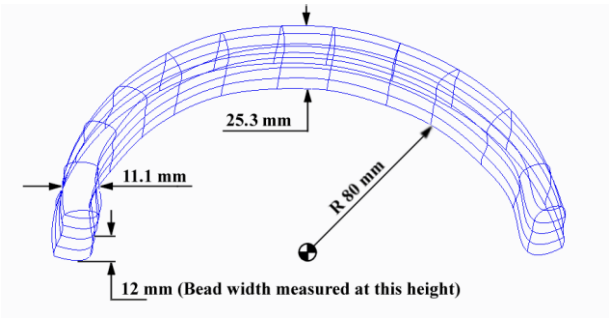

(b)

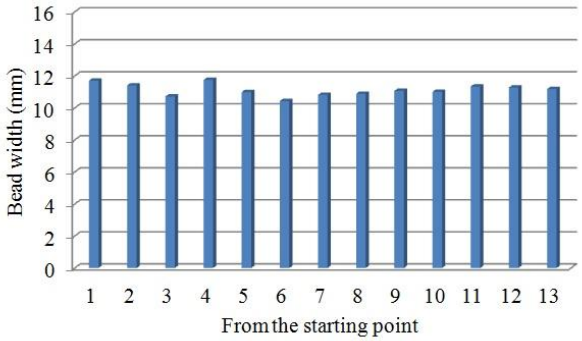

(c)

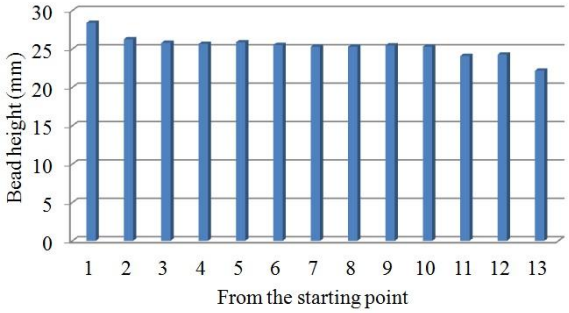

(d)

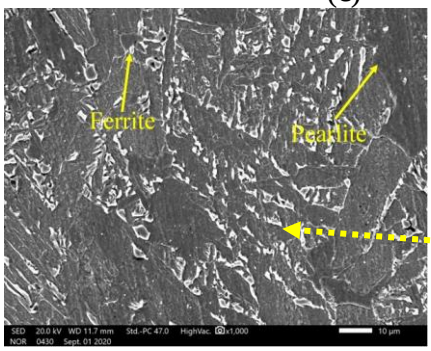

(e)

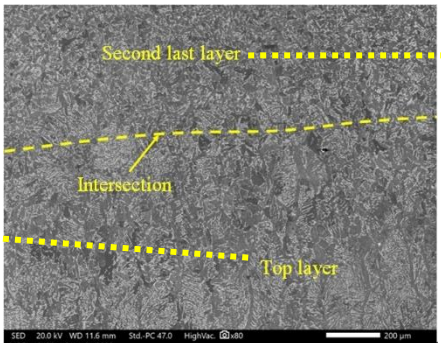

(f)

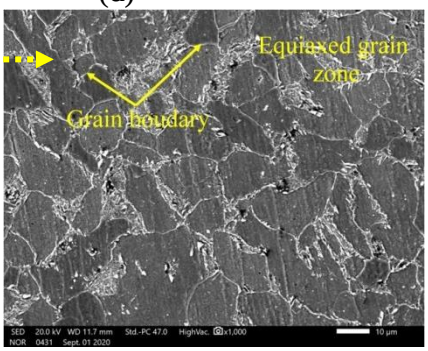

(g)

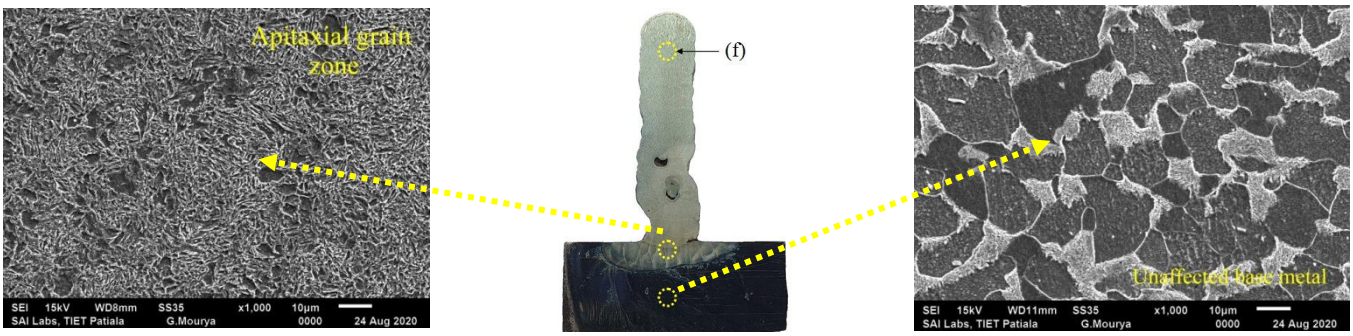

(h) (i) (j)

Figure 4.23 Metal deposition of semi-cylindrical profile: (a) material deposition of cylindrical profile, (b) wireframe of 3D measured material deposition, (c) layer height variation, (d) bead width variation, (e) SEM image of metal deposition zone at top layer, (f) SEM image of metal deposition zone at intersection of two layers, (g) SEM image of metal deposition zone at second last layer, (h) SEM image of HAZ, (i) cross section of metal deposited specimen and (j) SEM image of base metal

The stacking of the beads for the double semi-cylindrical profile is shown in Fig. 4.24(a). The start point of the deposition is indicated in the figure and the welding torch rotates in the clockwise direction looking from the top. The 3D wireframe model of the deposited profile developed from measured values using CMM is depicted in Fig. 4.24(b). The average radius of the double semi-cylindrical deposited bead was 40 mm. The variation in total layer height and bead width are shown in Fig. 4.24(c) and (d), respectively. The average heat input rate for voltage of 20 V, current of 140 A and for average deposition speed of 6.6 mm/s was 424.24 J/mm. It has been observed from Fig. 4.24(c) and (d), that reasonably better consistencies in layer height and bead width, respectively were obtained with an average layer height of 25.8 mm and bead width of 11.8 mm. The scanning electron micrograph of the deposited zone at the interface between two layers is shown in Fig. 4.24(f). Figure 4.24(e) and (g) show the SEM image of the top and bottom layer, respectively of the interface zone as shown in Fig. 4.24(f). The cut section of the specimen for the double semi-cylindrical layer deposition is shown in Fig. 4.24(i). In this figure, the interface of two layers, heat affected zone (HAZ) and the base metal are properly marked. Figure 4.24(h) and (j) illustrate the SEM image of the HAZ and the base metal, respectively.

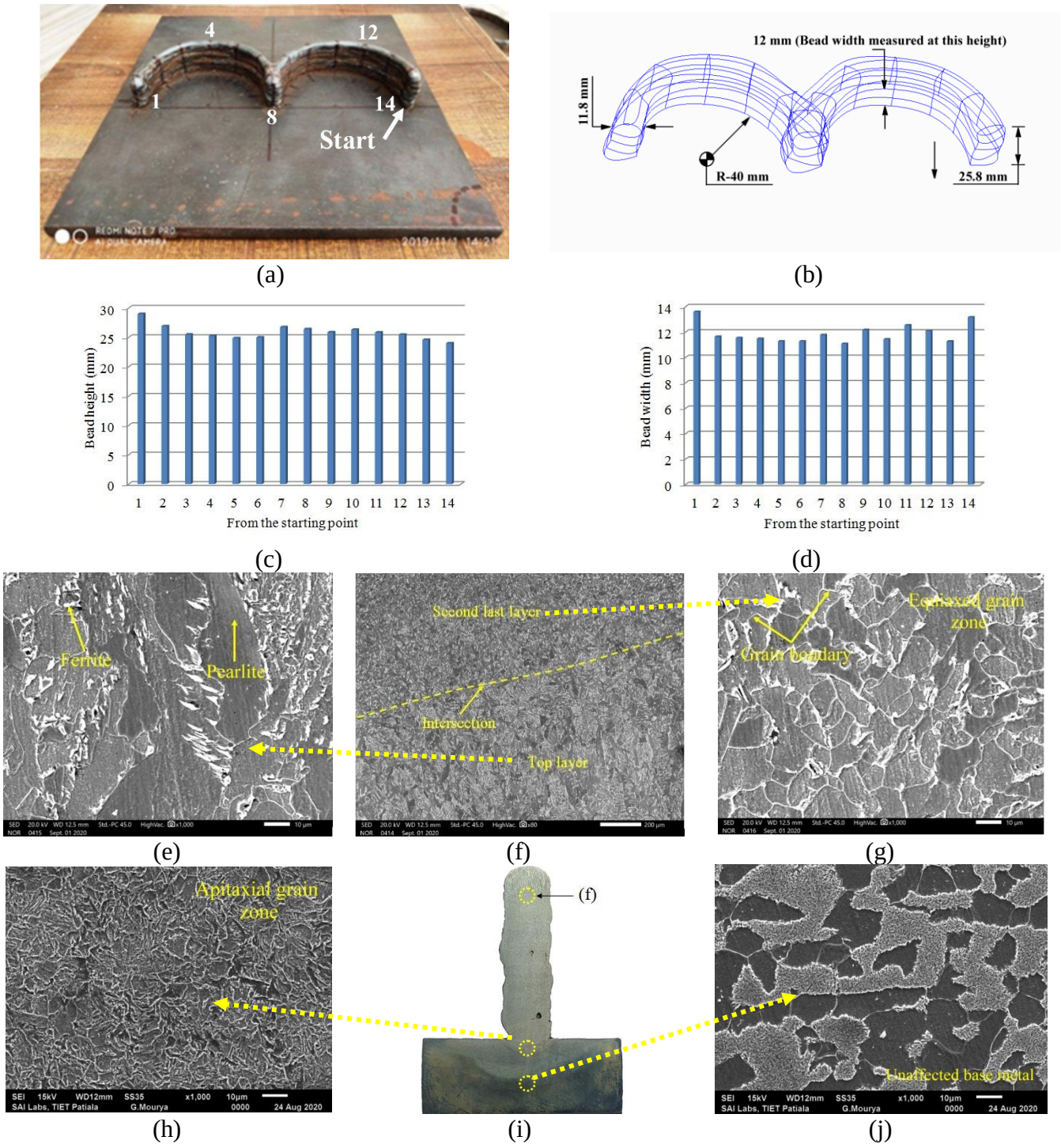

Figure 4.24 Metal deposition of double semi-cylindrical profile: (a) semi-cylindrical profile, (b) wireframe of 3D measured material deposition, (c) layer height variation, (d) bead width variation, (e) SEM image of metal deposition zone at top layer, (f) SEM image of metal deposition zone at intersection of two layers, (g) SEM image of metal deposition zone at second last layer, (h) SEM image of HAZ, (i) cross section of specimen and (j) SEM image of base metal

Figure 4.25(a) illustrated multi-layer deposition for double V-profile. The dimensions of the deposited profile were measured by CMM and the 3D wireframe model based on the measured values of the deposited profile is illustrated in Fig. 4.25(b). The length and angle of the V-profile deposition were 160 mm and 60º, respectively. The variation in total layer height and bead width are depicted in Fig. 4.25(c) and (d), respectively. The average heat input rate at average deposition speed of 6.5 mm/s was 430.6 J/mm. It had been observed from Fig. 4.25(c) and (d), that reasonably better consistencies in layer height and bead width, respectively were obtained with an average layer height of 25.7 mm and bead width of 11.9 mm.

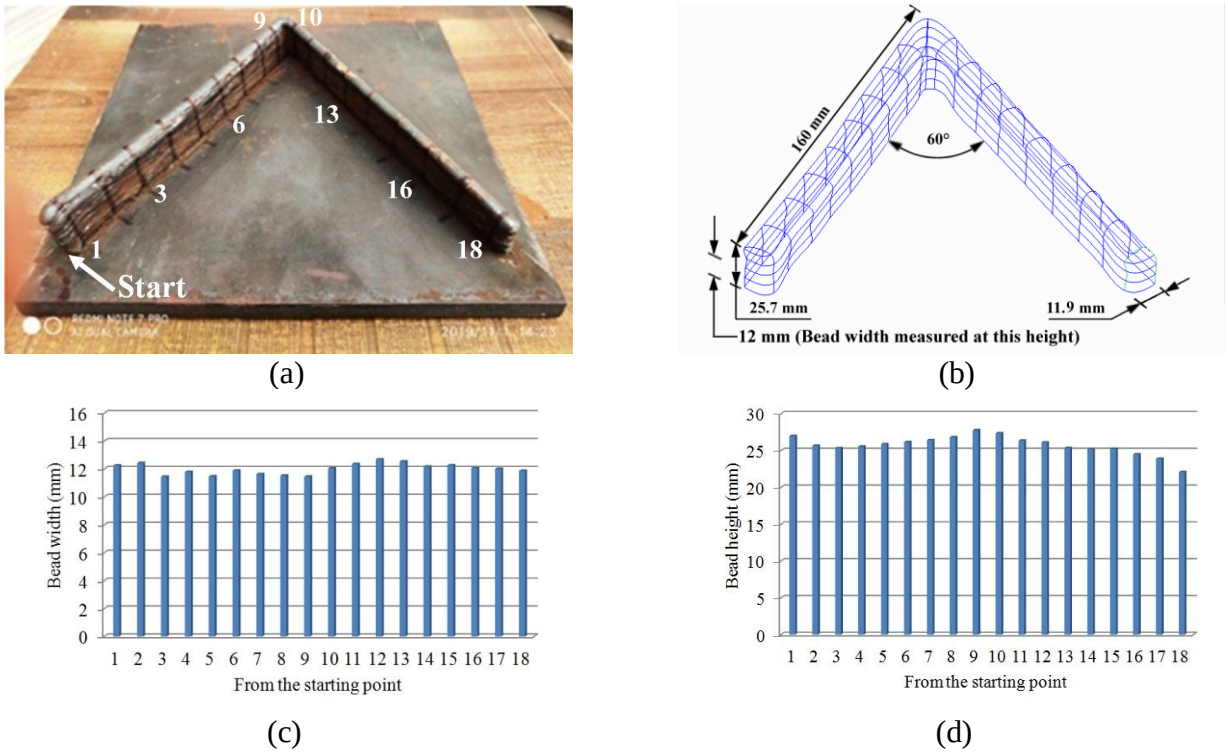

Figure 4.25 Metal deposition of V-profile. (a) material deposition of cylindrical profile, (b) wireframe of 3D measured material deposition, (c) layer height variation and (d) bead width variation

Figure 4.26(a) shows variation of micro-hardness in different zones for different deposited profiles. It was observed in all profiles that micro-hardness was maximum

(192.64–210.29 VHN) in the heat affected zone; micro-hardness of the metal deposition (151.91–186.81 VHN) was less than base metal (158.04–188.1 VHN) as well as HAZ. The best-fit third-order polynomial curves for micro-hardness are shown in Fig. 4.26(b).

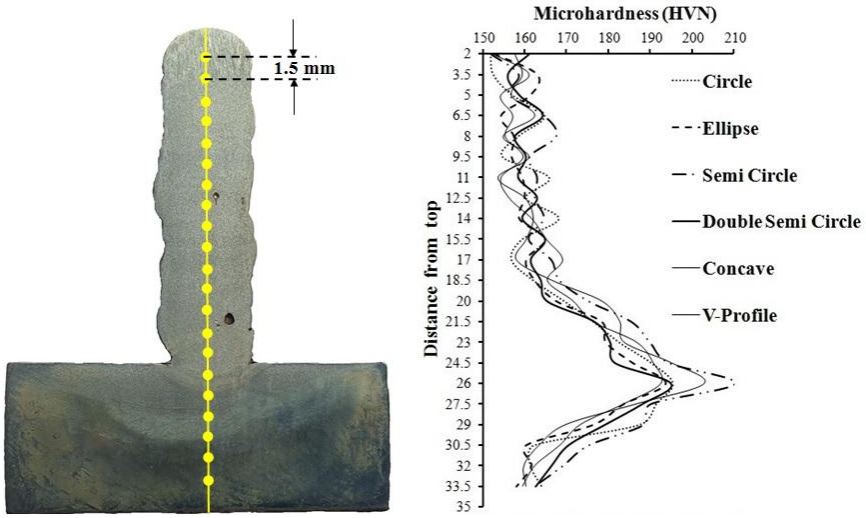

(a)

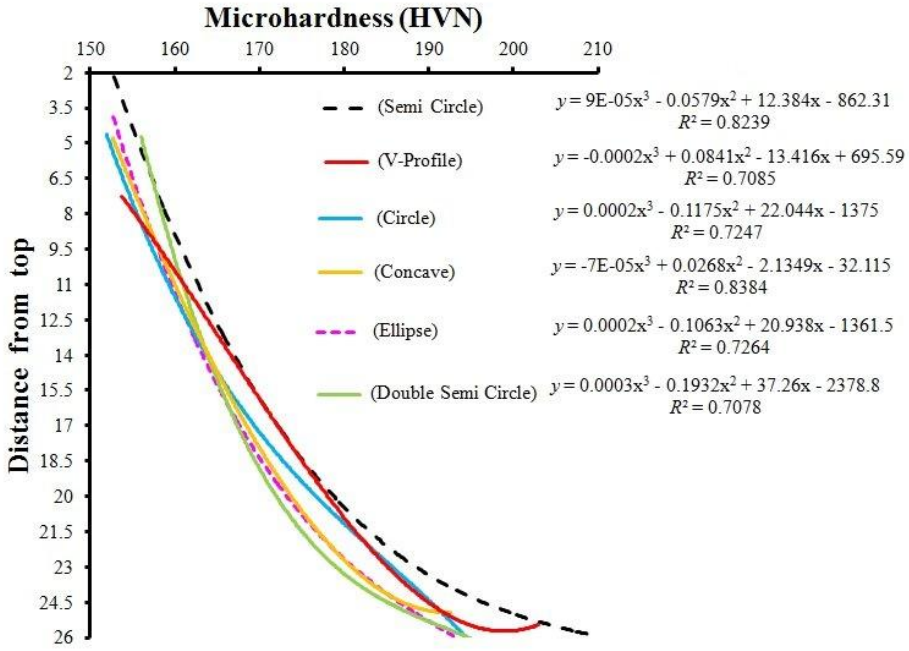

(b)

Figure 4.26 (a) Micro-hardness of different profiles (circle, ellipse, semi-circle, double semi-circle, concave and V-profile) and (b) best-fit third-order polynomial curves for micro-hardness

The microstructure of the deposited wall was significantly influenced by various factors such as cooling rate variation, constituents present in base metal as well as filler wire and direction of heat flow. Two different structures i.e., ferrite (α-iron) and pearlite (α + Fe3C) are clearly indicated in Fig. (4.20(e), 4.21(e), 4.22(e), 4.23(e), 4.24(e), 4.27(b)). Equiaxed grain and epitaxial grain are indicated in Fig. (4.20(g), 4.21(g), 4.22(g), 4.23(g), 4.24(g), 4.27(d)) and Fig. (4.20(i), 4.21(h), 4.22(h), 4.23(h), 4.24(h), 4.27(f)), respectively. Ferrite phase was observed as bright colour whereas pearlite phase as dark colour. Adjacent to the HAZ, the influence of heating was not sufficient for re-crystallization and consequently, base metal was unaffected. Micro-porosity was observed for cylindrical deposited samples and is indicated in Fig. 4.20(i). Porosity may be the cause of mechanical failure of the joint.

Multirun deposition has two distinct zones i.e., columnar and transformed zones as shown in Fig. 4.27(a). The transformed zone represented the part of the previous layer which was heated above the upper critical temperature (910˚C) during the deposition of consecutive layers [Nadkarni, 1998]. Columnar structures in the transformed zone were changed to equi-axed grains with different sizes. The transformed zone further has two distinct zones i.e., coarse grained and fine-grained zone. Microstructure image of the deposited zone at the interface between two layers is illustrated in Fig. 4.27(c). Figure 4.27(b) and (d) show the SEM image of the top and bottom layer, respectively of the interface zone as shown in Fig. 4.27(c). The locations of measurements used in SEM and EDX have been encircled on macrograph indicated by letter f, depicted in Fig. 4.27(g). The EDX spectrum for V-profile is shown in Fig. 4.27(e). The EDX spectrum revealed that Si and Mn along with Fe were present in deposited specimens. The cross section of the specimen for the V-profile layer deposition is illustrated in Fig. Fig. 4.27(g). In this figure, the interface of two layers, heat affected zone (HAZ) and the base metal are properly marked. Figure Fig. 4.27(f) and (h) show the SEM image of the HAZ and the base metal, respectively. SEM images clearly revealed that the grain size was gradually coarsened along the direction of deposition as shown in Fig. 4.20−4.25(e–h). This was due to the conduction mode of the entire heat transfer from weld. Therefore, heat transfer was restricted due to the narrow path on the vertical deposited specimen. Micro-hardness results as shown in Fig. 4.26(a) also support that the microstructure is relatively finer at

the bottom layer due to the fact of faster cooling rate, as a large part of heat produced dissipates to the substrate rapidly. Faster cooling rate helps to the transformation of polygonal ferrite into acicular ferrite near the edges as well as at the interface of two layers. Microhardness values were comparatively higher at HAZ than the base metal and different deposited layers due to the presence of bainite and martensite structures.

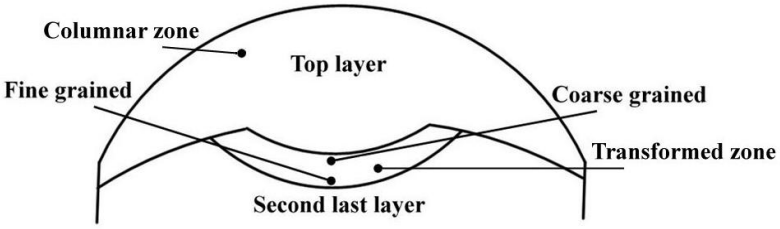

(a)

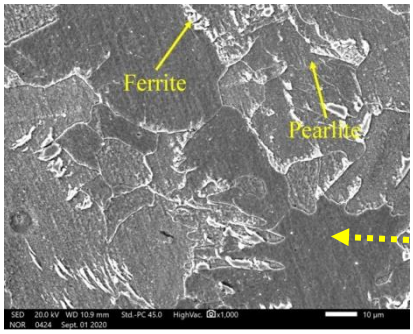

(b)

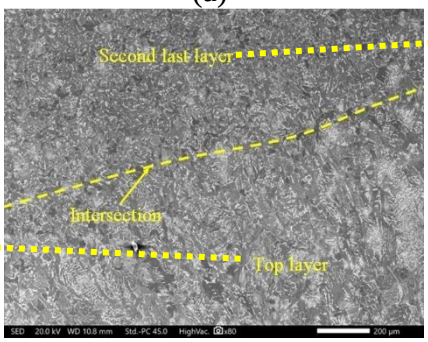

(c)

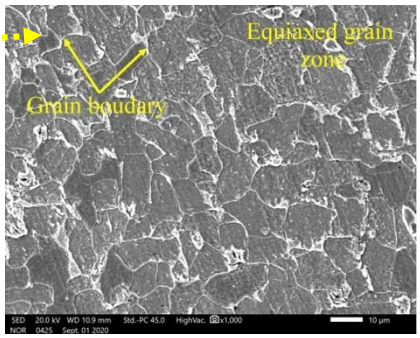

(d)

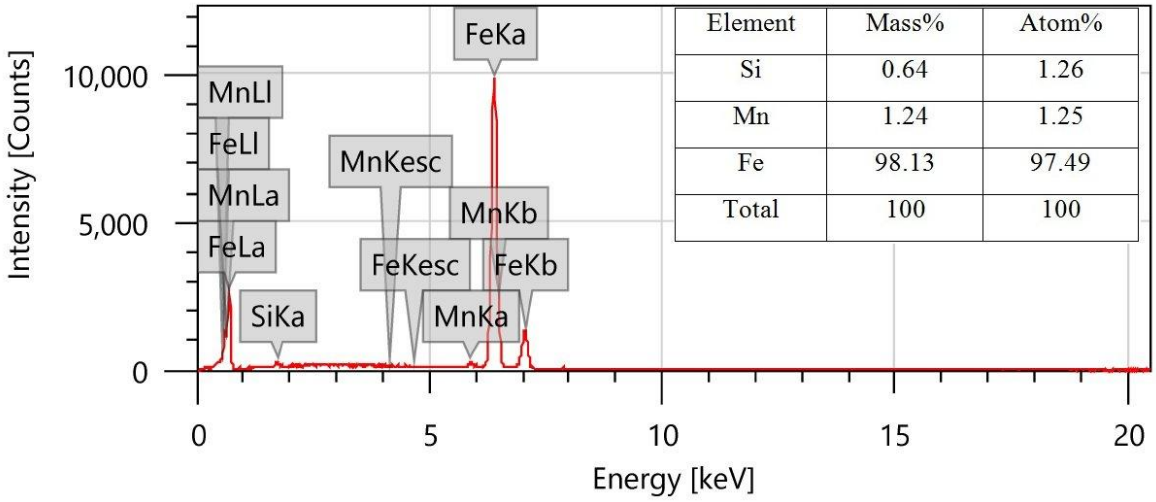

Element	Mass%	Atom%
Si	0.64	1.26
Mn	1.24	1.25
Fe	98.13	97.49
Total	100	100

(e)

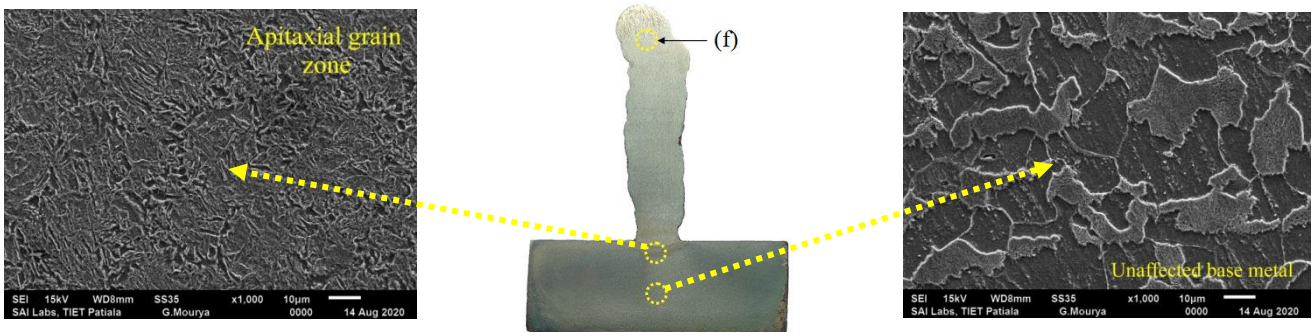

(f) (g) (h)

Figure 4.27 (a) Top layer and its vicinity, (b) SEM image of metal deposition zone at top layer, (c) SEM image of metal deposition zone at intersection of two layers, (d) SEM image of metal deposition zone at second last layer, (e) EDX spectrum showing peaks of elemental composition in deposited specimen, (f) SEM image of HAZ, (g) cross section of metal deposited specimen and (h) SEM image of base metal for metal deposition of V-profile

4.4 Multi-Layer Bead Deposition with Different Build Strategies

In this section, the automatic bi-directional GMAW setup as shown in Fig. 3.2(c) (refer Chapter-3) was used for depositing 3D components with different build strategies. Developed setup comprises of stepper motors, carriage, transmission system, guide ways and an Arduino UNO based control system. The control system was responsible for starting/ending of arc, controlling the speed of stepper motors, consequently welding speed and precision of given trajectory during metal deposition. The substrate remained stationary while the welding torch provided the necessary motion to deposit metallic parts. Electrode wire (ER70S-6) and low carbon steel having thickness of 12 mm were chosen as substrate to deposit 3D parts. The electrode wire of 1.2 mm diameter was chosen for welding. The welding gun, attached with the fabricated setup of a Tornado MIG350 GMAW machine (Ador, Bangalore, India) with maximum welding current rating of 350 A at 60% duty cycle was used for deposition purpose with 100% argon as a shielding gas. Five different path-strategies i.e., spiral-in (circular and square), raster (Square, diagonal and circular) (Fig. 4.28) were adopted to perform experiments by maintaining constant welding current of 140 A (for positive slopes) and 120 A (for negative slopes), voltage 22 V and gas flow rate 16 L/min. First, 10 layers were deposited for building positive slope and remaining 12 layers for negative slope to achieve the total height of 50 mm in all specimens as shown in Fig. 4.29. After depositing each layer, the

workpiece remained idle for 10 minutes with the aim of cooling the deposited layers to maintain the dimensional accuracy and to avoid overheating. The gap between the centres of two consecutive beads i.e., bead offset is a significant process variable, which defines the overlapping of beads and thus, it reveals the layer's surface quality. The bead offset distance was kept constant of 1 mm for all deposition-strategies. The welding torch was raised up according to the thickness of the previous deposited layer for depositing new layers.

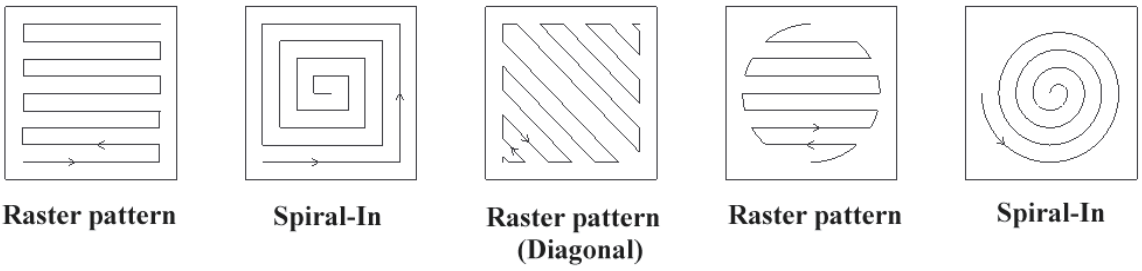

Figure 4.28 Different metal deposition patterns

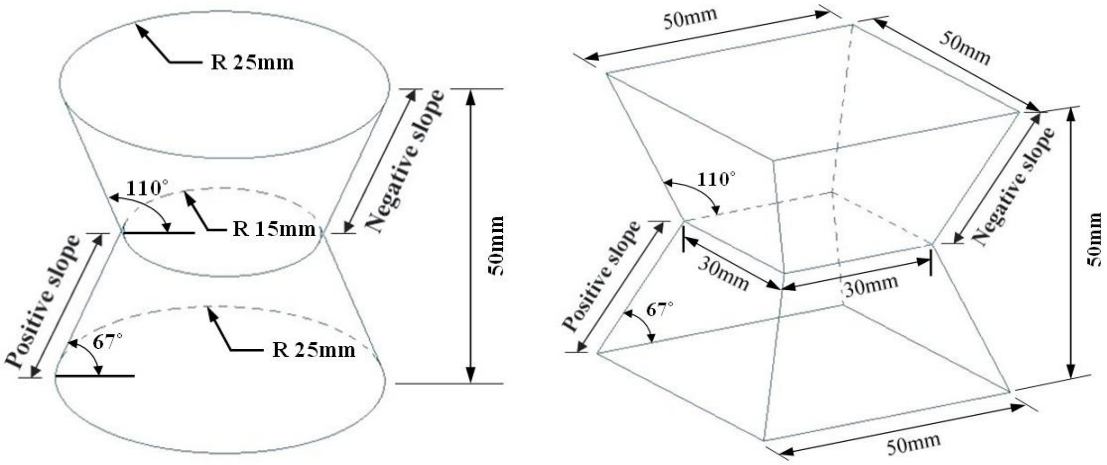

(a) (b)

Figure 4.29 Fabrication of components using negative and positive slops for: (a) circular object and (b) square object

4.4.1 Chemical Composition of Workpiece and Sample Preparation

The chemical composition of the substrate, material of electrode wire obtained after optical emission spectroscopy analysis (Make-Foundry Master by WAS, Germany) and other related details are documented in Table 4.7. After the dry run, the machine was

calibrated with 5 certified reference materials. A spark was produced in the shielding of argon gas between the tungsten electrode and the workpiece to produce burn spots on the specimen.

Table 4.7 Material composition in the present study

	Material	Compositions measured (wt%)	Dimensions
Workpiece	Mild steel	C: 0.154–0.158%, Si: 0.234–0.247%, Mn: 0.711–0.780%, P: 0.0302–0.0561%, S: 0.0274–0.0276%, Fe: Balance	150 mm × 150 mm × 12 mm
Welding wire	Carbon steel (ER70S-6)	C: 0.06–0.15, Si: 0.80–1.15, Mn: 1.40–1.85, P: 0.025 max, S: 0.035 max, Cu: 0.50 max: Fe: balance	Diameter 1.2 mm

After the bead deposition, the specimens were cut with wire electric discharge machining (WEDM) from the deposited samples for tensile and bending testing according to the arrangement shown in Fig. 4.30(a, b). The geometry of the tensile and bending specimens prepared according to the ASTM E8/E8M-15a and ASTM A290-14 standard and geometries are shown in Fig. 4.30(c). The location of the test specimens of different strategies after slicing is presented in Fig. 4.31. Samples for measuring the microhardness of the deposited parts were prepared using standard procedure including grinding and polishing with different grades of emery papers. Measurement of microhardness was carried out by Vickers hardness tester applying 500 gm force of load with 20 seconds of dwell time. The scanning electron microscopy (SEM) (JSM-IT500, JEOL) was used for metallographic examination of the deposited specimens and different grades (220, 320,400, 600, 800, 1000, 1500, 2000 and 2500) of emery paper were used to polish the specimens which were subsequently etched with nital (5 ml nitric acid and 95 ml ethanol).

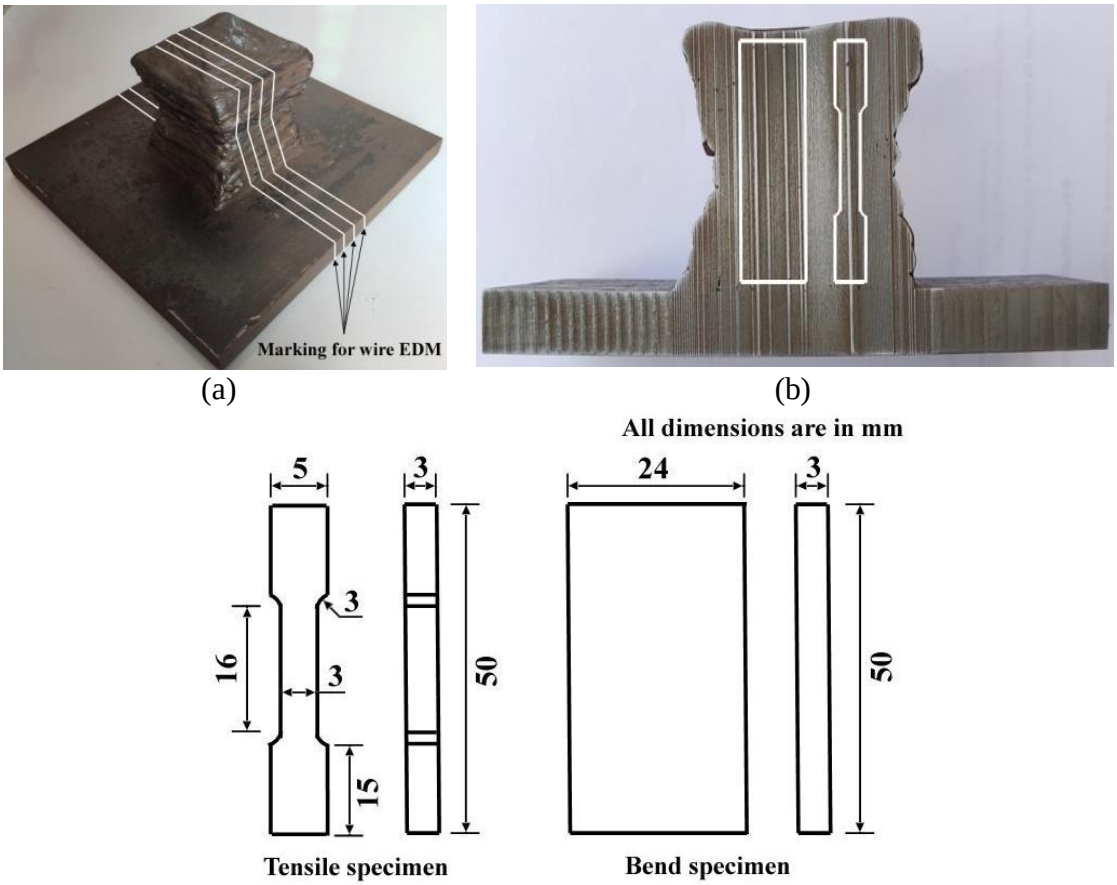

Figure 4.30 (a) Marked specimen for cutting, (b) location of specimens for cutting and (c) test specimens geometry

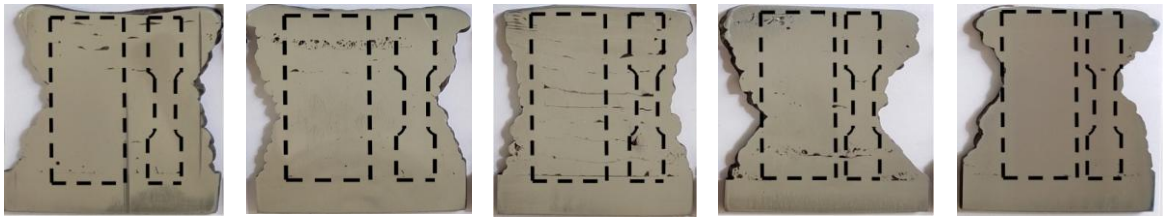

Raster (Square) | Raster diagonal (Square) | Spiral-In (Square) | Spiral-In (Circular) | Raster linear (Circular)

Figure 4.31 Location of tensile and flexural specimens for different strategies

4.4.2 Testing of Deposited Specimens

The influence of five different strategies have been studied to investigate the tensile strength, bending strength and microhardness on multi beads deposited metal parts which

are depicted in Fig. 4.32. Actual deposited specimens with different strategies and their wire frames are shown in Fig. 4.32(a, c, e, g, i) and Fig. 4.32(b, d, f, h, j), respectively. The dimensional accuracy of the deposited parts was measured using a coordinate measuring machine and the wire frames of different strategies are presented.

Raster (Square)

(a) Actual specimen

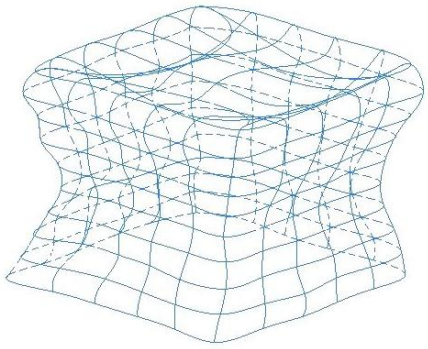

(b) Wire frame

Raster diagonal (Square)

(c) Actual specimen

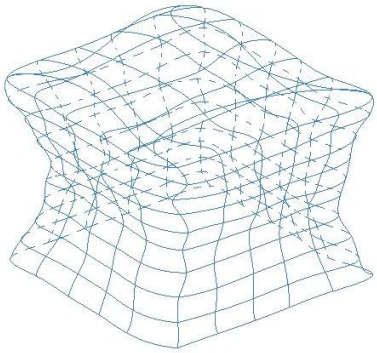

(d) Wire frame

Spiral-In (Square)

(e) Actual specimen

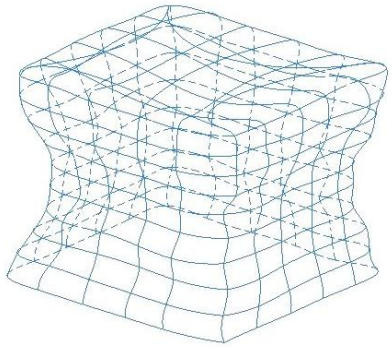

(f) Wire frame

Spiral-In (Circular)

(g) Actual specimen

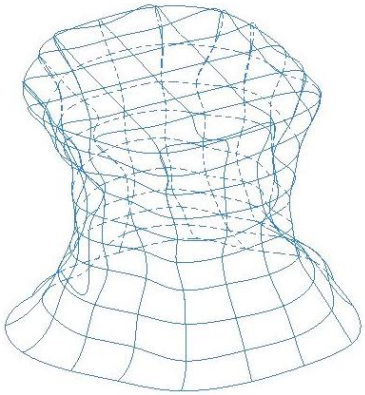

(h) Wire frame

Raster linear (Circular)

(i) Actual specimen

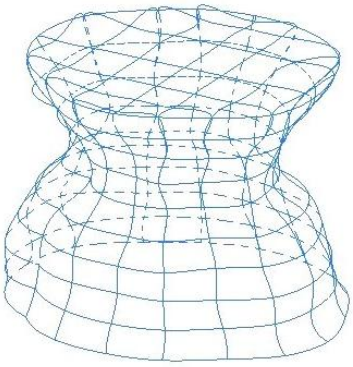

(j) Wire frame

Figure 4.32 Different strategies used for deposition along with actual specimens and their wire frames raster (square) (a-b), raster diagonal (square) (c-d), spiral-in (square) (e-f), spiral-in (circular) (g-h) and raster linear (circular) (i-j)

The accuracy/effectiveness of the fabricated setup was validated by depositing three dimensional specimens with different strategies and measuring the uniformity in the deposited specimens in terms of the dimensional accuracy, positive and negative slope variation. Staircase effects were observed during metal deposition in raster (Square) and raster diagonal (Square) pattern as shown in Fig. 4.32(a, c). The desired dimensions of the deposited specimen with different strategies are shown in Fig. 4.29(a, b). Theoretically the dimensions of the deposited specimen at the base, middle and top should be 50mm × 50mm, 30mm × 30mm and 50mm × 50mm (Fig. 4.29(b)) in comparison of measured specimens of 55.67 × 55.05, 43.91 × 44.19 and 51.78 × 53.69 in raster (square) strategy, respectively. The expected positive and negative slope angles

were 67˚ and 110˚ (Fig. 4.29(b)) in comparison of the measured specimens of 76.76˚ and 103.24˚. Similarly, actual measured values in spiral-In (square) strategy were 55.34 × 55.08, 43.46 × 43.96 and 52.83 × 53.49. The values of measured angle for spiral-In (square) strategy were 76.63˚ and 103.37˚. The measured dimensions in comparison to the theoretical dimension in raster diagonal (square) strategy were 53.44 × 53.89, 42.02 × 42.25 and 54.04 × 53.03. However, the measured specimen was close to the expected values, i.e., measured orientation at 77.11˚ and 102.89˚ in comparison with expected orientation at 67˚ and 110˚. In the same manner, in comparison to the expected dimensions in spiral-In (circular) strategy (Fig. 4.29(a)), the measured dimensions were 54.41 × 55.29, 39.24 × 32.44 and 53.54 × 45.12. The measured orientations were 73.13˚ and 106.87˚ in comparison with the expected orientations at 67˚ and 110˚. Similarly, actual measured values in the raster linear (circular) strategy were 54.61 × 54.50, 38.60 × 34.83 and 54.05 × 50.77. The expected positive and negative slope angles in comparison of the measured specimen were 72.26˚ and 107.74˚.

From the deposited specimens with different deposition strategies, the wire frames were obtained using CMM in order to assess the dimensional accuracy in comparison to the theoretical/ actual dimensions. It may be noted that a reasonably good dimensional accuracy of the deposited specimens has been achieved while building positive and negative slopes.

4.4.2.1 Analysis of Tensile and Bending Strength

Fractured specimens in tensile testing are shown in Fig. 4.33(a) whereas the specimens after bending are shown in Fig. 4.33(b). The results of the tensile strength and maximum bending load of all five strategies are provided in Fig. 4.34(a) and Fig. 4.34(b), respectively. Figure 4.34(a) shows the influence of different strategies on the tensile strength wherein *x*-axis shows the different profiles and *y*-axis shows the tensile stress. Figure 4.34(a) revealed that the tensile strength of raster diagonal (Square) (460 MPa) and raster linear (circular) (464 MPa) significantly high as compared to the remaining three strategies. The percentage elongation of tensile samples of the deposited specimens in different strategies such as raster (square), raster diagonal (square), spiral-In (square),

spiral-In (circular) and raster linear (circular) were 18.75%, 12.5%, 9.37%, 7.81% and 9.37%, respectively. It can be observed from the tensile fractured samples as shown in Fig. 4.33(a) that all the samples present clear lamellar tearing and neck formation in fractural locations. Higher values of tensile strength in raster diagonal (Square) and raster linear (circular) show the evidence of development of more heat in the fusion zone owing to the long profile path during deposition. The plastic deformation of a deposited specimen can be evaluated using the bend test. The bending properties are also a measurement of the material plasticity index. Figure 4.34(b) revealed that maximum load during bending of raster diagonal (Square) (3960 N) and raster linear (circular) (3940 N) significantly high as compared to the remaining three strategies. In the 3-point bend test of deposited specimens, spiral-In (square) and spiral-In (circular) specimens failed to bend. In contrast, both deposited specimens broke during the test which might be due to micro-voids and micro cracks developed during uneven solidification in the deposition.

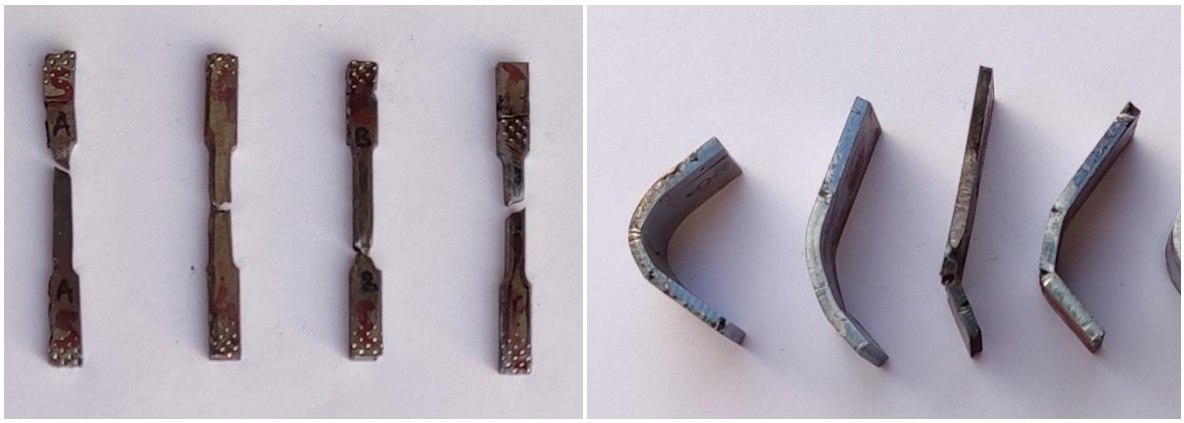

(a) (b)

Figure 4.33 (a) Fractured tensile specimens and (b) fractured bending specimens

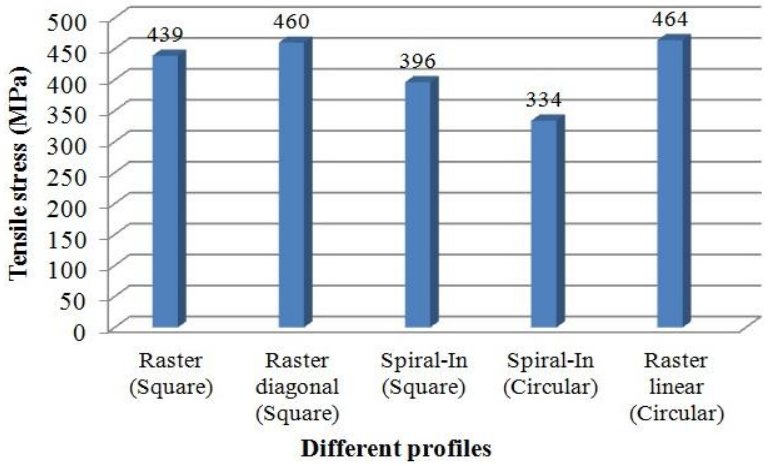

(a)

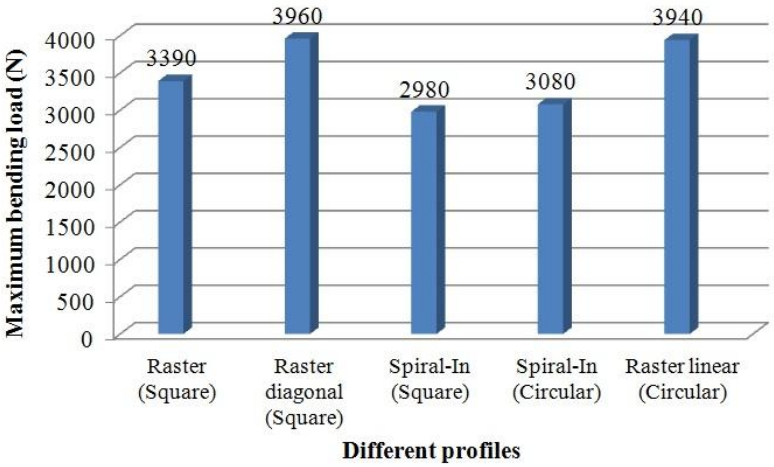

(b)

Figure 4.34 Comparison of tensile stress and maximum bending load during different patterns

4.4.2.2 Analysis of Microhardness

The microhardness of specimens for metal deposition using different strategies is shown in Fig. 4.35. The microhardness measurements along the centre line from top to bottom are taken between two indentations each of 1.5 mm apart as shown in Fig. 4.35(a). The microhardness values for the deposited metal layers in all five strategies are given in Fig. 4.35(b). The comparison of time taken to deposit one layer for all five strategies is depicted in Fig. 4.35(c). Figure 4.35(c) clearly indicates that the time taken by the spiral-in (circular) and raster linear (circular) is relatively less followed by raster diagonal (square), spiral-in (Square) and raster (square), respectively. Less time consumption

means that low heat input is provided during deposition and this results in lower microhardness value.

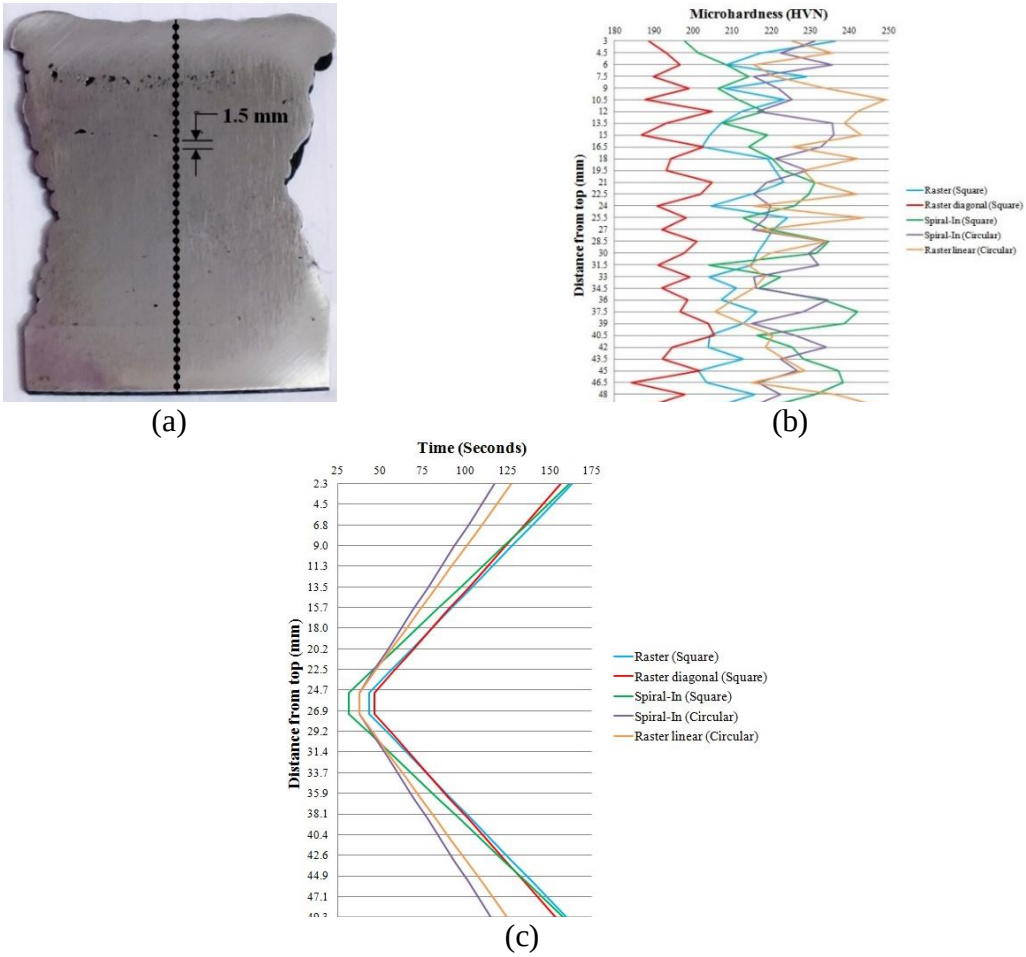

Figure 4.35 Microhardness results: (a) location of indentations on deposited specimen, (b) microhardness values of different patterns and (c) comparison of time taken for different build strategies

4.4.2.3 Microstructural Analysis

The scanning electron microscopy was carried out to gain more insight into the microstructural behaviour of the deposited specimens using different multi bead deposition strategies. Microstructural analysis of all specimens deposited using different multi-beads strategies are depicted in Fig 4.36. Figure 4.36 illustrates the interfaces of two beads, zoomed view of upper layer and lower layer at top position of all deposited specimens in the given table from left to right. SEM images revealed the clear demarcation between the two consecutive layers. In order to make it clearer, upper layer and lower layer are differentiated by dotted lines and are indicated as interfaces as shown in Fig. 4.36(b) in all strategies. SEM images clearly revealed that due to heat

accumulation of the next deposited layer, relatively fine grains were produced as compared to previous fully grown grains. It was also observed from SEM images of raster (square) that relatively more heat input was induced owing to the increase in surface area in the process of formation of negative slope. Consequently, comparatively fine grains were produced and relatively, high tensile strength was observed. More consistency in grain growth and no solidification micro cracks were observed in the SEM images owing to uniform heat input during deposition. However, micro-porosity was observed in the lower layer in case of raster (square) deposition as shown in Fig. 4.36(c). Distribution and arrangement of grains help to define the various types of microstructures which subsequently define mechanical properties. Ferrite (α-iron) and pearlite (α + Fe3C) structures were observed in SEM images as depicted in Fig. 4.36(c). Owing to the sufficient heat input, equiaxed grain zone was observed in the top layer. Relatively fine grain structure is formed in the upper layer which may be due to the higher solidification rate in the deposited layer. The rate of cooling of the fusion zone was enhanced by radiation to the atmosphere. The grain boundaries were clearly revealed in the fine grain microstructure as shown in Fig. 4.36(a).

Raster (Square)

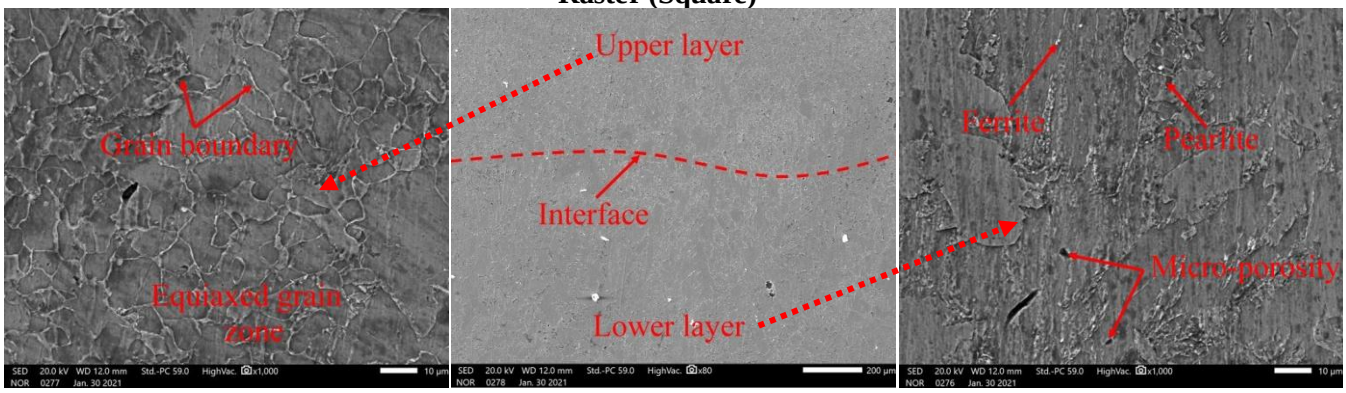

(a) Upper layer (b) Interface between two layers (c) Lower layer

Raster diagonal (Square)

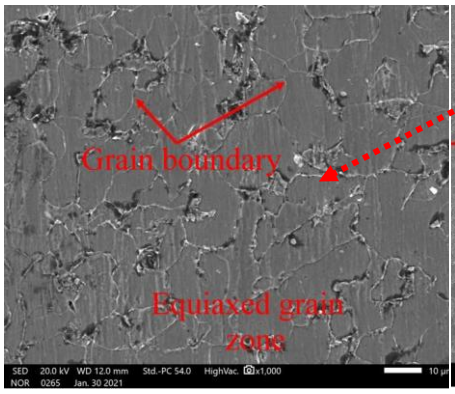

(d) Upper layer

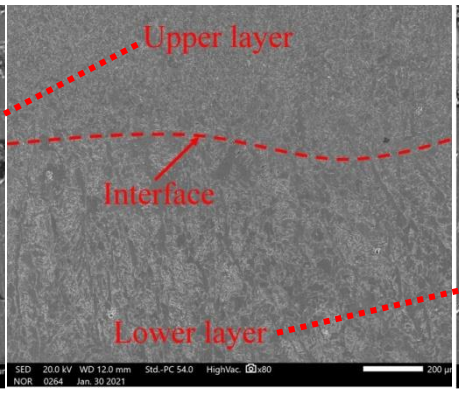

(e) Interface between two layers

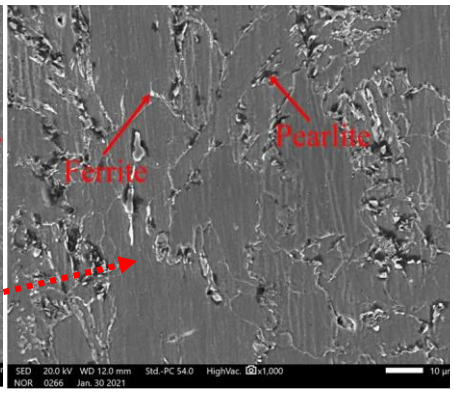

(f) Lower layer

Spiral-In (Square)

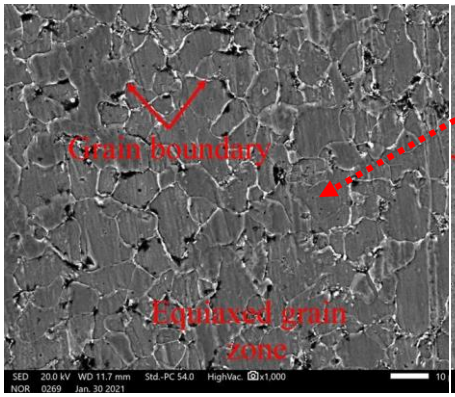

(g) Upper layer

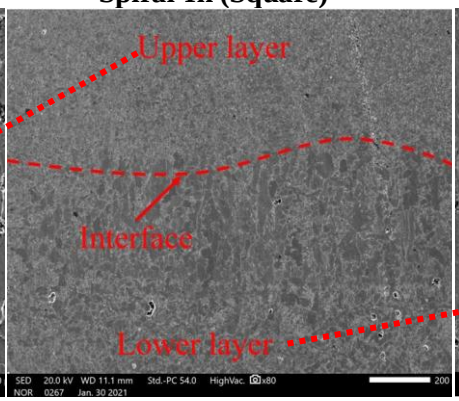

(h) Interface between two layers

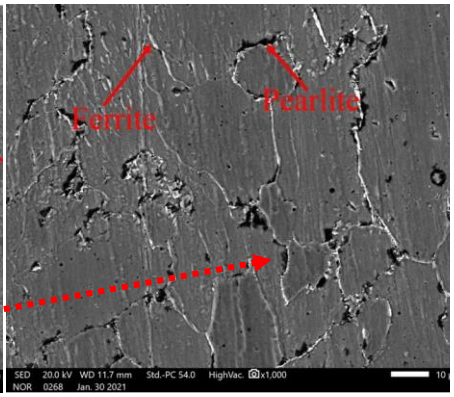

(i) Lower layer

Spiral-In (Circular)

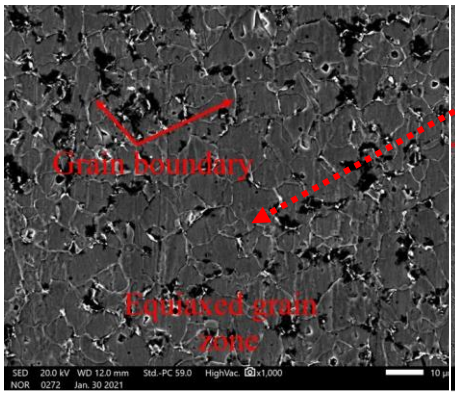

(j) Upper layer

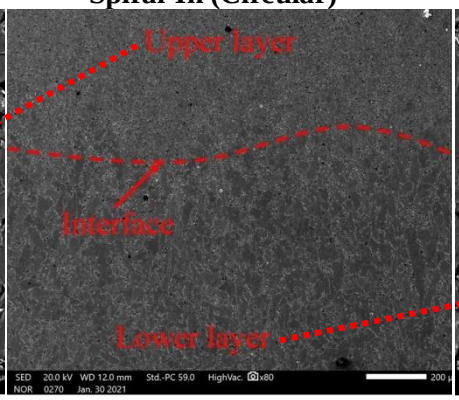

(k) Interface between two layers

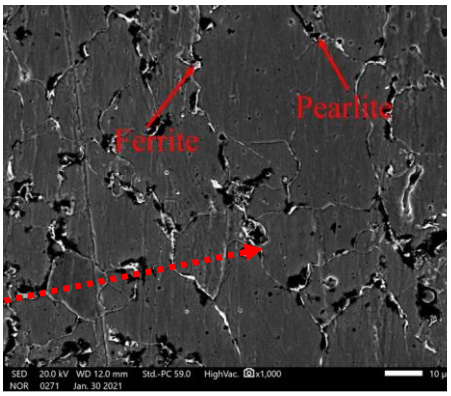

(l) Lower layer

Raster linear (Circular)

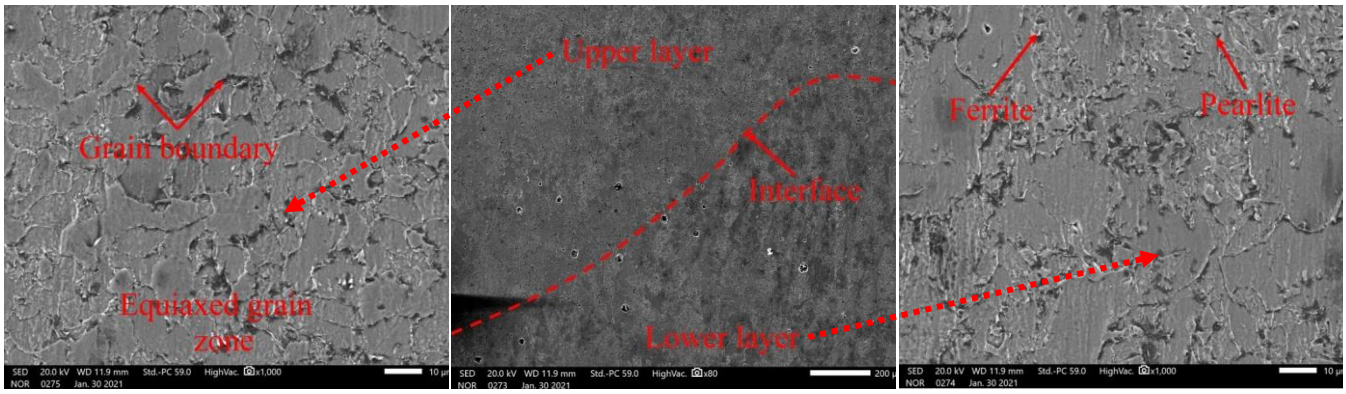

(m) Upper layer (n) Interface between two layers (o) Lower layer

Figure 4.36 SEM images of metal deposition zone at upper layer**,** interface of two layers and lower layer raster (square) (a-c), raster diagonal (square) (d-f), spiral-in (square) (g-i), spiral-in (circular) (j-l) and raster linear (circular) (m-o)

The results of all the weld deposition strategies i.e., raster (square), raster diagonal (square), spiral-in (square), spiral-in (circular) and raster linear (circular) using semi-automated movement setup for GMAW are presented in this section. During deposition, it was observed that welding conditions had significant influence on the accuracy of the bead geometry of the next layer. It was noticed during depositing negative slopes that the welding current and travelling speed had remarkable influence on the bead geometry. The weld performed at faster speed results in low heat input and comparatively faster solidification rate. Faster cooling rate generally leads to formation of fine grain structure and consequently yields higher mechanical strength. With the increase in temperature, weld puddles flow in the downward direction and creates inaccurate structure-formation. During deposition of all strategies, it was observed that positive slopes were framed with extreme consistency however, while forming negative slopes, more difficulty was faced with the same welding parameters and it induced excessive heat at fusion zones which led to inconsistency of forming inclination. In order to obtain the accuracy of bead deposition, welding speed was increased and consequently, reduction in bead height and addition of two more layers (12 layers) to achieve the same height of positive slopes were required.

Deposition with different weld bead path profiles and vertical layer deposition for different open and closed profiles were performed using bi-directional automatic

movement setup for GMAW and were presented in this chapter. Subsequently to enhance the versatility of the fabricated setup, three-dimensional components having negative and positive slopes were deposited using different path strategies. After deposition, specimens were prepared for testing purposes using standard procedure i.e., grinding and polishing to investigate the mechanical as well as microstructural properties. To gain more insight into the microstructural and mechanical behaviour of the welded joints, welding of two dissimilar metals i.e., austenitic AISI 304 and 316 stainless steels with duplex 2205 in the presence of three different activated fluxes i.e., SiO_2, TiO_2 and CrO_3 would be discussed in detail in Chapter-5.

Chapter 5

Joining of Dissimilar Stainless Steels using Activated Fluxes

Dissimilar metal joining has various engineering applications in nuclear power plant, chemical plant, food processing and automobile industries owing to the reduction in weight and it mitigates the production cost without compromising the mechanical properties. But, joining dissimilar steels is quite difficult. Joining depends upon the selection of process variables, shielding gas, filler material *etc*. for the variations in mechanical, thermal and chemical properties of the workpiece materials.

In the current chapter, the bead geometry is varied and the penetration depth is enhanced using an indigenously designed and fabricated bi-directional semi-automatic movement setup for GMAW. Three different grades of steel austenitic AISI 304/ 316 and duplex 2205 were welded in the presence of three activated fluxes (SiO_2, TiO_2 and CrO_3) using this setup. Moreover, effect of activated fluxes, influences of welding parameters namely welding current, voltage, workpiece material, filler material and flow rate of inert gas were investigated on penetration-depth, microhardness, impact strength, tensile strength and bending strength of dissimilar steels. Dissimilar joining of AISI 304-to-AISI 2205 and 316-to-AISI 2205 was performed following Taguchi factorial design of experiment (DOE) technique. Microstructural characterization of the welded specimens was also carried out at different weld zones using scanning electron microscopy. Since joining of dissimilar metals is a quite complex and needs a proper parametric selection in order to obtain high quality welding results, this study may facilitate the industry to properly understand the effects of process parameters in joining dissimilar metals using activated flux and could be helpful to precisely select the optimum levels of process parameters.

5.1 Effect of Activated Fluxes during Welding of Dissimilar Stainless Steels

The developed setup was used to join the metallic strips of dissimilar stainless-steel grades between austenitic AISI 304/ 316 with duplex 2205. The workpiece of dimensions 100 mm × 50 mm and thickness of 5 mm was selected. The influences of welding

current, voltage, workpiece material, filler material, gas flow rate, activated flux were investigated and all these parameters were varied at three levels. The workpieces, after cutting, were ground properly at their faying surfaces. Workpiece surfaces were cleaned using acetone to remove any impurities or oxide layer on the surface. Each of the activated fluxes was properly mixed individually with acetone to make a paste and subsequently, it is coated on the workpieces before the welding. Welding, without any edge preparation of the workpiece, was carried out by attaching the weld gun on the fabricated setup using MIG 350 (Tornado, Ador Frontech) machine as depicted in Fig. 5.1(a). Figure 5.1(b) & 5.1(c) show the close views of the specimen before (showing layer of activated flux) and after welding, respectively. Argon gas was used for welding of dissimilar metals.

(a)

(b)

(c)

Figure 5.1 Automatic bi-directional movement setup: (a) fabricated GMAW setup, (b) specimen after applying activated flux and (c) welded specimen

5.2 Chemical Composition of Workpiece and Sample Preparation

The chemical compositions of the base materials obtained after optical emission spectroscopy analysis (Make-Foundry Master by WAS, Germany) are documented in Table 5.1. Initially, the machine was dry run for 45 minutes and subsequently, calibration was performed with 5 certified reference materials by taking 3 readings on each material. Argon gas helped to produce plasma while spark was created between the tungsten electrode and the workpiece. At least 3 readings were taken to take the average.

Table 5.1 Weight percentage of base metal

Sample	C	Si	Mn	P	S	Cr	Mo	Ni	Al	Co	Cu	Fe
AISI 304	0.143	0.435	1.63	0.0440	0.0248	18.8	0.249	8.02	0.0021	0.122	0.403	Bal.
AISI 316	0.005	0.290	1.55	0.0434	0.005	16.7	1.82	9.74	0.0010	0.293	0.433	Bal.
AISI 2205	0.329	0.376	0.675	0.0030	0.0260	23.3	3.70	4.19	0.0606	0.124	0.119	Bal.

After welding (according to the conditions defined in Table 5.3), the workpieces were cut and prepared into standard specimens (following ASTM E8/E8M-15a, ASTM E23-16a and ASTM E290-15a standards) for mechanical testing and metallurgical studies. Test samples, from the welded specimens, for microhardness, tensile, bending, impact test and SEM observations were prepared according to the arrangement and geometry depicted in Fig. 5.2(a) and Fig. 5.2(b), respectively. Uniaxial tension tests and bending tests were undertaken on an ultimate tensile testing machine of 50 kN capacity (Tinius Olsen Pvt. Ltd., India). The toughness test was carried out using the Charpy impact testing machine (Fine Manufacturing Industries, India, 300 J capacity). Figure 5.3(a–c) depicts the broken specimens during tensile, impact and bend test, respectively. Microhardness specimens were cut from the welded samples, ground and polished using standard procedure. The Vickers microhardness measurements were obtained by loading 500 g and with 20 s dwell time using a microhardness testing machine (Metatech Industries, Pune, India, 1000 g capacity). For the microstructural observations, the specimens were finely polished using different grades of emery papers and subsequently, diamond paste was used for mirror-like surfaces. Specimens were etched with carpenter etchant prior to scanning electron microscopy (SEM, JEOL) for metallurgical studies.

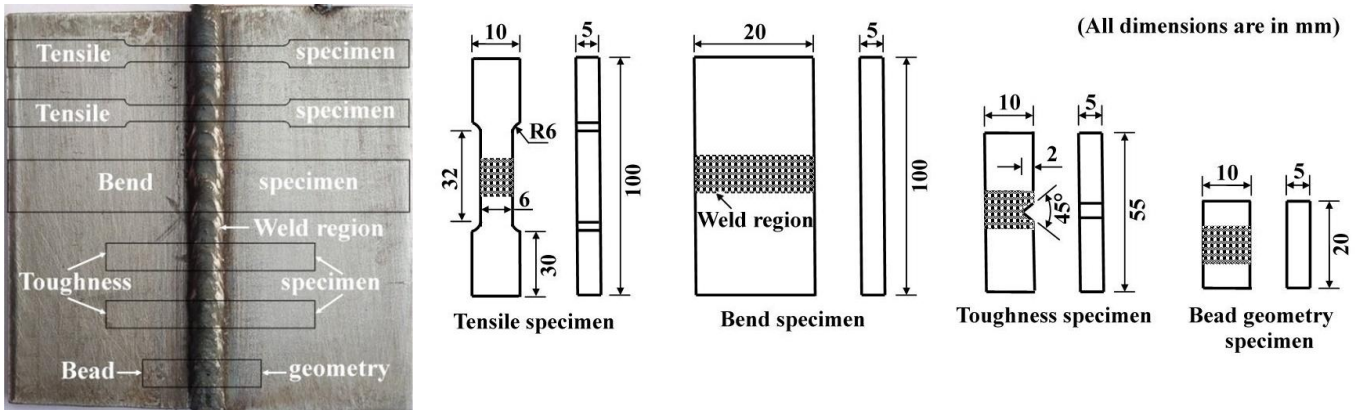

(a) (b)

Figure 5.2 (a) Marking arrangement of different test welded specimens and (b) geometry of all test specimens

(a) (b) (c)

Figure 5.3 Fractured specimens during: (a) tensile, (b) impact and (c) bend test

5.3 Selection of Orthogonal Array and Factors Assignment

For experimental work, it was decided to select L_{18} orthogonal array (OA). Fractional factorial design by Taguchi was followed for two-three mixed levels. L_{18} OA has a total 18 experimental trials i.e., degrees of freedom (DOF) are 17. The previous work and pilot

studies were considered to decide the levels of each factor. Further, each factor was varied one at a time. Eventually, all six factors were varied at selected levels for welding of AISI 304 and AISI 316 with AISI 2205 using activated fluxes as given in Table 5.2.

Table 5.2 Factors and their varied levels for each process variable chosen for joining the dissimilar metals

Sr. No.	Parameter	Symbol	Units	DOF	Level-1	Level-2	Level-3
1.	Base material	A	-	1	AISI 304-AISI 2205	AISI 316-AISI 2205	-
2.	Welding current	B	A	2	160	180	200
3.	Welding voltage	C	V	2	16	18	20
4.	Flow rate of gas	D	L/min	2	10	12	14
5.	Activated flux	E	–	2	SiO_2	TiO_2	CrO_3
6.	Filler material	F	–	2	AISI 304	AISI 316	AISI 2205

5.4 Analysis of Variance

The tensile strength, bending strength, microhardness, toughness and bead geometry were studied for all 18 combinations made of dissimilar steels i.e., austenitic AISI 304/316 and AISI 2205 stainless steels. The experiment results are tabulated in Table 5.3 along with experimental conditions. The statistical approach of analysis of variance (ANOVA) was applied to analyse the testing results. Using ANOVA, sum of squares and variance of each factor were calculated to estimate the influence of each factor in percentage and were presented in Table 5.4. Statistical analysis helps to identify the influence of each process variable on responses. It also helps to identify the contribution of prominent factors in the responses.

Table 5.3 Trial conditions of $L_{18}(3^5\text{-}2^1)$ experimental design (OA) and consequent experimental results

Mixed level Taguchi static designs

Expt. No.	Trial conditions						Experimental results			
	Weld material	Welding current	Welding voltage	Gas flow rate	Activating flux	Filler material	Tensile strength (MPa)	Bending strength (MPa)	Toughness (J)	Micro-hardness (VHN)
1	1	160	16	10	SiO_2	AISI 304	209.5	257	68.85	262.189
2	1	160	18	12	TiO_2	AISI 316	231	70.4	25.85	248.436
3	1	160	20	14	CrO_3	Duplex 2205	228	12.7	13.55	247.400
4	1	180	16	10	TiO_2	AISI 316	270.5	169	42.85	234.581
5	1	180	18	12	CrO_3	Duplex 2205	239	71.8	28.05	270.047
6	1	180	20	14	SiO_2	AISI 304	325.5	143	43.65	228.220
7	1	200	16	12	SiO_2	Duplex 2205	203	75.1	42.8	268.844
8	1	200	18	14	TiO_2	AISI 304	194.5	62.7	31.9	234.091
9	1	200	20	10	CrO_3	AISI 316	412.5	55.6	69.4	241.622
10	2	160	16	14	CrO_3	AISI 316	126.5	40.1	18.4	236.949
11	2	160	18	10	SiO_2	Duplex 2205	217.5	43.9	17.5	254.518
12	2	160	20	12	TiO_2	AISI 304	178	39.1	13.75	268.816
13	2	180	16	12	CrO_3	AISI 304	87.25	5.16	6.25	242.449
14	2	180	18	14	SiO_2	AISI 316	377.5	69.4	85.05	241.583
15	2	180	20	10	TiO_2	Duplex 2205	397	129	91.95	255.116
16	2	200	16	14	TiO_2	Duplex 2205	319	69.1	95	248.969
17	2	200	18	10	CrO_3	AISI 304	280	13.8	27.6	243.432
18	2	200	20	12	SiO_2	AISI 316	319.5	130	70.65	244.023

Table 5.4 ANOVA summary of results after joining between dissimilar steels

		Tensile strength			Bending strength			Toughness			Micro-hardness		
Source	DOF	SS	Variance	*F*-value	SS	Variance	*F*-value	SS	Variance	*F*-value	SS	Variance	*F*-value
Base material	1	7	7	0.00	7927	7927	2.71	195.0	195.0	0.24	0.0	0.0	0.00
Current	2	30375	15187	4.27	2858	1429	0.49	2963.3	1481.6	1.84	201.0	100.5	0.87
Voltage	2	34642	17321	4.87	6837	3419	1.17	654.8	327.4	0.41	7.1	3.6	0.03
Gas flow rate	2	23605	11802	3.32	8345	4173	1.43	1560.3	780.1	0.97	926.1	463.0	3.99
Activated flux	2	7159	3580	1.01	23188	11594	3.96	2617.0	1308.5	1.62	25.5	12.8	0.11
Filler material	2	18898	9449	2.66	1781	890	0.30	1354.1	677.0	0.84	827.0	413.5	3.56
Error	2	21328	3555		17558	2926		4840.8	806.8		696.3	116.1	
Total	17	136014			68494			14185.2			2683.1		

5.5 Welding and Testing of Dissimilar Stainless Steels

The joint's tensile strength is a direct function of current, voltage, gas flow rate and filler material. Figure 5.4(a) shows the effect of each process variable on the joint's tensile

strength. Figure 5.4(b) shows the influence of each factor on a joint's tensile strength during welding of dissimilar stainless steels. Figure 5.4(a) reveals the fact that tensile strength enhances with the corresponding rise of voltage and welding current due to increase in heat contribution and more depth of penetration. The tensile strength of the material increases with a minimum gas flow rate of 10 L/min of argon gas because low gas flow rate of shielding gas accumulates the heat in the weld region. Hence, low cooling rate leads to fine grains and consequently, there will be higher tensile strength for the weld joint. In spray metal transfer, droplet size is generally much smaller than the wire diameter. The required transition current for spray transfer is approximately 220 A and this current produces a penetrating arc that cannot be used for thin sheet metal. In the present case, the welding current was 200 A, therefore, spray metal transfer is expected during deposition using GMAW setup (Ramesh et al., 2015). Spray metal transfer was also experienced owing to high voltage and argon rich shielding gas. With the increase of welding current, voltage and use of semi-automatic bi-directional GMAW setup (more uniform heat input), spray transfer of filler material took place and this improved the depth of penetration and the tensile strength. Low gas flow rate improved the tensile strength as heat transfer rate enhanced with the elevated flow rate of shielding gas and it resulted in poor joint strength. It was observed that the final heat accumulation for melting & joining and cooling rate played a significant role for influencing the tensile strength. As the tensile strengths of AISI 304 (535 MPa) and AISI 316 (545 MPa) austenitic stainless steels were very much closer to each other as compared to 2205 duplex stainless steel (655 MPa), the failure of the joint at the interface of weld bead and austenitic stainless steels had taken place. Consequently, closer tensile strength was observed at the interface for both AISI 304 and AISI 316. The same can be seen in the Fig. 5.4(a). Similarly, main effect plot and percentage contribution for bending strength depicted in Fig. 5.5(a) and Fig. 5.5(b) respectively, depict the influence of the process parameters on the bending strength of the joints. The bending strength was most significantly affected by SiO_2 activated flux followed by the gas supply rate, current, voltage and filler material. Figure 5.6(a) depicts the main effect plot for toughness and the variations of toughness were influenced by the process parameters. Contribution of each factor on toughness is depicted in Fig. 5.6(b). The welding current was the most

important parameter for joint toughness trailed by activated flux, gas flow rate and filler material. The significant values of elevated toughness were obtained at 200 A welding current using SiO_2 activated flux as depicted in Fig. 5.6(a). During joining of dissimilar metals, microhardness in the fusion zone became a critical issue as three different materials were joined together during welding. The average values of microhardness in fusion zone and ANOVA summary are shown in Table 5.3 and Table 5.4, respectively. Figure 5.7(a) indicates the main effect plot for microhardness and reveals that the gas flow rate and filler material are two most significant parameters that influence the microhardness in the fusion zone. Figure 5.7(b) indicates the contribution of each factor to the microhardness in the fusion zone. Comparatively, higher microhardness values were observed when joining was carried out using SiO_2 activated flux. Owing to better thermal conductivity and lower coefficient of thermal expansion, the duplex 2205 filler material resulted in significantly higher values of microhardness.

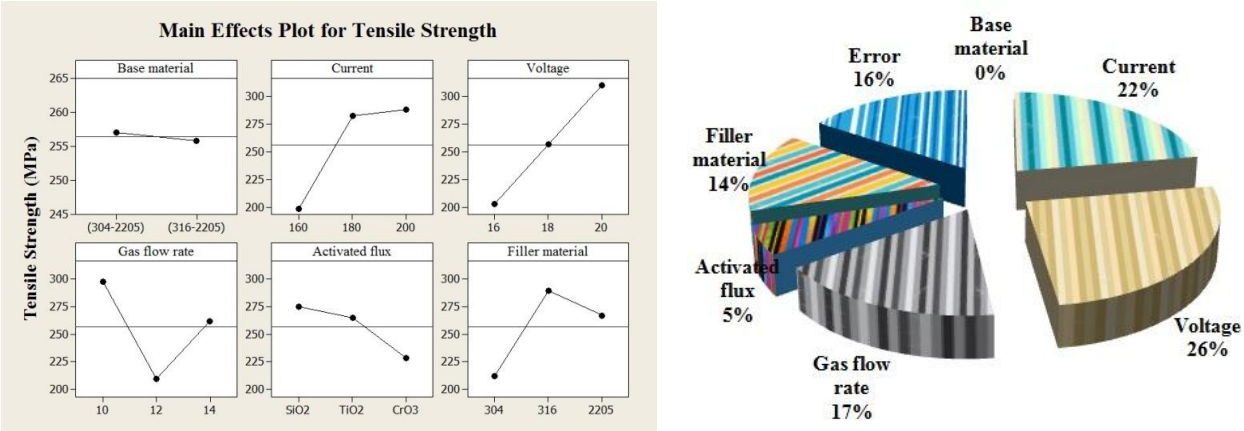

(a) (b)

Figure 5.4 (a) The effect of process variables on joint, (b) influence of each factor on the tensile strength of the joint of austenitic AISI 304/ 316 with duplex 2205

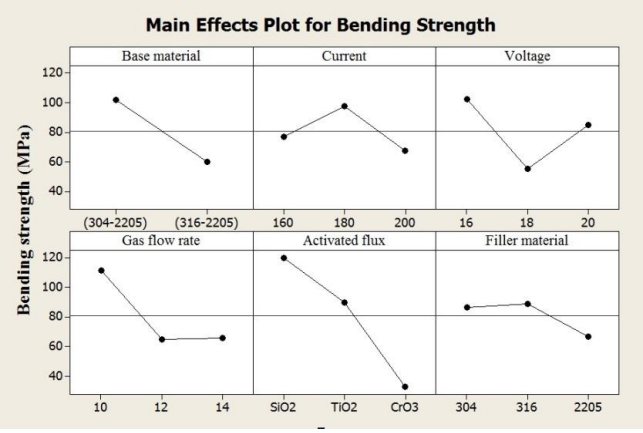

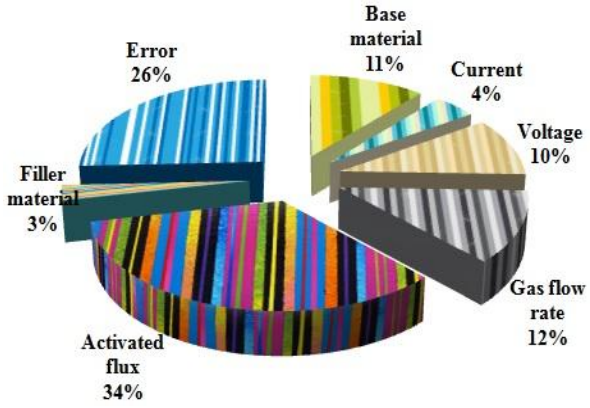

(a) (b)

Figure 5.5 (a) The effect of process variables on joint, (b) influence of each factor on the bending strength of the joint of austenitic AISI 304/ 316 with duplex 2205

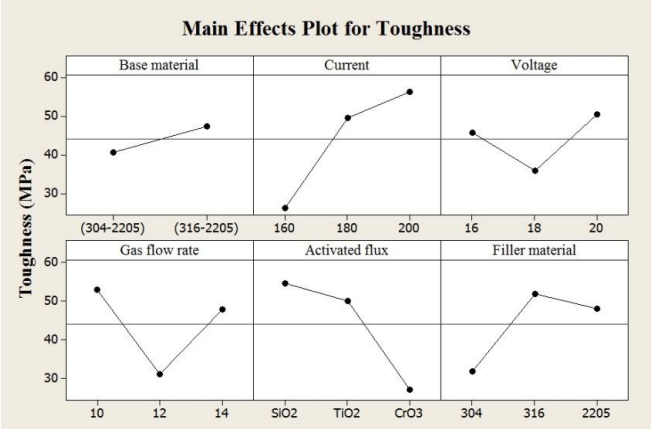

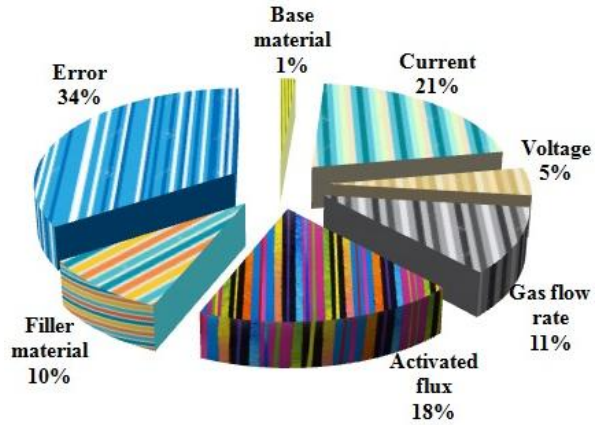

(a) (b)

Figure 5.6 (a) The effect of process variables on joint, (b) influence of each factor on the toughness of the joint of austenitic AISI 304/ 316 with duplex 2205

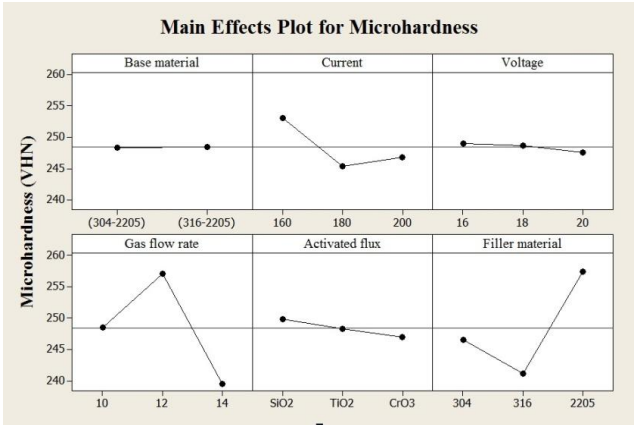

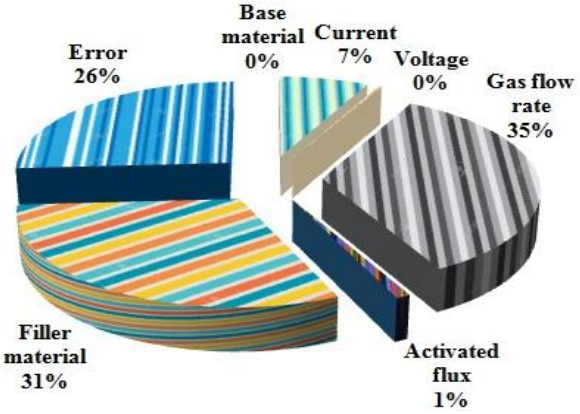

(a) (b)

Figure 5.7 (a) The effect of process variables on joint, (b) influence of each factor on the microhardness of the joint of austenitic AISI 304/ 316 with duplex 2205

Effect of three activated fluxes on the weld bead geometry is depicted in Fig. 5.8. The height of weld bead, bead width and penetration depth are indicated on each specimen. Figure 5.8 clearly reveals that with the help activated flux, full penetration depth is achieved in experiment no. 1, 9, 14 and 17 whereas in the remaining experiments, comparatively less penetration depth is observed. The oxygen ions present in SiO_2 activated flux interacts with electrons of arc column and rearranges the constriction of arc plasma and consequently, enhances the arc temperature and energy density. These changes in arc columns promote the electromagnetic Lorentz force which creates downward flow of liquid in the weld zone and results in deeper penetration. Oxygen ions also plays a vital role in the surface tension of the weld zone. Surface tension induces Marangoni convection which swaps the direction of flow of heat from outward (i.e., centrifugal) to inward (i.e., centripetal) leads to deeper penetration. SiO_2 among the three activated fluxes considerably influenced bead geometry and depth of penetration. This may be due to high temperature reactions between activated flux and workpiece material depending upon the chemical compositions. This high temperature reaction determines the potential of the Marangoni convection. Images of experiment no. 17 and 18 clearly indicate that bead width is influenced with high welding current and voltage.

Activated fluxes (SiO_2, TiO_2 and CrO_3) with higher oxygen content interacted considerably with electrons and ions involved in redistributing the charge carrier which resulted in constriction behaviour of plasma column. Furthermore, comparatively more amount of oxygen is present in CrO_3 than SiO_2 and TiO_2; the slag metal reaction and gas metal reaction promote to the formation of CO and CO_2. It would result in formation of blows or cavities in molten weld metal and consequently decrease in mechanical properties.

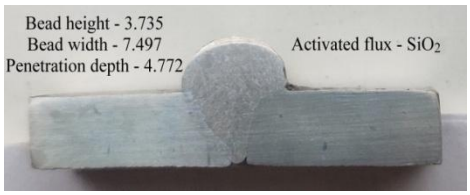

Experiment 1

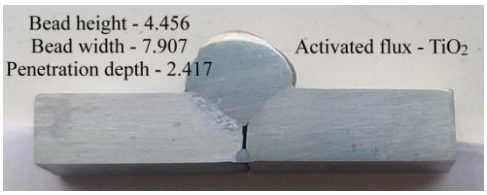

Experiment 2

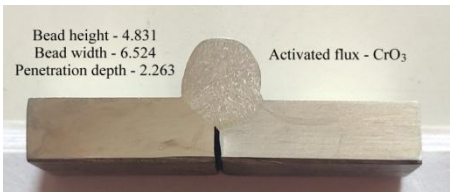

Experiment 3

Experiment 4

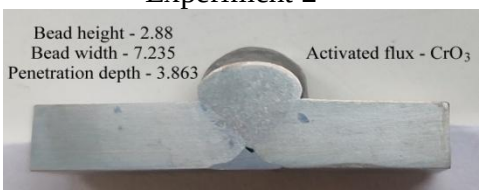

Experiment 5

Experiment 6

Experiment 7

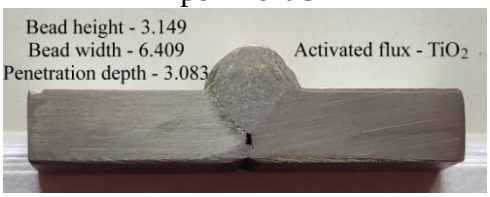

Experiment 8

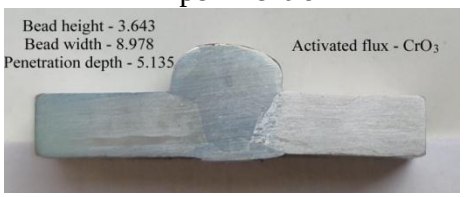

Experiment 9

Experiment 10

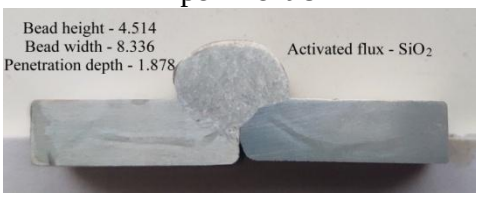

Experiment 11

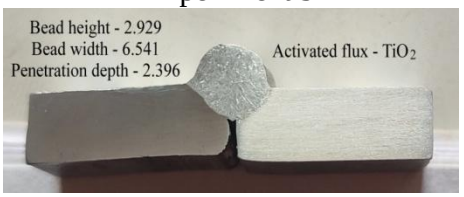

Experiment 12

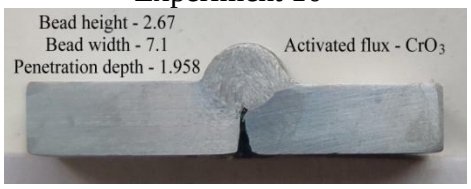

Experiment 13

Experiment 14

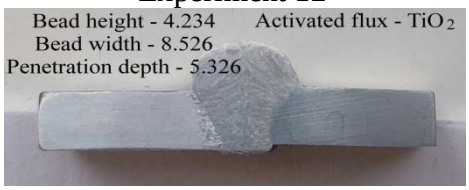

Experiment 15

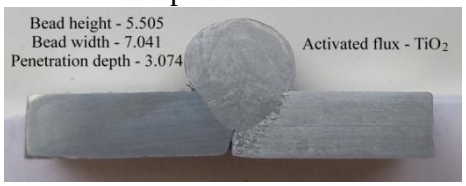

Experiment 16

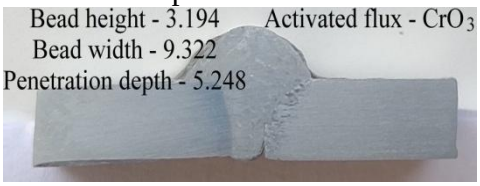

Experiment 17

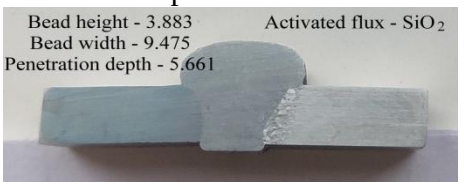

Experiment 18

Figure 5.8 Effects of activated fluxes on the weld bead geometry during 18 experiments

The microstructural study was carried out by SEM micrographs of samples prepared from joints of dissimilar steels as presented in Fig. 5.9. Trial numbers along with process parameters are given in the first column. The micrographs of the boundary of workpiece material and fusion region are given in the second column. SEM images clearly reveal the boundary marked by dotted lines between base metal and fusion zone

of selected specimens joining between dissimilar steels. It was also noticed that fine grain structure was created due to high gas flow rate or owing to rapid solidification rate. This led to high mechanical strength of the welded specimen. As observed from the SEM micrographs shown in Fig. 5.9, relatively low heat input (at welding current 160 A) in Expt. No. 1, leads to rapid solidification and grain growth in the weld joint and consequently improves the microhardness values. Austenite phase was observed in a few SEM micrographs of AISI 304 and AISI 316 stainless steels. Presence of austenite phase in Expt. No. 4, confirmed that the sufficient amount of heat was induced during welding to achieve full transformation from ferrite to austenite as sufficient amount of time was available for δ-ferrite to transform into austenite phase.

Figure 5.9 confirms the presence of white austenite phase and dark grey phase of ferrite in the SEM micrographs of duplex 2205. Depending upon the rate of cooling and composition, duplex stainless-steel cools as ferrite at some range of temperatures and as the temperatures come down, formation of austenite commences with ferrite-austenite combined structure. SEM micrographs of Expt. No. 7 (shown in Fig. 5.9) depict small dendritic grain growth in the fusion region in order to contribute more heat contribution during welding and this results in relatively poor tensile strength. Figure 5.9 clearly reveals improper fusion and separation of material at boundary of weld specimen and fusion region during Expt. No. 10 owing to relatively low welding current i.e., 160 A. Relatively low heat input and higher gas flow rate probably are the reason for the presence of vermicular ferrite morphology and separation at the interface of fusion zone and Duplex 2205. Similarly, in Expt. No. 15 at relatively higher heat input rate, high range of tensile strength of 397 MPa (second highest value) and toughness of 91.95 J were achieved. Without any solidification crack and a uniform fusion zone, the interface was observed from SEM micrographs as depicted in Fig. 5.9. A reasonably high tensile strength of 319 MPa and toughness of 95 J were obtained due to the high range of heat input in Expt. No. 16. A uniform weld interface between AISI 316 and Duplex 2205 was formed owing to sufficient heat input at maximum current of 200 A and the same can be observed from SEM images, as presented in Fig. 5.9.

Trial no. with parameters	Interface of base metal and fusion zone	
(Trial-1) 160 A, 16 V, 10 L/min, SiO_2, AISI 304	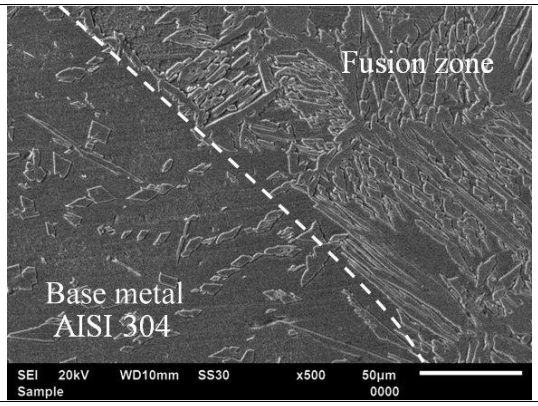	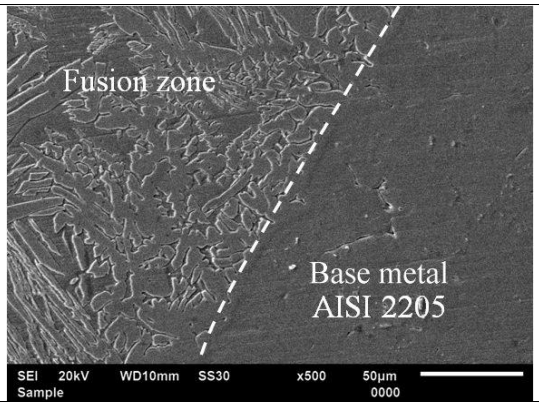
	Interface of AISI 304 and fusion zone	Interface of duplex 2205 and fusion zone
(Trial-4) 180 A, 16 V, 10 L/min, TiO_2, AISI 316	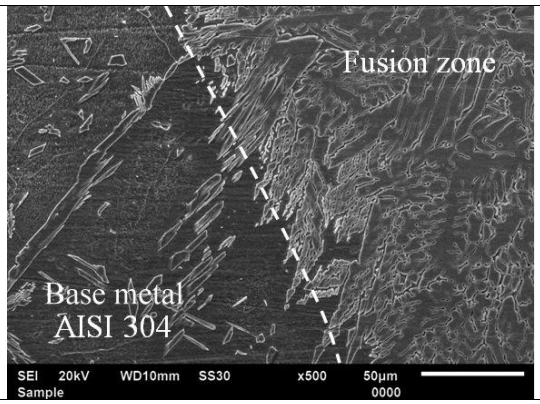	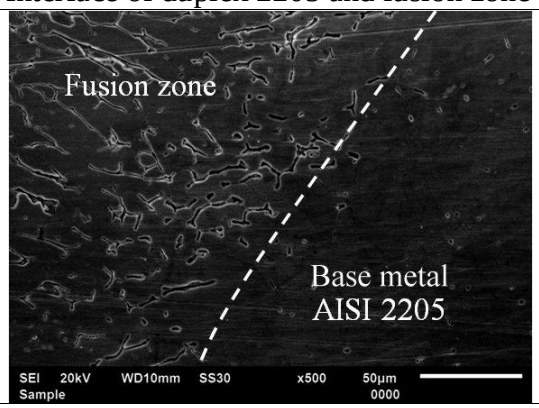
	Interface of AISI 304 and fusion zone	Interface of duplex 2205 and fusion zone
(Trial-7) 200 A, 16 V, 12 L/min, SiO_2, Duplex 2205	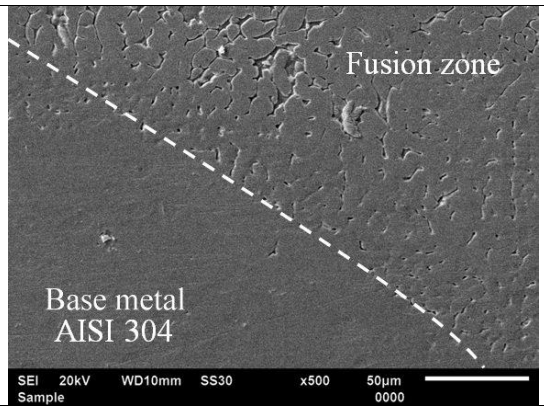	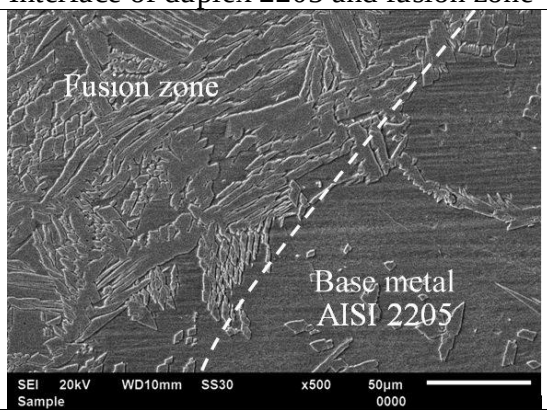
	Interface of AISI 304 and fusion zone	Interface of duplex 2205 and fusion zone

(Trial-10) 160 A, 16 V, 14 L/min, CrO_3, AISI 316	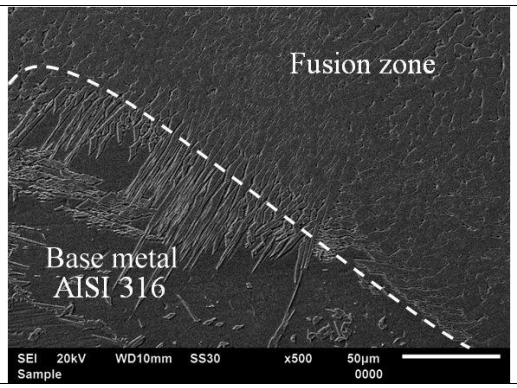	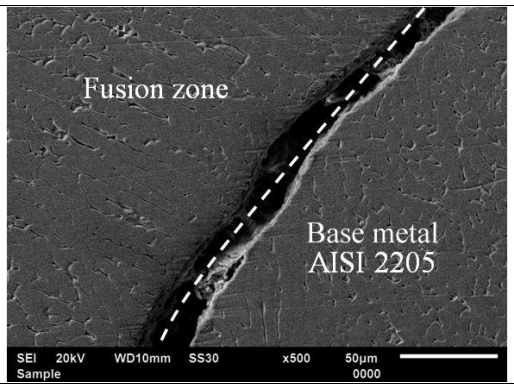
	Interface of AISI 316 and fusion region	Interface of duplex 2205 and fusion region
(Trial-15) 180 A, 20 V, 10 L/min, TiO_2, Duplex 2205	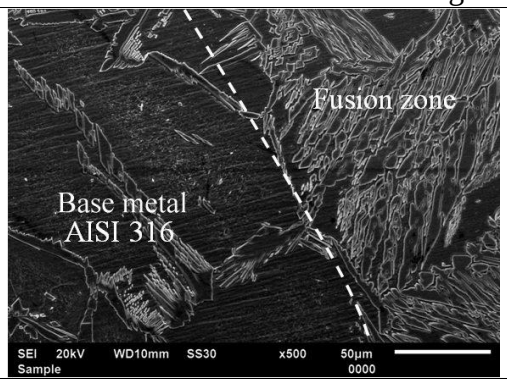	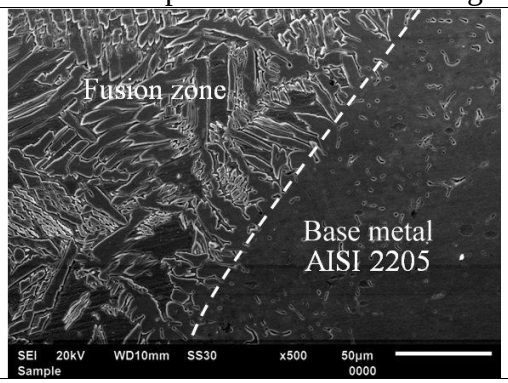
	Interface of AISI 316 and fusion region	Interface of duplex 2205 and fusion region
(Trial-16) 200 A, 16 V, 14 L/min, TiO_2, Duplex 2205	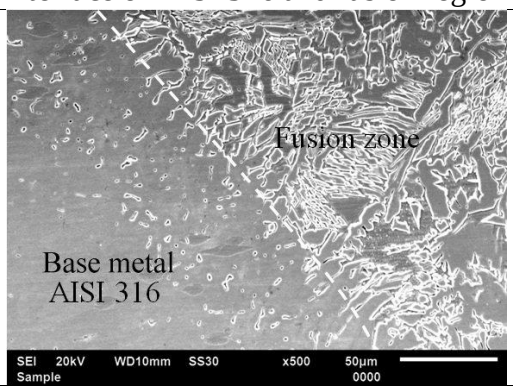	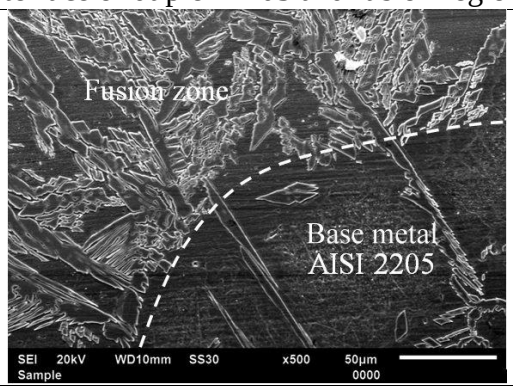
	Interface of AISI 316 and fusion region	Interface of duplex 2205 and fusion region

Figure 5.9 Metallurgical studies by SEM at boundaries between base material and fusion region after dissimilar joining

In this chapter, the welding of austenitic AISI 304/ 316 and duplex 2205 steels were performed in the presence of activated fluxes (SiO_2, TiO_2 and CrO_3) to enhance the penetration depth, as it is most desired aspect during joining, using the fabricated GMAW setup. The detailed discussion about experimental design by Taguchi factorial design of experiment (DOE) technique and subsequently statistical approach of analysis of variance

(ANOVA) was implemented to analyse the experimental results. Using ANOVA, the sum of squares and variance of each factor were calculated to estimate the influence of each factor in percentage. Statistical analysis helped to identify the influence of each process variable on responses. Effects of activated fluxes, influences of welding parameters namely welding current, voltage, workpiece material, filler material and flow rate of inert gas were examined on penetration-depth, microhardness, impact strength, tensile strength and bending strength of dissimilar steels. Microstructural observations were drawn through SEM images.

5.6 Techno-Economic Aspects

The comparisons of the Techno-Economic aspects of the developed GMAW setup to the conventional GMAW machine are given in Table 5.5.

Table 5.5 Comparison of Techno-Economic aspects

Parameter	**Welding with conventional method**	**Welding with developed GMAW setup**
1. Initial setup cost	Low	High
2. Labour cost	High	Less
3. Running cost including power, filler wire, shielding gas	Same	Same
4. Material loss in spatters owing to variation in gap between contact tube and workpiece	High	Very low
5. Weld quality	Acceptable	Excellent

The conclusions derived from the experimental and analytical work are presented in Chapter-6.

Chapter 6
Conclusions

Design and development of a bi-directional automatic movement setup using GMAW technique to deposit different open and closed profiles in single bead layer deposition and single bead multi layers depositions were carried out to measure its capabilities/effectiveness and subsequently to enhance the versatility of the fabricated setup. Three dimensional components having negative and positive slopes were deposited using different weld bead path strategies. These have been explored in the previous Chapters 3 and 4. The welding of two dissimilar metals i.e., austenitic AISI 304 and 316 stainless steels with duplex 2205 in the presence of three different activated fluxes i.e., SiO_2, TiO_2 and CrO_3 have been discussed in detail in Chapter 5.

6.1 Conclusions

Based on the results presented in chapters 3 to 5, the following conclusions can be drawn:

- The designed and developed bi-directional automatic movement setup for GMAW used in this research work is simple, indigenous, accurate and inexpensive.
- The deposited weld path as measured by CMM was compared with the predicted (using BG modelling technique) path for individual and simultaneous movement of the welding torch along two axes at different weld speeds. Measured weld paths were found to be in good agreement with the predicted/desired path with reasonable uniformity in weld bead width in most of the cases.
- The developed machine was suitable for effectively tracking the reference path and executing welding of any shape in two-dimension.
- The constant contact tube to work distance provided by the automated fabricated setup is required to achieve the significant consistency in weld bead width for all deposited profiles.
- Results achieved in this research work revealed that the weld bead width increased due to lowest speed in case of spiral shaped weld profile and consequently, maximum

heat was generated for this profile followed by S-shape, circular and elliptical profiles.

- The micrograph showed comparatively finer equiaxed grains produced in the weld fusion zone than HAZ due to relatively high heat input in case of spiral profile.
- Maximum micro hardness value was observed in HAZ followed by weld metal and base metal in all the profiles.
- The average depth of penetration was relatively more for open profiles (S-shape and spiral) than the closed profiles (circular and elliptical).
- The bead deposition was consistent i.e., deposited width and the layer heights all over the path of the deposition for different geometric shapes were almost uniform. Thus, the developed machine was suitable for executing 3D metal deposition of any simple or complex shape. The proposed equipment is reliable for complex shaped products and it is robust for varying process conditions.
- The average layer heights for cylindrical, elliptical, concave, semi-cylindrical, double semi-cylindrical and V-profile were almost uniform. The variation of heights those were measured was about 0.6 mm.
- Results revealed that in case of different profiles, the deposited width remained almost the same due to lower variation (0.1 mm/s) of speed. The variation in width was about 0.8 mm.
- The micrograph showed that comparatively finer equi-axed grains were produced in the deposition fusion zone than HAZ.
- It is observed in all profiles that micro-hardness is maximum (192.64–210.29 VHN) in the heat affected zone; micro-hardness of the metal deposition (151.91–186.81 VHN) is less than the micro hardness of base metal (158.04–188.1 VHN) as well as HAZ.
- The fabricated setup was capable of building overhanging components with a maximum of 20˚ inclination.
- Relatively low welding current and fast welding speed influence the deposition accuracy while depositing negative slopes.
- Comparatively better results were obtained from tensile, bending and microhardness testing and these results support that the deposited parts have dense structure.

- Amongst the five deposition strategies, raster linear (circular) exhibited highest tensile strength value followed by raster diagonal (square), raster (square), spiral-in (square) and spiral-in (circular).
- Yielding strength of the deposited specimens was significantly influenced during raster diagonal (square) deposition strategy.
- Low gas flow rate (10 L/min) improved the tensile strength as elevated gas flow rate of the shielding gas increased the heat transfer rate which resulted in poor joint strength.
- Bending strength of welded specimens in dissimilar metal joining was highly influenced by activated flux, gas flow rate, welding current and voltage.
- Use of duplex 2205 as filler material with a moderate supply of shielding gas improved the microhardness in the fusion zone.
- Welding current, activated flux and gas flow rate were significant process parameters which controlled the toughness of welded joints.
- Among the activated fluxes, SiO_2 significantly improved the bending strength and toughness as compared to tensile strength and microhardness.

6.2 Scope for Future Work

Research areas in automated welding are broad. Several areas regarding the proposed fabrication method which merit study, or development in more detail, include

1. A bi-directional automatic movement setup for GMAW may be modified for third directions i.e., *z*-direction and this will give freedom to welders to build 3D objects automatically as compared to manually controlling.

2. The same setup may be implemented in other engineering applications (pressure assisted WAAM) by simply replacing the welding torch with other tooling (roller or FSW tool with the application of pressure for the plastic deformation of the deposited metal).

3. The fabricated setup could be modified with concrete nozzle and other necessary changes for construction work of 3D printing of buildings.

4. In the fabricated setup, the welding torch may be replaced by FSW tool for friction stir welding process.
5. Similar and dissimilar metals joining with the combinations of other useful alloys may be introduced using present automatic setup.
6. Wood working is another interesting field where this setup can be implemented as a router machine.

References

Ahmad R and Bakar MA. Effect of a post-weld heat treatment on the mechanical and microstructure properties of AA6061 joints welded by the gas metal arc welding cold metal transfer method. *Materials and Design*. 2011; 32: 5120–5126.

Arif N and Chung H. Alternating current-gas metal arc welding for application to thin sheets. *Journal of Materials Processing Technology*. 2014; 214: 1828–1837.

ASTM E23-16a. *Standard test methods for impact testing of material for ductility.* ASTM International. West Conshohocken, PA, 2016.

ASTM E290-14. *Standard test methods for bend testing of material for ductility*. ASTM International. West Conshohocken, PA, 2014.

ASTM E8/E8M-15a. *Standard test methods for tension testing of metallic materials*. ASTM International. West Conshohocken, PA, 2015.

Bajpai PK, Singh I and Madaan J. Comparative studies of mechanical and morphological properties of polylactic acid and polypropylene based natural fiber composites. *Journal of Reinforced Plastics and Composites*. 2012; 31(24): 1712–1724.

Bhattacharya A and Bera TK. Development of automatic GMAW setup for process improvements: experimental and modeling approach. *Materials and Manufacturing Processes*. 2014; 29(8): 988–995.

Bhattacharya A and Kumar R. Dissimilar joining between austenitic and duplex stainless steel in double-shielded GMAW: a comparative study. *Materials and Manufacturing Processes*. 2016; 31(3): 300–310.

Bhattacharya A and Singla S. Mechanical properties and metallurgical characterization of dissimilar welded joints between AISI 316 and AISI 4340. *Transactions of the Indian Institute of Metals*. 2017; 70(4): 893–901.

Bhattacharya A, Bera TK and Suri VK. Influence of heat input in automatic GMAW: penetration prediction and microstructural observation. *Materials and Manufacturing Processes*. 2014; 29(10): 1210–1218.

Caggiano A, Nele L, Sarno E and Teti R. 3D digital reconfiguration of an automated welding system for a railway manufacturing application. *Procedia CIRP*. 2014; 25: 39–45.

Cao Y, Zhu S, Liang X and Wang W. Overlapping model of beads and curve fitting of bead section for rapid manufacturing by robotic MAG welding process. *Robotics and Computer-Integrated Manufacturing*. 2011; 27(3): 641–645.

Chapuis J, Romero E, Soulie F, Bordreuil C and Fras G. Behaviour of spreading molten metal drops deposited by fusion. *Experimental Thermal and Fluid Science*. 2013; 48: 29–36.

Chaudhari PG, Patel PB and Patel JD. Evaluation of MIG welding process parameter using activated flux on SS316L by AHP-MOORA method. *Materials Today: Proceedings*. 2018; 5(2): 5208–5220.

Chiumenti M, Cervera M, Salmi A, De Saracibar CA, Dialami N and Matsui K. Finite element modeling of multi-pass welding and shaped metal deposition processes. *Computer Methods in Applied Mechanics and Engineering*. 2010; 199(37–40): 2343–2359.

Clark D, Bache MR and Whittaker MT. Shaped metal deposition of a nickel alloy for aero engine applications. *Journal of Materials Processing Technology*. 2008; 203(1–3): 439–448.

Dhandha KH and Badheka VJ. Effect of activating fluxes on weld bead morphology of P91 steel bead-on-plate welds by flux assisted tungsten inert gas welding process. *Journal of Manufacturing Processes*. 2015; 17: 48–57.

Di X, Deng S and Wang B. Effect of pulse current on mechanical properties and dendritic morphology of modified medium manganese steel welds metal. *Materials and Design*. 2015; 66: 169–175.

Ding D, Pan Z, Cuiuri D and Li H. A multi-bead over lapping model for robotic wire and arc additive manufacturing (WAAM), *Robotics and Computer-Integrated Manufacturing*. 2015; 31: 101–110.

Ding D, Pan Z, Cuiuri D and Li H. A practical path planning methodology for wire and arc additive manufacturing of thin-walled structures. *Robotics and Computer-Integrated Manufacturing*. 2015; 34: 8–19.

Ding D, Pan Z, Cuiuri D and Li H. A tool-path generation strategy for wire and arc additive manufacturing. *The International Journal of Advanced Manufacturing Technology*. 2014; 73(1–4): 173–183.

Ding D, Pan Z, Cuiuri D and Li H. Wire-feed additive manufacturing of metal components: technologies, developments and future interests. *The International Journal of Advanced Manufacturing Technology*. 2015; 81(1–4): 465–481.

Ding D, Pan Z, Cuiuri D, Li H, Duin S and Larkin N. Bead modelling and implementation of adaptive MAT path in wire and arc additive manufacturing. *Robotics and Computer-Integrated Manufacturing*. 2016; 39: 32–42.

Duraisamy R, Mohan KS, Rajesh KA, Siva SN and Sankaranarayanasamy K. Reliability and sustainability of wire arc additive manufactured plates using ER 347 wire-mechanical and metallurgical perspectives. *Proceedings of the Institution of Mechanical Engineers, Part C: Journal of Mechanical Engineering Science*. 2021; 235(10), 1860–1871.

Elmer JW, Vaja J, Carpenter JS, Coughlin DR, Dvornak MJ, Hochanadel P, Gurung P, Johnson A and Gibbs G. Wire-based additive manufacturing of stainless steel components. *Welding Journal*. 2020; 99(1): 8–24.

Ferro CG, Mazza A, Belmonte D, Seclì C and Maggiore P. A comparison between 3D printing and milling process for a spar cap fitting (wing-fuselage) of UAV aircraft. *Procedia CIRP*. 2017; 62: 487–493.

Flynn JM, Shokrani A, Newman ST and Dhokia V. Hybrid additive and subtractive machine tools – Research and industrial developments. *International Journal of Machine Tools and Manufacture*. 2016; 101: 79–101.

Ghosh N, Pal PK and Nandi G. GMAW dissimilar welding of AISI 409 ferritic stainless steel to AISI 316L austenitic stainless steel by using AISI 308 filler wire. *Engineering Science and Technology, an International Journal*. 2017; 20(4): 1334–1341.

Haden CV, Zeng G, Carter FM, Ruhl C, Krick BA and Harlow DG. Wire and arc additive manufactured steel: Tensile and wear properties. *Additive Manufacturing*. 2017; 16: 115–123.

Haselhuhn AS, Buhr MW, Wijnen B, Sanders PG and Pearce JM. Structure-property relationships of common aluminum weld alloys utilized as feedstock for GMAW-based 3-D metal printing. *Materials Science & Engineering A*. 2016; 673: 511–523.

Haselhuhn AS, Wijnen B, Anzalone GC, Sanders PG and Pearce JM. In situ formation of substrate release mechanisms for gas metal arc weld metal 3-D printing. *Journal of Materials Processing Technology*. 2015; 226: 50–59.

Heinl P, Muller L, Korner C, Singer RF and Muller FA. Cellular Ti–6Al–4V structures with interconnected macro porosity for bone implants fabricated by selective electron beam melting. *Acta biomaterialia*. 2008; 4(5): 1536–1544.

Henckell P, Gunther K, Ali Y, Bergmann JP, Scholz J and Foret P. The influence of gas cooling in context of wire arc additive manufacturing—a novel strategy of affecting grain structure and size. In: *TMS 2017 146th Annual Meeting & Exhibition Supplemental Proceedings*. Springer, Cham. 2017; 147–156.

Horgar A, Fostervoll H, Nyhus B, Ren X, Eriksson M and Akselsen OM. Additive manufacturing using WAAM with AA5183 wire. *Journal of Materials Processing Technology*. 2018; 259: 68–74.

Horii T, Kirihara S and Miyamoto Y. Freeform fabrication of Ti–Al alloys by 3D micro-welding. *Intermetallics*. 2008; 16(11–12): 1245–1249.

Huang HY. Effects of activating flux on the welded joint characteristics in gas metal arc welding, *Materials & Design*. 2010; 31(5): 2488–2495.

Huang HY. Effects of shielding gas composition and activating flux on GTAW weldments. *Materials and Design*. 2009; 30: 2404–2409.

Huang J, He X, Guo Y, Zhang Z, Shi Y and Fan D. Joining of aluminum alloys to galvanized mild steel by the pulsed DE-GMAW with the alternation of droplet transfer. *Journal of Manufacturing Processes*. 2017; 25: 16–25.

Jain P, Bera TK, Rafique S, Singla A and Isaksson M. Comparative study of knee joint torque estimations for linear and rotary actuators using bond graph approach for stand–sit–stand motions. *International Journal of Advanced Robotic Systems*. 2020; 17(5): 1–13.

Jha MS, Chatti N and Declerck P. Robust fault detection in bond graph framework using interval analysis and Fourier-Motzkin elimination technique. *Mechanical Systems and Signal Processing*. 2017; 93: 494–514.

Jin Y, Du J, Ma Z, Liu A and He Y. An optimization approach for path planning of high-quality and uniform additive manufacturing. *The International Journal of Advanced Manufacturing Technology*. 2017; 92(1–4): 651–662.

Karunakaran KP, Suryakumar S, Pushpa V and Akula S. Low-cost integration of additive and subtractive processes for hybrid layered manufacturing. *Robotics and Computer-Integrated Manufacturing*. 2010; 26(5): 490–499.

Kazanas P, Deherkar P, Almeida P, Lockett H and Williams S. Fabrication of geometrical features using wire and arc additive manufacture. *Proceedings of the Institution of Mechanical Engineers, Part B: Journal of Engineering Manufacture*. 2012; 226(6): 1042–1051.

Khan WN and Chhibber R. Experimental investigation on dissimilar weld between super duplex stainless steel 2507 and API X70 pipeline steel. *Proceedings of the Institution of Mechanical Engineers, Part L: Journal of Materials: Design and Applications*. 2021; 1–14.

Kim IS, Son JS, Kim IG, Kim JY and Kim OS. A study on relationship between process variables and bead penetration for robotic CO2 arc welding. *Journal of Materials Processing Technology*. 2003; 136: 139–145.

Kruth JP, Froyen, L, Van VJ, Mercelis P, Rombouts M and Lauwers B. Selective laser melting of iron-based powder. *Journal of materials processing technology*. 2004; 149(1–3): 616–622.

Kumar R, Bhattacharya A and Bera TK. Mechanical and metallurgical studies in double shielded GMAW of dissimilar stainless steels. *Materials and Manufacturing Processes*. 2015; 30(9): 1146–1153.

Kumar V and Bera TK. Performance of automated machine for different profiles in two-dimensional welding. *Materials and Manufacturing Processes*. 2021; 36(4): 435–447.

Kumar V, Bera TK and Bhattacharya A. Development and performance analysis of semi-automatic movement setup for planar welding. *Materials and Manufacturing Processes*. 2019; 34(11): 1251–261.

Kwak YM and Doumanidis CC. Geometry regulation of material deposition in near-net shape manufacturing by thermally scanned welding. *Journal of Manufacturing Processes*. 2002; 4(1): 28–41.

Lee W, Wei C and Chung SC. Development of a hybrid rapid prototyping system using low-cost fused deposition modeling and five-axis machining. *Journal of Materials Processing Technology*. 2014; 214(11): 2366–2374.

Li Y, Huang X, Horvath I and Zhang G. GMAW-based additive manufacturing of inclined multi-layer multi-bead parts with flat-position deposition. *Journal of Materials Processing Technology*. 2018; 262: 359–371.

Liu H, Cheng Zhi, Huang J, Ye Z, Yang J, Chen S and Zhao X. Feasibility study of different filler metals on MIG-TIG double-sided arc brazing of titanium alloy-stainless steel. *Journal of Manufacturing Processes*. 2019; 47: 183–191.

Liu ZY, Li C, Fang XY and Guo YB. Energy consumption in additive manufacturing of metal parts. *Procedia Manufacturing*. 2018; 26: 834–845.

Lu F, Wang HP, Murphy AB and Carlson BE. Analysis of energy flow in gas metal arc welding processes through self-consistent three-dimensional process simulation. *International Journal of Heat and Mass Transfer*. 2014; 68: 215–223.

Mercado Rojas JG, Wolfe T, Fleck BA and Qureshi AJ. Plasma transferred arc additive manufacturing of nickel metal matrix composites. *Manufacturing Letters*. 2018; 18: 31–34.

Nadkarni SV. Modern arc welding technology. *Oxford & IBH Publishing Co. Pvt. Ltd.* New Delhi, India. 1998.

Nilsiam Y, Sanders P and Pearce J. Applications of open source GMAW-based metal 3-D printing. *Journal of Manufacturing and Materials Processing*. 2018; 2(1): 18.

Nilsiam Y, Sanders P and Pearce JM. Slicer and process improvements for open-source GMAW-based metal 3-D printing. *Additive Manufacturing*. 2017; 18: 110–120.

Ogino Y, Asai S and Hirata Y. Numerical simulation of WAAM process by a GMAW weld pool model. *Welding in the World*. 2018; 62(2): 393–401.

Palanivel R, Dinaharan I, Laubscher RF and Davim JP. Influence of boron nitride nanoparticles on microstructure and wear behavior of AA6082/TiB2 hybrid aluminum composites synthesized by friction stir processing. *Materials and Design*. 2016; 106: 195–204.

Panchagnula JS and Simhambhatla S. Feature based weld-deposition for additive manufacturing of complex shapes. *Journal of The Institution of Engineers (India): Series C*. 2016; 99(3): 285–292.

Panchagnula JS and Simhambhatla S. Manufacture of complex thin-walled metallic objects using weld-deposition based additive manufacturing. *Robotics and Computer-Integrated Manufacturing*. 2018; 49: 194–203.

Pardal G, Martina F and Williams S. Laser stabilization of GMAW additive manufacturing of Ti-6Al-4V components. *Journal of Materials Processing Technology*. 2019; 272: 1–8.

Qi L, Chao Y, Luo J, Zhou J, Hou X and Li H. A novel selection method of scanning step for fabricating metal components based on micro-droplet deposition manufacture. *International Journal of Machine Tools and Manufacture*. 2012; 56: 50–58.

Rao PN. Manufacturing Technology–Vol. 1. 3rd edition. *Tata Mc-Graw Hill*, New Delhi. 2009.

Ruan Y, Qiu XM, Gong WB, Sun DQ and Li YP. Mechanical properties and microstructures of 6082-T6 joint welded by twin wire metal inert gas arc welding with the SiO_2 flux. *Materials & Design*. 2012; 35: 20–24.

Sachin R, Sumesh A and Upas US. Study of mechanical properties and weldability of aluminium alloy and stainless steel by gas metal arc welding. *Materials Today: Proceedings*. 2020; 24: 1167–1173.

Sandhu K, Singh G, Singh S, Kumar R, Prakash C, Ramakrishna S, Krolczyk G and Pruncu CI. Surface characteristics of machined polystyrene with 3D printed thermoplastic tool. *Materials*. 2020; 13(12): 2729 1–16.

Shi J, Li F, Chen S and Zhao Y. T-GMAW based novel multi-node trajectory planning for fabricating grid stiffened panels: An efficient production technology. *Journal of Cleaner Production*. 2019; 238: 1–10.

Simchi A, Petzoldt F and Pohl H. On the development of direct metal laser sintering for rapid tooling. *Journal of materials processing technology*. 2003; 141(3): 319–328.

Singh A and Bera TK. Bond graph aided thermal modelling of twin-tube shock absorber. *International Journal of Modelling and Simulation*. 2016; 36(4): 183–192.

Singh G, Saxena RK and Pandey S. Investigating the effect of arc offsetting in AISI 304 stainless steel and copper welding using gas tungsten arc welding. *Journal of the Brazilian Society of Mechanical Sciences and Engineering*. 2021; 43(174): 1–22.

Singh J, Arora KS and Shukla DK. Dissimilar MIG-CMT weld-brazing of aluminium to steel: A review. *Journal of Alloys and Compounds*. 2019; 783: 753–764.

Singh R and Bera TK. Bond graph approach for dynamic modelling of the biped robot and application to obstacle avoidance. *Journal of the Brazilian Society of Mechanical Sciences and Engineering*. 2019; 41(10): 1–12.

Somashekara MA, Naveenkumar M, Kumar A, Viswanath C and Simhambhatla S. Investigations into effect of weld-deposition pattern on residual stress evolution for metallic additive manufacturing. *The International Journal of Advanced Manufacturing Technology*. 2016; 90(5–8): 2009–2025.

Song YA and Park S. Experimental investigations into rapid prototyping of composites by novel hybrid deposition process. *Journal of Materials Processing Technology*. 2006; 171(1): 35–40.

Song YA, Park S and Chae SW. 3D welding and milling: part II—optimization of the 3D welding process using an experimental design approach. *International Journal of Machine Tools and Manufacture*. 2005; 45(9): 1063–1069.

Song YA, Park S, Choi D and Jee H. 3D welding and milling: Part I–a direct approach for freeform fabrication of metallic prototypes. *International Journal of Machine Tools & Manufacture*. 2005; 45: 1057–1062.

Sravanthi SS, Acharyya SG, Prabhakar KVP and Padmanabham G. Integrity of 5052 Al-mild steel dissimilar welds fabricated using MIG-brazing and cold metal transfer in nitric acid medium. *Journal of Materials Processing Technology*. 2019; 268: 97–106.

Sudhakar R, Sivasubramanian R and Yoganandh J. Effect of automated MIG welding process parameters on ASTM A 106 Grade B pipe weldments used in high-temperature applications, *Materials and Manufacturing Processes*. 2017; 33(7): 749–758.

Suryakumar S, Karunakaran KP, Bernard A, Chandrasekhar U, Raghavender N and Sharma D. Weld bead modeling and process optimization in hybrid layered manufacturing. *Computer-Aided Design*. 2011; 43(4): 331–344.

Taminger K and Hafley RA. Electron beam freeform fabrication: a rapid metal deposition process. In: *Proceedings of third annual automotive composites conference, Society of Plastic Engineers*. Troy, 2003; 9–10.

Tathgir S and Bhattacharya A. Activated-TIG welding of different steels: influence of various flux and shielding gas. *Materials and Manufacturing Processes*. 2016; 31(3): 335–342.

Tathgir S, Bhattacharya A and Bera TK. Influence of current and shielding gas in TiO2 flux activated TIG welding on different graded steels. *Materials and Manufacturing Processes*. 2015; 30(9): 1115–1123.

Tidriri K, Chatti N, Verron S and Tiplica T. A bond graph modeling for health monitoring and diagnosis of the tennessee eastman process. In *2017 4th IEEE International Conference on Control, Decision and Information Technologies (CoDIT)*. Barcelona, Spain. 2017; 0155–0160.

Tiwari A, Singh P, Pankaj P, Biswas P, Kore SD and Pal S. Effect of tool offset and rotational speed in dissimilar friction stir welding of AISI 304 stainless steel and mild steel. *Journal of Materials Engineering and Performance*. 2019; 28(10): 6365–6379.

Utela B, Storti D, Anderson R and Ganter M. A review of process development steps for new material systems in three-dimensional printing (3DP). *Journal of Manufacturing Processes*. 2008; 10(2): 96–104.

Varbai B, Kormos R and Majlinger K. Effects of active fluxes in gas metal arc welding. *Periodica Polytechnica Mechanical Engineering*. 2017; 61(1): 68–73.

Vora JJ and Badheka VJ. Experimental investigation on microstructure and mechanical properties of activated TIG welded reduced activation ferritic/martensitic steel joints. *Journal of Manufacturing Processes*. 2017; 25: 85–93.

Wang F, Williams S, Colegrove P and Antonysamy AA. Microstructure and mechanical properties of wire and arc additive manufactured Ti-6Al-4V. *Metallurgical and materials transactions A*. 2013; 44(2): 968–977.

Wang L, Chen J, Fan XH and Wu CS. Influence of fluid flow on humping bead during high-speed GMAW. *Welding Journal*. 2019; 98: 315s–327s.

Wang L, Chen J, Wu C and Gao J. Backward flowing molten metal in weld pool and its influence on humping bead in high-speed GMAW. *Journal of Materials Processing Technology*. 2016; 237: 342–350.

Xiong J and Zhang G. Online measurement of bead geometry in GMAW-based additive manufacturing using passive vision. *Measurement Science and Technology*. 2013; 24(11): 1–7.

Xiong J, Lei Y and Li R. Finite element analysis and experimental validation of thermal behavior for thin-walled parts in GMAW-based additive manufacturing with various substrate preheating temperatures. *Applied Thermal Engineering*. 2017; 126: 43–52.

Xiong J, Lei Y, Chen H and Zhang G. Fabrication of inclined thin-walled parts in multi-layer single-pass GMAW-based additive manufacturing with flat position deposition. *Journal of Materials Processing Technology*. 2017; 240: 397–403.

Xiong J, Zhang G and Zhang W. Forming appearance analysis in multi-layer single-pass GMAW-based additive manufacturing. *The International Journal of Advanced Manufacturing Technology*. 2015; 80(9–12): 1767–1776.

Xiong J, Zhang G, Gao H and Wu L. Modeling of bead section profile and over lapping beads with experimental validation for robotic GMAW-based rapid manufacturing, *Robotics and Computer-Integrated Manufacturing*. 2013; 29: 417–423.

Xiong J, Zhang G, Hu J and Wu L. Bead geometry prediction for robotic GMAW-based rapid manufacturing through a neural network and a second-order regression analysis. *Journal of Intelligent Manufacturing*. 2014; 25: 157–163.

Xiong J, Zhang G, Qiu Z and Li Y. Vision-sensing and bead width control of a single-bead multi-layer part: material and energy savings in GMAW-based rapid manufacturing. *Journal of Cleaner Production*. 2013; 41: 82–88.

Xiong X, Zhang H and Wang G. Metal direct prototyping by using hybrid plasma deposition and milling. *Journal of Materials Processing Technology*. 2009; 209(1): 124–130.

Xu X, Ding J, Ganguly S, Diao C and Williams S. Oxide accumulation effects on wire + arc layer-by-layer additive manufacture process. *Journal of Materials Processing Technology*. 2018; 252: 739–750.

Yang D, He C and Zhang G. Forming characteristics of thin-wall steel parts by double electrode GMAW based additive manufacturing. *Journal of Materials Processing Technology*. 2016; 227: 153–160.

Yang D, Wang G and Zhang G. Thermal analysis for single-pass multi-layer GMAW based additive manufacturing using infrared thermography. *Journal of Materials Processing Technology*. 2017; 244: 215–224.

Zhang Y, Chen Y, Li P and Male AT. Weld deposition-based rapid prototyping: a preliminary study. *Journal of Materials Processing Technology*. 2003; 135(2-3): 347–357.

Zhang Y, Huang J, Cheng Z, Ye Z, Chi H, Peng L and Chen S. Study on MIG-TIG double-sided arc welding brazing of aluminum and stainless steel. *Materials Letters*. 2016; 172: 146–148.

Zhang ZD and Cao QJ. Study on metal transfer behaviour in metal inert gas arc welding with activating flux for magnesium alloy. *Science and Technology of Welding and Joining*. 2012; 17(7): 550–555.

Zhao H, Zhang G, Yin Z and Wu L. Three-dimensional finite element analysis of thermal stress in single-pass multi-layer weld-based rapid prototyping. *Journal of Materials Processing Technology*. 2012; 212(1): 276–285.

Curriculum Vitae

Vinod Kumar did his graduation (Bachelor of Engineering) in Mechanical Engineering from Thapar Institute of Engineering & Technology (Deemed to be University) (formerly Thapar University), Patiala, Punjab, India in the year 2010. After that, he has worked for three years as Lecturer at Rayat Polytechnic College, Railmajra, Shaheed Bhagat Singh Nagar, Punjab. He obtained his Master of Engineering (M.E.) (Part-Time) degree in Production & Industrial Engineering from Thapar Institute of Engineering & Technology, Patiala, Punjab in the year 2014. Then, he worked as Lab Instructor in the department of Mechanical Engineering at Indian Institute of Technology, Ropar for two years. In the year 2017, he joined in the Ph.D. Program (Part-Time) at Thapar Institute of Engineering & Technology (Deemed to be University), Patiala, Punjab as a Research Scholar to pursue his research work in the area of **'Studies on Joining and Deposition using Planar Movement Setup for GMAW'**. He is presently working as Welding Instructor in the Department of Technical Education and Industrial Training, Punjab since 2015.